ABSTRACT

FIGURSKEY, SULLIVAN J. Thermal and Thermodynamic Modeling of WC-Co and Mo-Metal Matrix Composites for Electron Beam Powder Bed Fusion.

The Additive Manufacturing (AM) of materials that require tight temperature and process control to achieve desired characteristics or properties similar to those produced from traditional processes is challenging. Among these difficulties are accurate temperature measurement as well as the control of small melt pools with extreme and rapidly changing localized boundary conditions. Representative thermal and fluid dynamic modeling of AM systems have been shown by a number of groups to be highly informative in understanding the complex nature of metal 3D printing; however, fully coupled models can be very computationally expensive. Similarly, detailed in-situ process monitoring for measurement of temperatures and other melt pool properties has been shown to be effective and accurate, though significant investment is required.

In this study, an FEM-based thermal model and commercial thermodynamic software were utilized to quickly predict aspects of the process such as temperature and phase prediction as a result of electron beam melting, with increased flexibility and computational efficiency. Such predicted characteristics include melt pool size, thermal profiles and material phases and microstructures. The alloys selected for study were WC-11Co and a Mo-TiC metal matrix composite, chosen as demonstration materials due to their non-AM, traditional process metallurgy manufacture and requirements for tight temperature control to maintain desired properties. The framework of this thesis uses modeling to evaluate selected machine parameters for the purposes of AM research to explore parameter space in a reasonably accurate and fast time-frame as a predictive tool.

Thermal and Thermodynamic Modeling of WC-Co and Mo-Metal Matrix Composites for Electron Beam Powder Bed Fusion

by
Sullivan J. Figurskey

A thesis submitted to the Graduate Faculty of
North Carolina State University
in partial fulfillment of the
requirements for the Degree of
Master of Science

Materials Science and Engineering

Raleigh, North Carolina

2021

APPROVED BY:

Christopher Rock	Lew Reynolds
Elizabeth Dickey Co-chair of Advisory Committee	Timothy Horn Co-chair of Advisory Committee

ACKNOWLEDGEMENTS

I would like to thank Dr. Christopher Rock for his guidance and patience during my many years at North Carolina State University, as well as Dr. Timothy Horn for his advice and insight. I would also like to thank Dr. Harvey West, without whom the quality of work contained herein would have certainly suffered. Thank you to all who made my journey more interesting and worthwhile.

I would also like to thank Dr. Yousub Lee, Dr. Micheal Kirka, and Dr. Ryan Dehoff of Oak Ridge National Laboratory for their work fundamental to the study presented here. Thank you to Paul Mason and Adam Hope as well for their assistance in developing a better understanding of ThermoCalc for use in this thesis. Thank you as well to the Moldino Tooling Company, LTD Japan, without whom much of this work would not have been possible.

This work was performed in part at the Analytical Instrumentation Facility (AIF) at North Carolina State University, which is supported by the State of North Carolina and the National Science Foundation (award number ECCS-1542015). The AIF is a member of the North Carolina Research Triangle Nanotechnology Network (RTNN), a site in the National Nanotechnology Coordinated Infrastructure (NNCI).

TABLE OF CONTENTS

LIST OF TABLES

LIST OF FIGURES

CHAPTER

1

INTRODUCTION

Metal additive manufacturing (AM) has grown in popularity over the last decade as a processing method for fabricating metal parts with complex geometries containing features which are difficult to produce via traditional techniques, such as forging or machining [1, 2]. Components with such complex designs are readily made with internal cavities, thin walls, and mixed structures due to the layerwise melting that is utilized by AM, and such solids as interwoven meshes can be fabricated directly as near net shape parts, without the use of expensive tooling. Thus target applications for AM parts often have very high value and complexity, while also requiring advanced properties. A significant limiting factor for these targeted, high value applications is that the parts and materials must be have well known properties, which can take over a decade for part or material redesign, depending on the criticality of those applications. Therefore a substantial quantity of the fabrication, materials, and design research over the last decade in AM has been focused on materials commonly used in markets such as biomedical and aerospace: e.g. Inconel 718 & 625, Hastelloy X, Ti-6Al-4V, Stellite 28 (Co-28Cr-6Mo) and stainless steels such as 304 and 316L [3–8].

However, there are approximately 6500 engineered alloys in use around the world on any given day; commercially, metal AM widely utilizes approximately 20 of the alloys [4, 9]. The desire for new part designs driving new materials for AM is currently a focused area of research to expand the catalogue of commercially available AM alloys, however significant challenges

exist for expansion of new alloys into AM [5, 6]. For example, alloys with high second phase content such as 731LC, MAR M247, and WC-Co, among others, are starting to be of specific interest for parts by AM for use in aerospace, energy and tooling markets due to retention of desired properties in very challenging environments such as high temperature applications or tooling [10–12]. However, most of these alloys were designed for either powder metallurgy (P/M), investment casting, or cast wrought processing routes which may result in significant processing challenges when fabricated by AM [13]. The manufacturing of components through AM necessitates a fundamental understanding of the effects of that process on the materials being used.

The characteristics of the 2nd phase (oxides, carbides, intermetallics, etc.) are critical to fabrication, such as size, distribution, morphology and coherency, among others, ultimately control the properties pre-eminent to the specific component. Generally, alloys designed for consolidation into near net shape by conventional solid state processing such as hot isostatic pressing (HIP), solid-state sintering, or semi-solid routes such as liquid phase sintering, are expected to behave differently in AM vs P/M.

1.1 High Temperature and High Content Second Phase Alloys

The most commonly described process in which a second phase is utilized in alloy development is through precipitation hardening. Precipitation hardening is process by which a second phase, or precipitate, is formed within an alloy due to controlled composition and thermodynamics, usually controlled by heat treatment processing. The intermetallic particles are usually present to improve mechanical strength through controlled particle size and distribution. These particles then impede the movement of dislocations, reducing ductility and thus hardening the material [14]. The formation of a second phase within a material can be caused by a variety of processes at wide-ranging points in the alloy fabrication process, with these precipitates being intentionally formed within the alloy, as in the carburization of steels, or can be combined through mechanical alloying, as in some powder metallurgy techniques [15]. Second phase particles can also be unintentionally formed if a material's processing parameters are non-optimal for the given alloy and composition [16].

This research will focus on two alloy systems, WC-Co and Mo-TiC, selected due to their high content of second-phase particles traditionally present, and the variety of melting temperatures for each phase. The alloys chosen are WC-11%Co, and a custom Mo + TiC MMC alloy. Traditionally, these alloys are processed via P/M under very controlled processes to gain a desired microstructure. This includes liquid phase sintering and hot isostatic pressing (HIP) in the case of WC-Co [17]. Mo + TiC is a new, custom alloy design, however similar MMC alloys

have had most widely reported production via solid state processes and spark plasma sintering to maintain the desired discrete particle additions [18, 19].

1.2 Metal Powder Additive Manufacturing

Metal powder additive manufacturing is the process by which a three-dimensional part is formed from the successive addition of two-dimensional layers of metal powder selectively bonded together in pre-defined geometries. The different techniques and the specific properties of the additive manufacturing process are covered in the literature review in more detail. But as an overview, this method of manufacture has several clear advantages and disadvantages. The benefits of using this process include the ability to produce complex shapes with internal geometries that are extremely difficult to manufacture using other methods, as well as the relatively short time it takes to produce a finished part from a 3-D CAD model, reducing the lead times typical of even low-volume commercial manufacturing processes. An additional minor benefit is the overall tendency of the AM process to reduce the generation of waste material, as much powder that was not incorporated into the part can generally be recovered and reused [1]. The drawbacks to AM include difficulty in scaling production, limitations in the part dimensions, and, of particular interest to this current research, non-traditional microstructures and very limited developed alloy systems [20].

1.3 Predictive Approach to the AM Process

In metallurgical fabrication, there are many variables that must be defined before accurate predictions and a fundamental understanding of the cause and consequence of the resultant microstructures can be realized. These include ambient pressure, temperature, material composition (both locally and in bulk), changes of state, changes of phase, solidification mechanics and crystallization, etc. These variables are also required to predict the results of AM processes; however, unlike in traditional powder metallurgy processes, many of these variables are not easily measured, or are difficult to be accurately estimated, either in practice or based on existing literature [21–23].

1.4 Summary of Research Goals

The research shown in this thesis focuses on the effect of melting powder by AM into test articles using materials not typically melted as a key component of their traditional part fabrication. The alloys selected were chosen to represent a range of compositions to evaluate

similarities in phase formation, solidification and general response to the electron beam PBF process, regardless of composition: WC-11Co and a custom Mo-TiC MMC, designed with a targeted second phase to matrix melting temperature of dT< 500C. This temperature gap is especially important in extreme conditions of AM, where process temperature is difficult to control in conjunction with other key properties, such part coherence and porosity. This work also focuses on a computational approach to predicting phase formation and the materials response of each selected alloy to EB PBF. This work focuses on the modeling methodology using thermal models, thermodynamic modeling, and model verification by experimentation to guide parameter development in AM. This work does not focus on detailed parameter development, instead it presents a generalized framework as a guide to direct parameter development and key materials considerations for successful part fabrication space.

CHAPTER

2

LITERATURE REVIEW

2.1 Physical Metallurgy Techniques

To understand the alloys to be examined in the following research, it is imperative to understand the process for which they were designed, or at times, how the process itself was designed for the alloy. Material processes today link together the inherent properties of the material system, its target application and its capability of being produced within a market value for that application [24]. Generally, alloys engineered for higher performance applications are traditionally produced by several popular routes, depending on their end use and value. These processes include Cast/Wrought, solid-state sintering, hot isostatic pressing (HIP), liquid phase sintering (LPS), and investment casting. Each technique will be presented in summary, with the important characteristics for the purposes of this research highlighted.

2.1.1 Cast & Wrought Processing

The cast process is a bulk metallurgical technique in which a metal alloy in its liquid state is poured, or 'cast', into a hollow mold, often made of packed sand or different metal with a significantly higher melting temperature [25, 26]. The cast metal forms to the shape of the mold and, once solidified, the mold is broken or separated, and the cast part is removed. This

process is often used in conjunction with wrought processes, as the cast part may not be of the dimensions, microstructure, or finish require for a given application [24]. A second casting process, investment casting, is a similar process whereby a fully melted material is poured into a manufactured mold. This process has many advantages over traditional casting, especially in terms of the available of part geometries and part surface quality; however, this process will not be specifically covered, as the fundamental mechanics are largely similar traditional casting for the purposes of the present research [27].

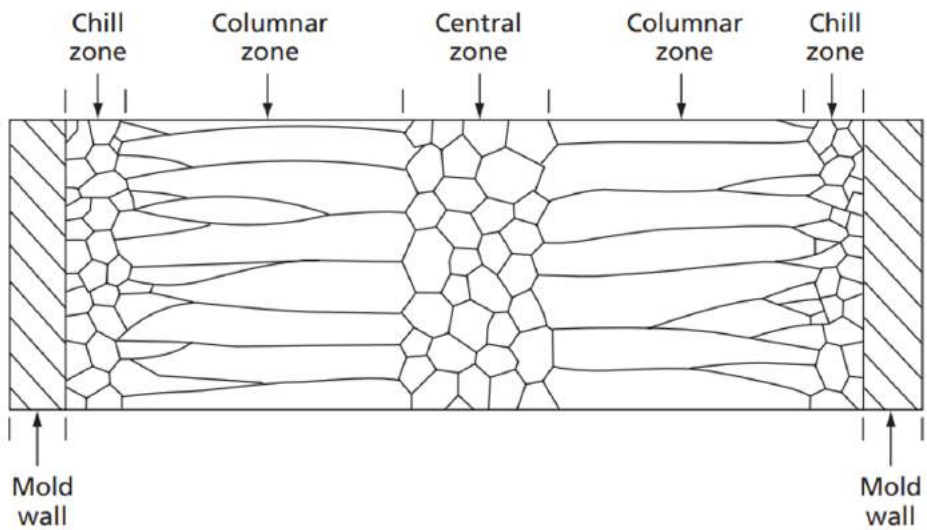

Figure 2.1 Diagram of typical as-cast microstructure, courtesy of Physical Metallurgy Principles, 4th ed.

Figure 2.1 illustrates a typical ingot cast grain structure, with the indicated microstructural zones a result of the unique solidification of castings. The chill zone, located along the mold wall, is characterized by fine, equiaxed grains formed due to the rapid nucleation caused by significant heat conduction through the mold wall, while simultaneously insulating the central molten material. The columnar zone is shown further inwards from the mold wall, and is characterized by lower grain nucleation rates and columnar grains that grew in the direction of heat extraction as the liquid interior solidified [24]. The large, equiaxed grains that make up the central zone are formed by relatively slow cooling due to the insulating nature of the surrounding chill and columnar zones of the cast material, and can be up to millimeters in size, depending on the size of the casting and its heat extraction through mold configuration [25].

Another microstructural consideration made in bulk castings is the solute distribution. For alloys with considerable amounts of solute, especially those solutes with very different

densities or solidification temperatures relative to the bulk, interdendritic regions of the casting can have a significant degree of small-scale chemical inhomogeneity or microsegregation [28]. In such cases it is often necessary to include significant homogenization time and/or deformation to produce the desired homogeneous structures and avoid deleterious phases such as uncontrolled intermetallics, carbides, and other inclusions [29].

To control these microstructural properties, cast parts are commonly then wrought, a process in which the bulk metal is deformed and shaped through a variety of techniques, including forging, drawing, cold rolling, and extrusion, among others. These processes can take place at either elevated temperatures, as with forging, or near room temperature, as with cold rolling. Each process is unique, but they all deform a material from a solid billet to a new net shape under tightly controlled and predictable conditions, and in doing so affect the internal microstructure of the product [25]. This change in microstructure can be merely a side effect of the wrought process or it can be its purpose, given that, for many applications, the typical as-cast structure shown in Figure 2.1 is not ideal [26].

Therefore, wrought processing can be used to control casting size, homogenize solute elements, refine the as-cast microstructure, or and combination therein. In the wrought process, the as-cast ingot is heated to temperatures exceeding 0.6 Tm (melting temperature) to facilitate the redistribution of of elements by solid-state diffusion as well as activate the dislocation slip systems of the material [30]. Then the material is deformed, promoting significant dislocation generation and subsequent motion for dynamic and metadynamic recrystallization. This process of heating and deformation is repeated until the desired shape and microstructure is obtained, with the possible addition of further microstructure evolution from heat treatments specifically designed to produce desired matrix phases such as controlled intermetallics or carbides to better control material properties [31].

The main advantages of cast and wrought processes are their maturity as a manufacturing method, and the relative simplicity of the processes themselves. The solidification and microstructural evolution mechanisms in such processes have been thoroughly research and understood for many decades, leading to a deeper understanding of how these processes can and cannot be used to achieve a desired final product [31]. These processes are best optimized for alloy systems that have lower melting points, for casting purposes, and higher ductility, which is valuable during wrought processing. Alloys like Inconel 718, which have very high ductility and relatively low melting temperatures of approximately 1350°C, are very optimized for cast and wrought processing, as they can be extensively deformed before suffering detrimental effects. Alloys like 718 also do not require extreme temperatures to melt, cast, and are not extremely sensitive to oxidation [32]. While complex alloys like 718 are prone to chemical segregation, the microstructures can be homogenized during processing, which improves

product consistency and reliability [33]. Alloys less suited to such techniques include high content second phase superalloys like MAR 247, IN 731, and tooling materials, like WC-Co. Such materials often contain a significant fraction of refractory metals or intermetallics, which reduce their compatibility with hot-working and can be challenging to fabricate [11, 26, 34].

The alloys typically developed for and produced by cast-wrought processing are typically good candidates for AM, and have been some of the most widely used and researched alloys in AM, due in part to good ductility and widespread use in various industries. This includes Ti-6Al-4V, a host of different steels, and nickel-based super alloys, like Inconel 625 and the aforementioned Inconel 718 [35]. These alloy groups are among the most well-understood and widely produced materials by powder-bed fusion (PBF) processes, in large part due to their having been purpose-built for full melting and resolidification as occurs during the casting process, in addition to the alloys themselves being well researched independent of the AM sphere [6]. For the AM of these materials, some consideration must be made for the AM process, as there as significant differences in the material-experienced temperatures, cooling rates, and applied forces during AM when compared to the traditional cast and wrought processes [36]; however, the obstacles to quality production of these materials are significantly reduced when compared to those alloys traditionally manufactured via solid-state methods [5, 13, 37]. Many of the alloys developed for AM have come from alloys developed for casting processes, with methods for adapting to the AM process more widely understood; however, this limits the possible materials for and applications of AM. Thus, to widen the scope of available materials and applications, a methodology for adapting materials developed for processing methods other than cast-wrought will be valuable to the AM field.

2.1.2 Solid-State Sintering

Solid-state sintering is a thermal treatment process that involves the heating of a compact (or green body) to produce a dense part with the desired properties. The value of this technique lies in the ability to form custom metal powders into complex, near net shape parts while retaining desired properties after densification. This process also allows for the manufacture of materials difficult to process via techniques such as cast-wrought due to low ductility or high melting temperatures, though the main drawback is the limited available techniques for post-processing. In this technique, the initial consolidation (or pressing) of a mass of fine powder particles into a die is typically used to form a porous green compact [14]. At this stage, the article still consists of discrete powder particles in point contact with each other, with a connected network of open pores filling in the remaining space, and thus forms the first stage of the classic four-stage sintering process, shown in Figure 2.2 [38], with the green body then

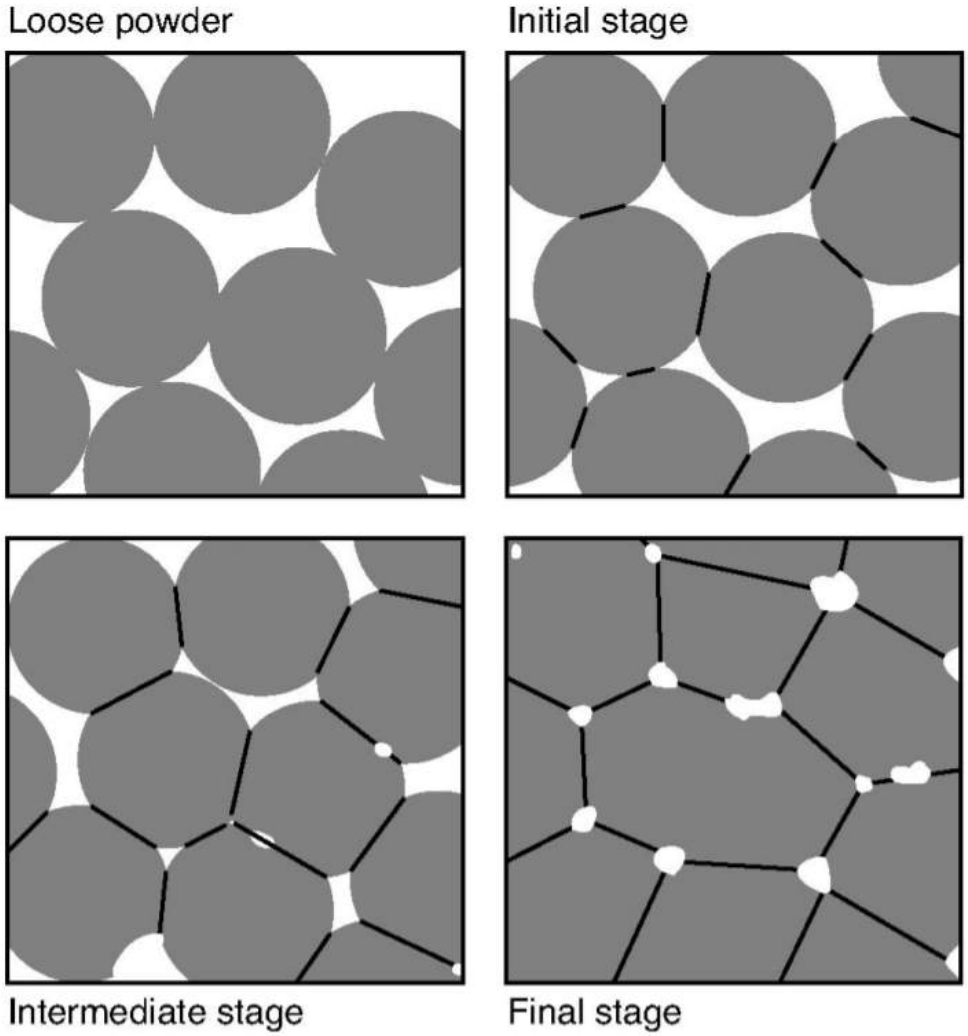

Figure 2.2 An illustration of the powder and pore morphologies during each of the four sintering stages courtesy of Woodhead Publishing.

heated, typically to 0.7-0.9 Tm, to activate atomic mobility and diffusion [14].

As this sintering process begins, necking starts to occur at the point contacts between particles through diffusional mass transport, with the second stage of sintering being defined as when the diameter of this interparticle neck is less than one-third of the particle size [39]. As sintering continues, the diameter of the necked regions increases, with the particle network becoming fully interconnected with a similarly interconnected pore network,. The intermediate stage of sintering is defined as the time during which the diameter of the necked region is between one-third and one-half of the particle size, as illustrated in Figure 2.2. The final stage of the sintering process reduces the porous network to discrete pores, and with the article consisting of continuous grain regions [38]. This process does not tend to form perfectly dense

parts, as the complete elimination of porosity relies heavily on solid-state diffusion, and thus is difficult to achieve without additional steps being taken; however, typical densities exceed 95% of theoretical [14].

This process is also unique from those previously discussed as full melting of the alloy does not occur during sintering, as the technique utilizes temperatures below the melting point, allowing for tight control of the process conditions and potentially retaining native powder properties such as distributed second phases or other novel features resulting from the powder manufacturing process [14, 39]. There is little to prevent most alloys from being able to utilize this technique, however the persistent porosity is detrimental to many alloy systems that can be produced without such porosity via other methods [40]. Additionally, due to the required pressing step in the process, the possible part geometry is limited by the mechanical properties of the powder and the thicknesses possible. A change in part dimensions also occurs as porosity is eliminated, but this can often be accounted for with a high degree of accuracy [14].

Thus a significant advantage of this process is that complex shapes can be produced from a wide range of materials without significantly altering the starting microstructure, and without deformation as is often necessary in cast products. Powder from a variety of processes and materials, from simple steels to complex ODS alloys, can be made with a wide ranging set of properties that can be retained or modified to satisfy application requirements [41]. Examples of these include steels and copper alloys with complex near net shapes for cost saving in automotive, nuclear, and electrical applications [42]. Additionally, metals or ceramic matrices with engineered second phase dispersoids such as oxide dispersion strengthened steel and Ni-based alloys have properties that can be retained satisfy application requirements [43].

Hot Isostatic Pressing, or HIP, is a metallurgical technique that shares much with the sintering process. HIP can be used by itself to manufacture parts, or in conjunction with other processes, as an additional way of controlling microstructure and other properties [44]. This process is most often used to consolidate metal powders, but can also be used for the purposes of cladding or porosity removal in cast parts [38]. As the name implies, the HIP process utilizes high temperatures and pressures to achieve the desired microstructural changes, most often being higher densities than could be achieved through other processing techniques, with the mechanisms of densification much like the standard solid-state sintering discussed previously [45].

A typical HIP cycle will begin with the period required to achieve the high temperatures and pressures required, ramping to temperatures that will allow for atomic diffusion combined with pressures that will allow for plastic flow to occur in the material [44]. After ramping, there is a 'soak' phase in which the temperature and pressure is held constant for a period of time. This is necessary as early in the process much of the densification is the result of plastic flow

within the material, which continues until the density of the part increases to the point where it can withstand the pressure without deforming [38]. After this point, various time-dependent diffusion mechanisms begin to dominate the densification rate, until a fully dense solid is made [44]. Being a sintering process, it has the similar part geometry limitations if the initial article must be pressed from powder, but otherwise a major advantage of HIP is its ability to eliminate porosity in manufactured parts, with part size being limited only by the HIP equipment available [44]. One of the few limitations on the alloys that can make use of HIP is that the process cannot take place under vacuum, and thus possible interactions between the pressure transference medium and the material must be accounted for [45].

Alloys that benefit most from solid-state sintering or HIP techniques include those that have difficult to control microsegregation or high fractions of relatively high melting point materials or high content of secondary phases, such as refractory metals like W and Mo. These techniques are also valuable for maintaining those microstructures in a finished product that would be difficult to produce via other methods, which includes many Al-based composites and some Ti-based materials, pure or alloyed. Though P/M of Ti is a viable option for many applications, few alloys exist exclusively for Ti P/M, and thus do not exhibit the same difficulty to additively manufacture as other materials specifically designed for P/M techniques [46]. Many Mo and W-based alloys, however, were specifically designed for P/M processes, and are thus prone to exhibiting significant differences in final microstructure between solid-state sintering and PBF [47, 48], and as these materials are of particular import to the present research, they are discussed in more depth later.

Given the complex nature of the process as discussed above, the materials typically manufactured via solid-state sintering or HIP tend to differ from those produced via cast and wrought processes, as the materials have largely been designed based on the requirements for each manufacturing technique. This further supports the need for a new predictive methodology for material processing in AM, as valuable materials applications are unavailable for use with AM as they were designed for very different manufacturing conditions like sintering and HIP. Furthermore the materials already developed for AM are not necessarily a useful framework as many of those alloys were themselves designed for manufacturing processes differing greatly from sintering and HIP, like cast and wrought processes.

2.1.3 Liquid-Phase Sintering

Liquid-phase sintering is a very widely utilized manufacturing method for sintered P/M products, largely due to the relative rapidity of the technique when compared to solid-state sintering. The major difference between solid state sintering and LPS is the addition of a liquid

phase, which dramatically increases the speed of the densification process by allowing faster rearrangement of particles [49]. This liquid phase is incorporated into the green body as a solid additive, and only this phase is fully melted upon heating. This decreases the temperatures required for densification when compared to the non-liquid phase of the alloy, as the melting temperature of the liquid phase is necessarily lower [50].

Starting with a green body, the process also typically follows three steps, the first of which is the melting of the liquid phase and the rearrangement of the solid particles. It is during this step that a majority of the densification occurs, and is often followed by the solution-precipitation stage [49]. In this stage the solid particles dissolve at the solid-liquid interfaces, preferentially at the contact areas between solid particles that are now wetted with the liquid phase. This dissolved phase then diffuses through the liquid to precipitate back onto the particle in regions with lower chemical potential, away from the contact areas [49]. This process results both in densification as well as grain growth. The main characteristic of the third step is Ostwald ripening, in which the grains coarsen and part density increases, with little solution-precipitation still occurring [50].

LPS is most useful in alloys with a significant difference in melting temperatures between two distinct phases, as the process necessitates the coexistence of a liquid and solid phase. This is also important as process temperatures too close to the melting point of the solid phase will increase grain growth significantly, which is generally detrimental to the mechanical properties of the material [49]. This highlights another important consideration which is the necessity of some solubility of the solid phase in the liquid phase, but not so much that grain growth is too rapid [51]. LPS is a common technique for materials with high refractory contents, like WC-Co, due to the lower temperatures required to melt the Co binder and form dense parts when compared to solid-state sintering or processes that require full melting [52].

Similarly to solid-state processing, the conditions experienced by materials in the liquid-phase sintering process are markedly different from those found in PBF processes [48, 52, 53]; though, in this instance, at least one component of the material is meant to be fully melted. However, evidence suggests that during PBF of these materials like WC-Co, as discussed later, all phases are melted, which differs significantly from the conditions found in solid-state sintering, HIP, or LPS. This full melting often leads to dramatic changes in the material, most notably unintended phases and detrimental microstructures [47].

2.2 Materials with Significant Second Phase Content

A fundamental tool in metallurgy, the use of second phases in alloys is well researched and is a critical component of many alloy systems [15]. Second phases will be presently defined

as those phases of a system which are discontinuous and embedded in a continuous primary phase, or matrix [54]. In alloys with a high degree of second phase particles, there may be significantly more second phase than primary phase, but the key attribute is the discontinuity of the second phase. Indeed, it is these alloys with a high degree of second phase particles that are often most desirable for a wide variety of high-value applications, as these alloys tend to retain critical material properties in the extreme environments often found in aerospace, tooling, oil, gas, and other energy applications [55].

High content second phase alloys are useful due to the improvement in material properties from to the addition or formation of the secondary phase within the primary phase [54]. One common and well documented use of second phases is in the precipitation hardening of steel. In this case, a dispersion of particles is formed in a material, creating obstacles to the movement of dislocations, and thus hardening the material [16]. Additionally, high content second phase Ni superalloys for use in high temperature applications, as is the case with MAR-M200 alloys. In this alloy system, the yield stress has been shown to increase with temperature, up to approximately 800C, making the alloy ideally suited to demanding environments [15].

Another example of second phase hardening can also occur in WC-Co, where WC grains within a Co matrix greatly enhance the hardness of the material. However, this hardening effect of precipitation formation is not always beneficial, as is the case with the formation of eta phase precipitates within the Co matrix. This is a case where the eta phase, a second phase itself, can form within the Co regions and harden the material. This hardening effect is detrimental as the dislocation movement through the Co matrix, now blocked by the formation of the eta phase, is the major benefit Co in WC-Co [56]. The magnitude of the effect of second phase particles depends on the specific properties of those particles and the surrounding phase, including the second phase particle size, shape, volume fraction, chemistry, and interface with the surrounding material phase [16].

2.2.1 Metal Matrix Composites

Metal matrix composites, or MMCs, are an important class of material that saw significant early development in the mid 20th century [57]. The name itself describes the three critical components of a MMC; its being a composite, with at least one of the components being a metal which forms the continuous matrix in which the other component is suspended. The matrix metal may be combined with any number of materials, such as another metal, oxide, ceramic, or even organic compounds, traditionally broken into three types of MMC's: monofilaments, whisker fibres, and particulates [58, 59].The most commonly used reinforcing particles are oxides, nitrides (e.g. TiN, SiN), borides (e.g. TiB), and carbides (e.g. WC, TiC), due to their

tendencies to have high melting temperatures, and the value of MMC's in high temperature applications [57, 58]. This also means that MMC's can be high content second phase materials, as is the case with commonly used automotive ODS alloys like Al/Al2O3 [34].

Early research into MMC's focused on the development of monofilament-reinforced high performance materials based on matrices of aluminum and titanium, however due to high cost and process complexity, attention shifted to the latter two categories; whisker fibres and particulates which are discontinuously reinforced MMC's [60]. An example of such a discontinuous alloy, Fe-TiC compositions are doubly relevant to the current research. This material can be formed by liquid metal-carbide mixing as well as reactive casting methods, with TiC additions showing the potential for increasing the hardness of the Fe matrix while retaining its ductility [61]. Additionally, research has shown that the TiC precipitation occurs in these alloys due to higher affinity of titanium to carbon, but also due to TiC precipitating at higher temperatures than iron carbides [62].

Many MMC's are processed by LPS, and the process is equivocal to non-MMC materials as discussed previously [57]. An additional consideration with MMC's, however, is the relatively high temperature of the constituents, as it has been reported that elevated temperatures are correlated with the formation of deleterious phases and inhomogeneity [63]. These detrimental microstructures are formed from the reaction of the secondary phase with the matrix, and can be controlled via compositional changes or careful temperature and process control [63].

A pertinent example of this in practice can be found in Titanium Zirconium Molybdenum (TZM) alloys, a system adjacent to the Mo-TiC alloy investigated in this research, as the matrix metal is Mo, composited with Zr, Ti, and C [64]. The processing of TZM begins with vacuum arc melting, followed by tightly controlled thermomechanical treatment, as the controlling of the microstructure is very difficult [19]. Many TZM products are formed through sintering and then mechanically worked, again under tightly controlled conditions to form the desired microstructures; though, despite this control, the influence of the second phase on microstructure is not well understood [64]. The effect of Ti, Zr, and C additions however, is reported to be the inhibition of dislocation movement through their dispersion in the matrix, similar to the precipitation hardening of steel discussed previously [65]. Secondarily, the are reported to inhibit grain growth, due to both their tendency to form along Mo grains boundaries as well as their incoherency with the Mo matrix, due to the large relative difference between lattice constants [66]. Thus there is significant importance in not just the properties of the added components, but how they interact with the matrix.

The two materials that are the focus of the current research are WC-Co and Mo-TiC, chosen in part due to the reported difficulty of the additive manufacture of these materials [67, 68]. In the traditional processing of WC-Co and Mo-TiC, the second phase remains discrete and

typically manufactured by powder metallurgy processes like LPS, press and sinter, spark plasma sintering, and HIP techniques [47, 69]. These process are necessary, as opposed to equilibrium melting, as such melting would destroy the presence of second phase particles and form unintended phases without significant post-processing [19, 64, 70]. Additionally, the difference in melting temperatures between the two components of each alloy will be important, as the melting temperatures of all components are also relatively high, meaning extreme energies and temperatures may need to be generated and imparted to the materials during processing via any techniques, including AM. This has often been shown by the literature to be difficult to reliably control, and can have detrimental effects on final part properties and microstructure. [68, 71].

2.3 WC-Co System

2.3.1 WC-Co Atomic Structures and Phase Constituents

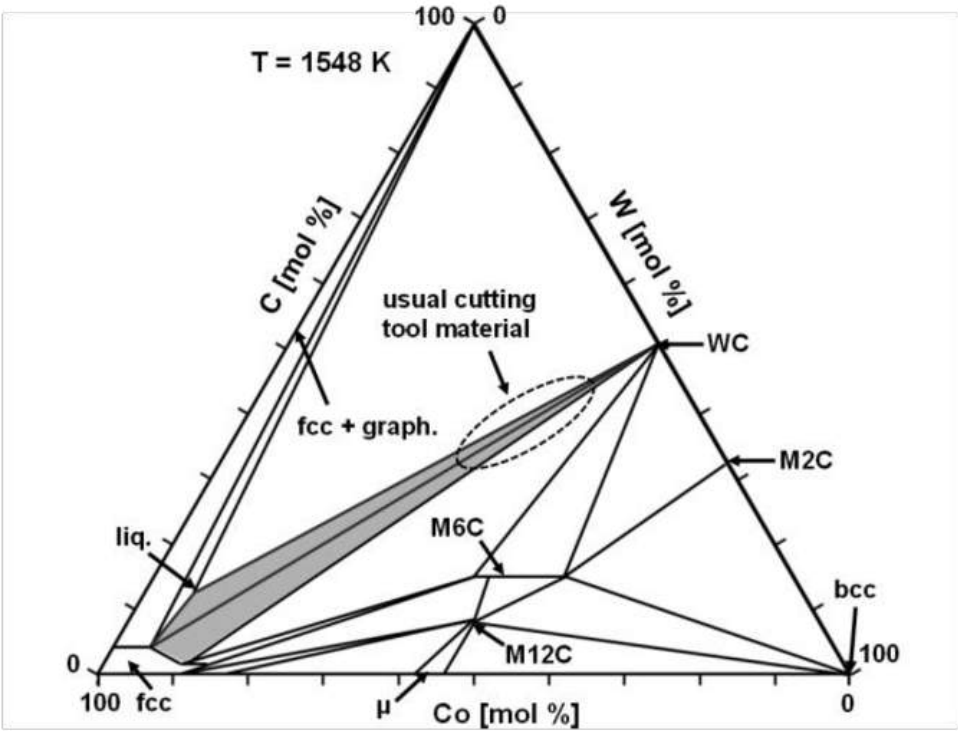

Figure 2.3 The isothermal section of the Co-W-C ternary phase diagram at 1548 K, courtesy of Springer-Verlag, Metallurgical Transactions.[72]

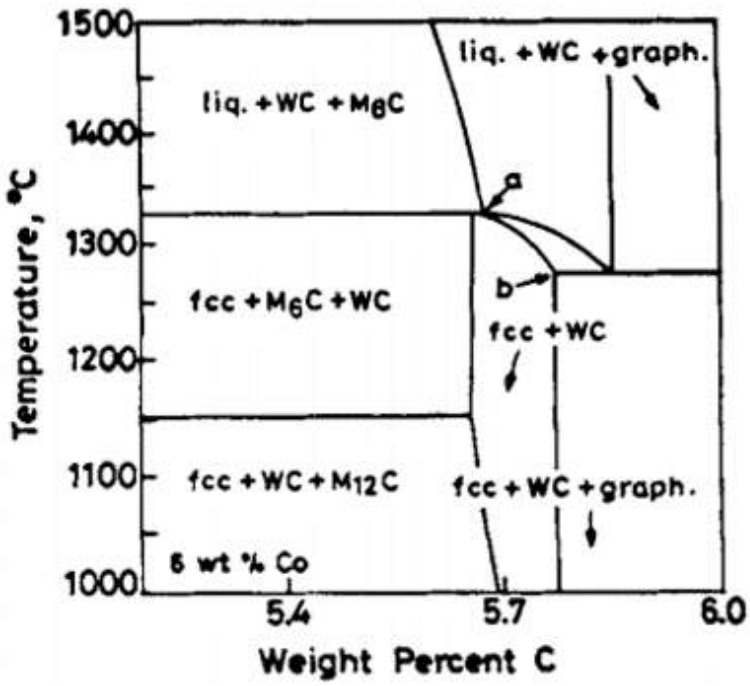

Figure 2.4 A section of a Co-W-C pseudo-binary phase diagram, courtesy of Springer-Verlag, Metallurgical Transactions.[72]

As a MMC, the basis of WC-Co is the metal matrix of Co that surrounds the individual WC grains, with the Co phase acting as a binder and providing greater toughness to the very hard, wear-resistant WC grains. WC forms a primitive hexagonal close packed (HCP) crystal structure at temperatures lower than 2525°C, with C atoms occupying the positions 1/2, 2/3, 1/2 in the lattice [72]. The relationship between the solubility of C in W is naturally very closely tied to temperature, with the equation for that solubility as follows:

$$ln(C_{\max}) = 4.67 - \frac{15.0x10^3}{T} \tag{2.1}$$

where T is the temperature of the bulk [73]. The leads to a maximum solubility of C in W as 0.7 at% at the eutectic temperature of 2710°C. Additionally, as per the shown phase diagram, the formation of the carbide W_2C will occur in regions that are deficient in C.

There are two structures of cobalt, a close-packed hexagonal structure stable at temperatures below around 420°C, and a face-centered cubic structure stable at higher temperatures, the exact allotropic transformation temperature depending on the purity. One characteristic of being in solution with tungsten and carbon during sintering is that this cubic phase is typically preserved at room temperature, and cannot be transformed via annealing [74]. Figures 2.3 and

2.4 show a W-C-Co ternary phase diagram and binary phase diagram, with the latter targeted between 5 and 6 wt% compositions, in which a great many of the viable WC-Co reside. At low concentrations of Co, the compositional region in which typical commercial compositions are found between 5.65 and 5.8wt% C as labeled on Fig. 2.3, and thus small changes in either global or local compositions can have significant effects on the phases formed during and after processing [72]. The pseudo-binary phase diagram presented in Figure 2.4 shows a similar sensitivity to changes in C concentration, as the labelled 'fcc+WC' region is closely bounded on the left by regions with eta phase formation and on the right by regions with graphite precipitation, both of which are detrimental to material performance. For compositions typical of 11% Co cutting material, the WC-Co compositions are typically 5.75 wt%C [72].

Deficiencies in carbon can form W_2C, but when alloyed with Co this same deficiency can also lead to the formation of two eta phases, Co_6W_6C and Co_2W_4C [72]. These phases are shown in the ternary phase diagram in Figure 2.3. These phases are detrimental to the properties of the material, as they form in Co-rich regions, decreasing the ductility and thus the toughness of the material [49, 72, 73]. Similarly, it can also be seen from Figure 2.4 that excess carbon also produces an undesirable phase, in this case in the form of graphite precipitations within WC grains. These formations also decrease the toughness, reducing the ability of the WC grains to withstand cracking and decreasing the hardness of those WC grains [49, 72–74]. It has also been shown that Co content can have a significant effect on manufactured part properties, as increased wt% Co corresponds with a increase in mean WC grain size, which itself effects the material properties as discussed previously [52].

2.3.2 WC-Co Processing

WC-Co is generally produced by solid-state sintering or LPS, wherein the Co phase acts as a binder and provides for faster densification through its facilitation of WC grain reorganization as well as mass transport. Typically processed at around 1450°C for hours, the LPS of WC-Co works very similarly to the LPS of other materials [75]. With the two components interspersed with each other, the component with the lower melting temperature becomes liquid, in this case the Co. This liquid phase then wets the surrounding WC particles and allows for both the rearrangement of those particles and their coarsening [75].

The typical cobalt content for commercial alloys range widely, from 5-25at.%, with properties like grain size, hardness, and toughness changing as a result of this change in compositions [76]. In general, the eutectic temperature decreases as Co content increases from 5at% to 20 at%, after which it begins to increase again, as illustrated by the pseudo-binary phase diagram for WC-Co shown in Figure 2.4 [70].

Rearrangement is facilitated by the decreased friction between the WC particles in the liquid Co, and the WC grain coarsening and homogenization is due to the limited solubility of W in Co, allowing for significantly increased rate of atomic transport between WC grains [77]. The benefits of LPS are low sintering temperatures (relative to WC melting temperature), more rapid densification and homogenization, and improved microstructural properties, while maintaining the high densities required of high-performance materials like WC-Co [77]. These relatively low sintering temperatures and rapid densification arise from the need to only melt the binding phase (Co).

The HIP of WC-Co is a common processing step used in the WC-Co system to produce high density parts, either in conjunction with previous steps, such as sintering, or as the sole densification technique [78]. The HIP process in WC-Co can increase the densification rate and final part density beyond that which is possible with LPS, and can be utilized to collapse gas-filled pores formed through vapor generation or pore coalescence [49, 79, 80].

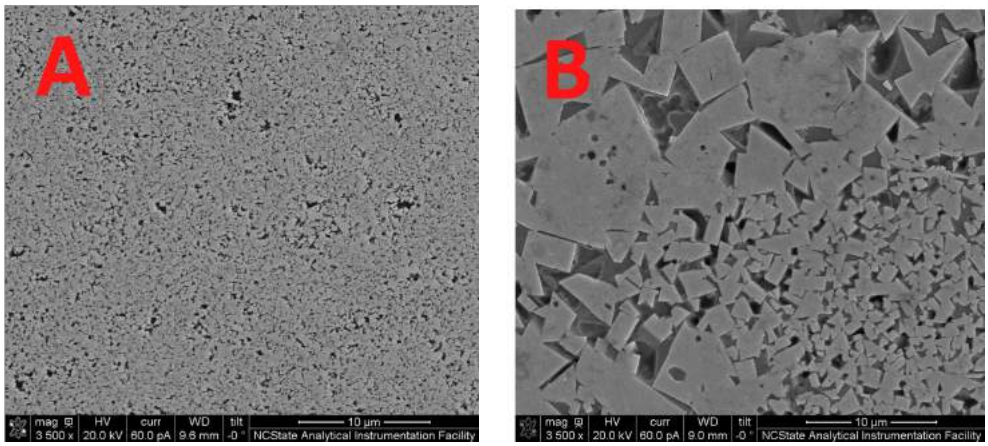

Figure 2.5 SEM micrographs of A) traditionally manufactured WC-Co material via sintering and B) AM produced WC-Co microstructures

Precise control of the sintering of WC-Co is critical to achieving the desired properties of the material. Figure 2.5 illustrates a common problem in WC-Co processing, which the rapid growth of WC grains may occur during processing. This abnormal growth is also seen in unoptimized sintering processing and in the absence of additives to control grain growth and 3D printed WC-Co of various compostions where the growth corresponds to the movement of the WC-Co size distribution with process parameters such as temperature and sintering time [81]. This issue is exacerbated by high temperature, high pressures, and/or low local or bulk Co content [76].

Dissolution-precipitation of W solute in liquid Co appears to one of the processes contributing to WC grain growth, and is a rapid step [77]. Additionally, in sintering studies relating to WC-Co, this growth is controlled not by diffusion, but limited by the precipitation step, and likely itself limited by mechanisms of nucleation-growth [75].

2.4 Mo-TiC System

2.4.1 Mo-TiC Atomic Structures and Phase Constituents

Similarly to WC-Co, Mo-TiC is a MMC where the ductile phase, molybdenum, comprises the metal matrix in which the harder TiC phase is suspended, forming a particle reinforced MMC. Molybdenum forms a body-centered cubic (BCC) crystal structure in its pure form, wheres TiC forms a diamond cubic structure at room temperature, with lattice parameters of 0.315nm and 0.433nm [82]. As melting temperatures play an important role in all metallurgy process, it is also essential to be cognizant of the relationship between the two alloying elements, as in WC-Co. Pure molybdenum melts at 2623°C, while TiC melts at 3160°C [83]. This results in a gap of approximately 500°C, which is half that of the gap in melting temperatures between WC and Co, likely resulting in a smaller processing window to prevent the melting of TiC.

Furthermore, observation of the molybdenum cubic lattice in TiC-containing alloys shows negligible difference in lattice parameter when compared to pure Mo, suggesting a low solubility of titanium in molybdenum. Conversely, observation of the TiC crystal lattice has shown significant solubility of Mo in TiC, up to 25 mol.% in compositions of more than 75 mol.% TiC [84]. Additionally, the effect of combining molybdenum to TiC has also been found to lower the melting temperature of TiC, with the lower bound found at the eutectic temperature of 2175°C [85]. An important element of the current research will be the methodology controlling the maintenance or development of discrete TiC particles in the bulk material, despite its similar melting temperature to Mo.

This ternary system also leaves the possibility of the formation of molybdenum carbides, should the TiC dissociate and the carbon diffuse to Mo-rich regions. This would likely form MoC or Mo_2C, the two most stable stoichiometries [83]. Within these phases, certain configurations are regarded as more stable than others, with the orthorhombic beta-Mo_2C phase having been experimentally found to be more stable than hexagonal a-Mo_2C [85]. For MoC stoichiometries, hexagonal (a-MoC) and face-centered cubic (d-MoC) are both possible to form, though both have similar properties to be equivalent for this experimentation [82].

Studies involving the sintering of ternary Mo-TiC alloys have found that during this sinter-

ing process, interdiffusion between Mo and TiC occurs and a typical cored structure can be observed where the rim consists of [18]. One of the challenges of 3D printing both the WC-Co and Mo-TiC systems is, in trying to better reflect traditional PM processes, they are generally not fully melted as required by AM processing for reasonable density [69, 86].

2.4.2 Mo-TiC Processing

Pure Mo is used in a variety of products such as missile and aircraft parts, high temperature furnaces, power generation, protective coatings, thermocouple sheaths, and electronic filaments where the components are generally fabricated by powder metallurgy or Arc casting processes [87]. Novel Mo-based MMC's have been less reported; however, it is desirable due to an extremely high melting point, along with a low coefficient of thermal expansion and good thermal conductivity allows for the material's strength, corrosion resistance, and creep resistance to be maintained even at very high temperatures. The targeted application is where the TiC helps Mo maintain its desired creep and strength at extreme operating environments, with a unique property the further extends the applications of Mo alloys is the low induced radioactivity Mo experiences, making it an excellent material for use in nuclear reactor components [88, 89].

The main drawback for Mo is the difficulty of manufacture as, in addition to maintaining material properties at high temperatures, Molybdenum and Mo-based alloys are highly sensitive to degradation from small interstitial contaminants like carbon, nitrogen, and oxygen, and can be detrimental even at very low concentrations [84, 88]. These impurities, as well as the extreme temperatures required for forming Mo, strongly influence fabrication processes and resulting properties [90].

Other characteristics such as heat treatment, stress state, and grain structure have important effects of the properties of pure Molybdenum, and can significantly influence formability and resulting properties. For these reasons, researchers have sought to improve its toughness, and TiC has been shown to do as much. Parts manufactured from mechanically alloyed Mo and TiC have been shown to exhibit a lower DBT, higher toughnesses and significantly reduced grain growth, all of which make this material more useful in its potential applications [18]. Given the highly desirable properties of this material system, a viable manufacturing path, such as could be found in AM, would introduce tremendous value in many of the described advanced materials applications. One potential downside is, even in very low TiC concentrations, both recrystallization and grain growth are prevented by those TiC additions [18].

2.5 Summary of Powder Bed Fusion

Powder Bed Fusion, or PBF, is a term used to describe a variety of manufacturing techniques that exist under the larger umbrella of additive manufacturing [1, 4, 20, 35]. These techniques are bound by a similarity in the input material, powder, and the strategic melting, or fusion, of this powder to create a manufactured part. As an AM process, this technique utilizes a layer-by-layer approach, with a desired three-dimensional part divided into a continuous series of two-dimensional slices. These slices are then manufactured sequentially, one on top of the other, during PBF, usually with the first layer adhering to a base of bulk metal, usually a start plate of similar or non-detrimental composition material. Each layer consists of powder of a chosen alloy, with particles typically ranging from 10-100 microns and depending on the specific implementation of PBF, and where this powder is spread in a thin (20-70 microns) layer that covers, at minimum, an area that encompasses the maximum cross sectional area of the 3-D part [1]. This layer of powder is then typically melted by a high-power laser or electron beam, in the desired pattern that corresponds to the 2-D slice, adhering to the previous layer, and after solidification, the powder for the next layer is similarly spread, and then melted, typically using a high-powder laser or electron beam, in the desired pattern that corresponds to the 2-D slice, adhering to the previous layer, and after solidification the process is repeated [4]. A key to densification of the layers is that the melt pool generated is typically 3-5 layers deep such that there is adhered continuity in the fabricated z-direction [20].

2.6 Effect of AM on Non-Cast/Wrought Alloys

Commercially available alloys for metal AM such as IN 718, SS316L and Ti-6Al-4V are widely manufactured in AM because 3D printing and cast-wrought processing share important material property requirements [36]. Generally, alloys produced by cast/wrought processing require compositions suitable for full melting and solidification and reasonable ductility for shape processing and working [35]; since 3D printing requires melting for powder layer adhesion, it produces a liquid melt pool (on a much smaller scale than Cast/Wrought) and often undergoes significant thermal stress due to thermal cycling [91]. Therefore, materials printed using PBF materials generally require ductility and the ability to be fully melted without significant deleterious phase formation and post processing. Binder jetting is the exception to this; however, the process requires the use of a binder agent which may contaminate or otherwise depreciate the material properties, often requiring significant post processing to produce a finished product [35].

Newer material systems such as WC-Co and refractory alloys have been of specific interest

for parts by AM for use in demanding applications such as aerospace, energy, and tooling markets due to their retention of desired properties in very challenging environments [20]. As these alloys were designed for the techniques discussed previously that differ greatly from AM, such as LPS for WC-Co and spark plasma sintering for Mo-based alloys, there have been significant processing challenges found during fabrication via AM in contemporary studies [66, 71, 92–96]. While there has been some research into the use of WC-Co in AM, there have been very limited research looking specifically at the AM of Mo and its alloys. What studies do exist, for both alloy systems, often make use of a laser system for the processing of the material [67, 71, 96]. This process is, as previously discussed, a comparable but not identical process to EBM, and can cause the material being processed to exhibit unusual or detrimental features in the parts or on the used powder [97]. Due to this lack of literature data that deals directly with these alloys in EBM, especially Mo and its related alloys, research that investigates similar alloys will have to be examined for its potential value to the current research. This includes TZM studies for Mo-MMCs and studies or different Co compositions for WC-Co, and how these systems may inform the specific alloys used in the present research.

2.6.1 AM of WC-Co

Given the potential benefits of creating complex part geometries, with reduced post-processing, the AM of WC-Co has been the subject of increasing research in recent years. However, due to the nature of PBF AM, there has been very limited reported successful attempts in producing WC-Co with properties and microstructures similar to traditionally manufactured WC-Co. Much of the existing research focuses on the laser-based PBF process, with some additional studies also looking at WC-Co in EBM and binder jet AM [47, 96, 98]. Binder jet AM is a solid state process that uses a binder to adhere the layers together, instead of melting, such that it produces a green body capable of complex geometries [98]. However, the green body requires densification with some significant drawbacks including shrinkage, residual porosity, composition changes due to the binder, and detrimental redistribution of Co during sintering that have been reported after sintering [75, 76]. These limitations to the binder jet process make the PBF process of greater interest to the present research, especially for applications that benefit from little post-processing.

Published studies of laser PBF [6, 47, 70, 96, 99–103] and EB PBF [95, 104] looking into the additive manufacturing of WC-Co have found several trends to be consistent throughout. On a macroscopic level, the high thermal gradients combined with the brittle nature of the material itself often leads to part cracking and layer de-lamination due to high residual stress [6, 99]. The risks of this are especially common in laser PBF process due to ambient process conditions;

however, cracking and de-lamination has also been report in EB PBF with temps ranging from x-y, in part due to thermal cycling that is common in the EBM process caused by the heating before and during melting, followed by the cooling that occurs between layers. This problem is also related to alloy composition, as the use of high Co compositions has been shown to significantly reduce part cracking [47].

Porosity is also a common observation in AM WC-Co parts, and has been found to be closely associated with energy density of the beam [99], with both spherical and irregular porosity shapes being found, depending on their hypothesized formation mechanisms [98]. Larger, irregular pores tend to be the results of layer defects or insufficient melting, while smaller, spherical pores tend to be the result of the either the decomposition of residual moisture or additives in the powder and/or the evaporation of the Co binder [96].

As is the case with many alloy systems in AM [35], there is a positive correlation between fabricated part density and energy input in the WC-Co system [96]. Uhlmann et al. prepared a process map from a number of published studies in the laser PBF of WC-Co and found energy input to be a vital parameter for dense parts. Energy density also affects numerous other part properties such as composition, likely by evaporation of Co, as well as the formation of different phases, and grain size. In both laser PBF and EB PBF, WC grain size has been shown to increase during the PBF process in proportion to the energy density of the heat source [47], and with grain enlargement even being seen in very low energy density experimentation as in other studies. In investigating the EB PBF of WC-13%Co via EBM, Konyashin et al. found that abnormal grain growth was commonly observed in produced parts, with grains growing at times by a factor of 30 or more relative to the initial feedstock [95]. This is especially significant given the very short time during which the material is at a temperature high enough to sustain a liquid phase. In the investigation of grain size on the resulting hardness of WC-Co, Upadhyaya et al. found that as average WC grain size increased from 0.5um to above 3um, Vickers hardness decreased from 2000 to 800 (HV) [70]. The exact mechanisms behind this increase in grain size is not yet fully understood and they will not be a focus of the present research.

The additional effects of energy density on material properties further complicate the processing of WC-Co, with the atomic composition of both Co and C shown to decrease after processing via AM, with the degree of change increasing as the energy density of the applied energy increased [103]. Additionally, increasing the energy density of the laser also increased the relative composition of both W2C and eta phases, even when these phases were not detectable in the initial powder feedstock, and are associated with depreciation in material properties [47, 76]. Hardness was reported to increase with increasing energy density due to the formation of relatively large quantities of the hard, brittle W2C and eta phases, as well as the combination of enlarged WC grains, increased density of the material, and reduction of the ductile Co binder[47,

70]. Thus, it can be said that WC-Co hardness and density generally improve with increasing energy density, with these improvements being largely at the expense of the alloy's toughness.

The retention of traditional material properties are difficult to maintain due to the formation of a melt pool during PBF, which differs greatly from solid-state or LPS processes. Such complex changes to the material processing are difficult to isolate and control for specifically, which has been a major obstacle to the greater application of WC-Co alloys in AM, as well as other similar, high content second-phase materials [100–102, 105]. Overall, a vast majority of the literature has focused on investigating the effect of specific parameter sets on specific alloys, as opposed to more generalized methods of deriving parameter sets, leaving a significant gap in the research for the results of the current experimentation.

2.6.2 EB PBF of Mo-MMCs

The additive manufacturing of MMC's has been of great recent interest due to the possibility to make near net shape materials with a range of properties. MMC systems of varying matrix compositions have been studied including Al, Ti, Ni, Fe and their respective alloys with the added second particles ranging from carbides (TiC, ZrC), oxides (Al2O3) and nitrides (B2N, TiN), among others [62, 71, 87, 106, 107]. The goal of most of these studies generally is to strengthen the materials with targeted property improvements [62, 71, 106]. Mo-TiC is of particular interest for methodological development due to the inherent difficulty of additively manufacturing refractories as well as multi-component systems in which the melting temperatures for the components are similar. These challenges require thermal data to control and predict phase formation and internal microstructures. Maintaining discrete TiC particles within a Mo-rich matrix is vital to achieving the intended properties of the system, and requires similar control and prediction of phase formation and thermal information.

Studies involving pure Mo have reported significant cracking that occurs throughout the material during fabrication, as well as observing the existence of crack networks within manufactured AM parts, especially when using laser PBF due mainly to the low temperature ductile to brittle transition temp (DBTT) [66, 69]. It has been reported that laser AM, specifically, is challenging for PBF fabrication of pure Mo because the inert atmosphere used in LPBF has a tendency to form a low O2 environment which causes oxidation of pure Mo up to 800 ppm preferentially along the GB giving rise to grain boundary cracking and instability in the DBTT [69, 86]. Density of Mo articles by AM have been reported with a wide range of values, from 42.2% to 99.1% by laser PBF where porosity is due to the very high melting temperature necessary to melt Mo [69, 108].

There is limited literature that exists of 3D printing Mo alloys containing carbides, if not

specifically TiC, and can be used to inform the effect this type of addition has on the alloy as a whole. Adding carbon to Mo alone have been shown to form Mo_2C-rich regions between large Mo grains when additively manufactured, meaning the possibility of TiC additions forming these same carbides if it undergoes a similar process will need to be considered [66, 85]. As previously discussed, the Mo-based alloy TZM (Titanium Zirconium Molybdenum) is a commonly researched alloy that is closely related to Mo-TiC, and typically has a nominal composition of Mo–0.5 Ti–0.1 Zr–0.02 C (wt. %), and greatly expands the scope of current related literature [64, 65, 86, 87, 109].

In spark plasma sintering, this alloy has been shown to form complex carbides, typically located along the boundaries of the larger Mo grains, with those grains being much smaller post-process than pure Mo [107]. Thus, the literature reports that the mechanics of various carbide formations will be an important consideration in the present research, especially if temperatures required exceed the melting point of TiC, as in the case of the spark plasma sintering of TZM [109]. In the welding of TZM lap joints by fiber laser, large-scale porosity was commonly observed, likely caused by gas evolution and/or keyholing [65]. The microstructure in the interaction area of the laser beam was consistent with microstructures seen in many other materials, with large, columnar grains surrounding smaller, more equiaxed grains in the solidified melt pool, and small, equiaxed grains formed in the HAZ [65, 109].

Studies have also reported on the 3D printing of non-refractory MMC alloys that utilize TiC as a second phase, informing what structures one might expect to form due to the TiC inclusion in the Mo-TiC system. There have been a number of reports on the PBF of Al-TiC alloys, however the large difference in melting point between Al and TiC likely won't reflect the conditions expected during AM of Mo-TiC [63]. Looking at studies that include materials with more similar melting temperatures, the TiC additions tend to significantly change in morphology. Other reports that also included TiC found little to no irregular TiC structures [110]; however, these studies were researching the behavior of TiC within multi-component alloys such as Inconel 625 and other alloys with lower bulk melting points that either Ti or Mo, and thus may not be indicative of the conditions that the manufacturing of Mo-TiC may experience. Pribytkov et al. combined TiC with pure Ti at a 50/50 vol% ratio, the TiC was significantly altered, forming irregular, dendritic structures differing greatly from the initial powder feedstock, with specific morphologies depending on whether laser-based PBF or electron beam PBF was used to produce the samples [111]. The similarities of this research set-up with the one utilized in the present research, including their use of mechanically alloyed powder, without additional ternary elements, makes these structures of particular interest, given their likelihood of forming.

A portion of the present research sought to further previous work investigating the Mo-TiC

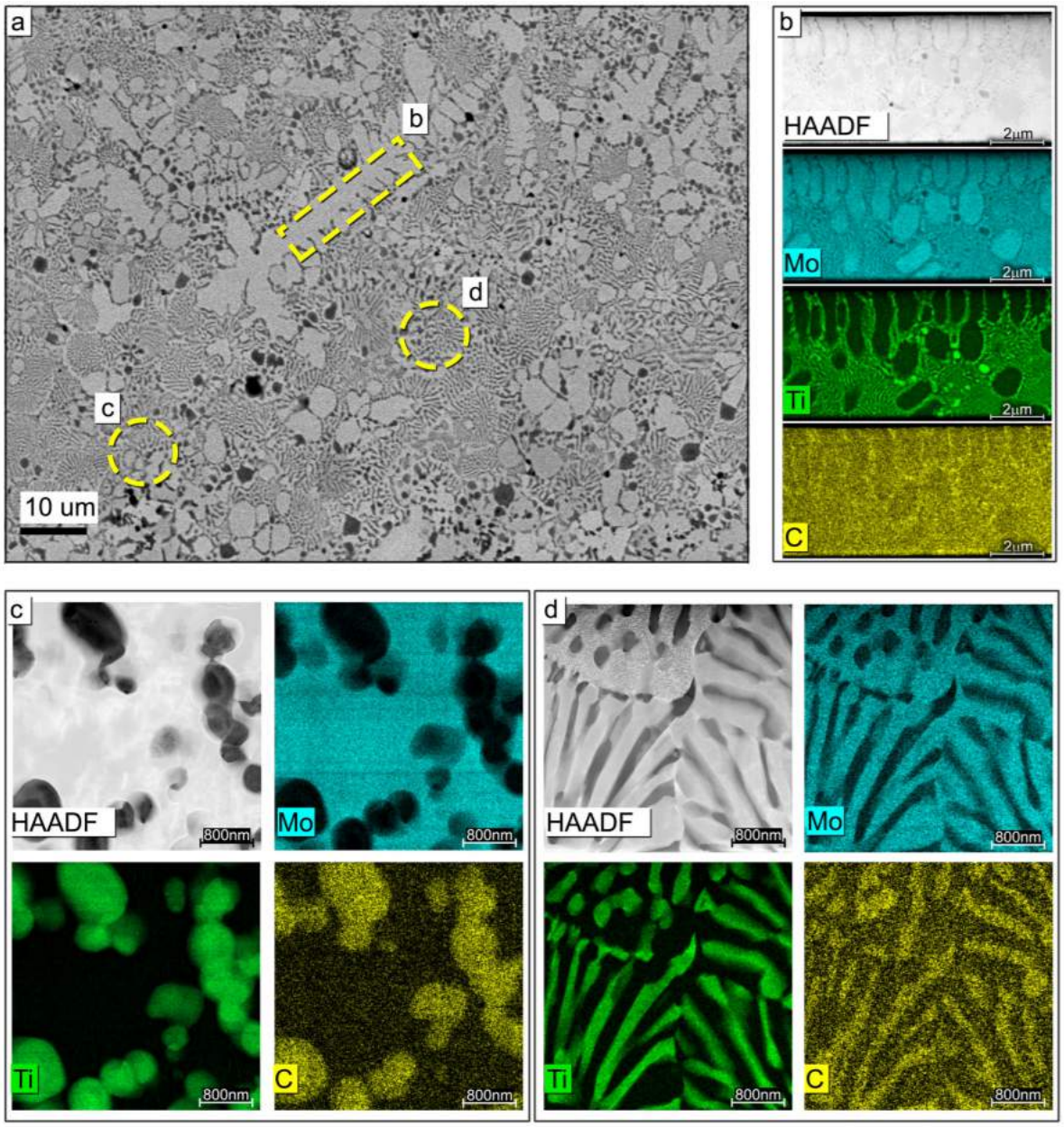

Figure 2.6 Structures observed from EBM of Mo-10.5Ti-2C composition, including (a) SEM at 1000x of mixed structures, and the STEM and EDS of (b) dendritic Mo with interdendritic Ti and C plus a fine lamellar TiC region with very small discrete TiC particles, (c) Mo matrix with discrete TiC particles, and (d) eutectic structure. Courtesy of Springer JOM.[112]

system in EBM [112]. The authors manufactured both Mo and Mo-TiC in an EB PBF system, with the most commonly observed structures from previous research shown in Figure 2.6. This figure presents a subset of the results presented by the study, with Figure 2.6a being a representative SEM image of the mixed structures found in the as-fabricated Mo + TiC MMC layers, with specific regions highlighted and examined further in Figures 2.6b-d. Overall, Figure

2.6a shows regions of lamellar eutectic structures, dendrites, as well as discrete TiC particles. STEM imaging and elemental identification by EDS was performed on the highlighted regions, after ion beam cross-sectioning, and are shown in the Figure inserts 2.6b-d. Figure 4.2b reveals dendritic Mo with an interdendritic Ti and C structure, plus a fine lamellar TiC region with submicron, discrete TiC particles. Figure 2.6c shows a Mo matrix, also containing discrete TiC particles, which was the structure expected by the authors prior to experimentation. Figure 2.6d confirms the observed lamellar structure to consist of alternating lamellae of TiC-rich and Mo-rich phases.

These results were also examined in conjunction with thermodynamic phase modeling, including generated ternary phase diagrams and Schiel calculations, and were found to largely match the phase observations. However, the authors also reported that based on these generated ternary phase diagrams and Schiel calculations that the process was extremely sensitive to changes in temperature and composition. One of the key considerations when developing novel material systems for 3D printing is the driving force between the desired microstructure, related compositional effects and properties desired after AM. In the case of the two material systems described here, it is anticipated that 3D printing by PBF may significantly change the desired microstructure. Process modeling is often deployed as a technique to predict important aspects of material processing and outcomes including thermal modeling and cooling rates [11, 113, 114], thermodynamic modeling for phase prediction [115], computational fluid dynamics for melt pool physics [116], microstructure and properties [117], among others.

2.7 Model-based Approach within PBF

Given the extreme conditions present during the AM process, an accurate understanding of those conditions is paramount to the successful development of a workable manufacturing procedure for a given material composition. In-situ information is especially difficult to obtain in AM due to the very high temperatures, small melt pool sizes, and very short time scales. In-situ thermographic microstructure monitoring is possible, but requires expensive, specialized equipment, with a very involved calibration process, as described by Raplee et al. In this paper, the authors develop a method for calibration of a FLIR 7600 to the widely varying emittance to detect melt pool imperfection and improve repeatability for the detection of porosity and other microstructural features [118]. Given the complex nature of this process monitoring technique and the significant investment, a FEM approach was selected to approximate the informational capabilities of such a monitoring method.

A material's specific composition and properties must be taken into account, and thus a new parameter set must be developed, or at the very least confirmed, for even minor changes

to either the starting or desired final properties of the material [119]. The advent of integrated computational materials engineering (ICME) gives a methodology for achieving these parameter sets in a manner that has the potential to be far more efficient than the current methods commonly used at present [120]. The current research presents a systematic model-based approach that allows for the design of material parameters in AM as they relate to the thermal and compositional properties of that material. Combining simplified FE thermal modeling to predict temperatures and a thermodynamic program to predict compositions and material phases as a result of those temperature profiles, the material and microstructural properties of a material as a result of PBF can be rapidly estimated to guide parameter development.

Finite element simulation of thermal fields in AM has been a growing field of research in the AM community, with the obvious benefits of better understanding of the beam interactions and the melt pool conditions, at the cost of computational resources. As such there is the trade-off between computationally intensive, high resolution, dynamic FE simulations and less computationally expensive, static models with additional assumptions made [121]. Zhang et al. use FEA to describe the effects of beam velocity, power, and line offset on temperature distribution during PBF, with the model simplified by only accounting for heat convection between the part boundaries and atmosphere [122]. Additionally, and dynamics or material phase changes were ignored in this and similar studies [91, 122, 123]. Matsumoto et al. utilized a similar FE model to propose an FEA for a single layer melting in PBF, with the model calculating the temperature distribution within a solid, single layer [124]. A fully-coupled thermal and CFD model of laser PBF was performed by researchers at LLNL to investigate melt pool properties, and thermal modeling has been shown to be predictive in certain situations and materials [125–128]. The present research opted to use less computationally intensive approach, similar to those employed by Zhang et al., Huang et al., and Matsumoto et al. As the goal of this research is rapid material parameter development, such simplicity was valuable, as more computationally complex models can increase computational time or expense by several orders of magnitude [119]. As the model utilized in this research does not consider the fluid dynamics of the melt pool explicitly, process parameters from the literature are used to account for such properties implicitly [127]. Originally developed as a thermal framework to predict hot cracking behavior during the EBM of IN 718 during EBM, researchers evaluated the effect of geometry, process parameters, and microstructure to minimize cracking [11, 127]. The described framework consists of uncoupled low fidelity heat transit model for the thermal analysis, and in practice, this style of FE thermal modeling has produced positive results in numerous studies and material systems [101, 129]; however little focus has been given to less traditional material systems such as high volume percent second phase materials, as is the focus of the present research. Thermal modeling only provides part of the necessary information for predicting

the effect of melting during PBF, however, and analysis of the predicted effect of temperature profiles on the formation of phases is also important [129].

To do this requires accurate thermodynamic, phase formation modeling, which is provided in this research by the program ThermoCalc. ThermoCalc is a thermodynamic and diffusion simulation software package that allows for the generation of many diagrams based on an arbitrary elemental composition. The diagrams able to be generated include; binary/ternary phase diagrams, Schiel plots, T-T-T diagrams, and equilibrium phase diagrams, allowing for a broad analysis of the material response [130–132].

CHAPTER

3

EXPERIMENTAL METHODS

This chapter covers the techniques used in the sample preparation, characterization, and modeling of materials investigated within this thesis.

3.1 Thermal Modeling

The thermal model used for this research was initially developed by collaborators Lee et al. at Oak Ridge National Laboratory [11, 126, 127]. The program is written in Python, which uses the open source finite element analysis framework FEniCS to solve heat equation partial differential equations (PDE's). This models a 3D mesh of a given material, which has energy input as a moving Gaussian source. The temperature at each node is calculated for each time-step, with the governing heat equation given in Equation 3.1 below:

$$\rho C_p \frac{\partial T}{\partial t} = \nabla(k \nabla T) + E + q \tag{3.1}$$

where ρ is the density of the material, C_p is the specific heat, T is temperature, t is time, k is thermal conductivity, and E is the energy input provided by the heat source. The thermal energy to melt powder particles on the start plate comes from the modeled electron beam, a

moving volumetric heat source with Gaussian distribution that was adopted to consider the material-heat source interaction. The mathematical expression for this heat source is given in Equation 3.2 below [113, 127]:

$$E(x,y,z) = A_e P \frac{2}{\pi r^2 d} e^{-2[\frac{x^2+y^2}{r^2}+(\frac{z}{d})^2]} \tag{3.2}$$

where A_e is effective absorption coefficient of electron beam, P is electron beam power, r is radius of the beam and d is the penetration depth, for which 20 µm is used. This was modeled by the utilized program as a 3-D transient simulation, constructed based on the numerical solution of heat transfer equation, with the electron beam used as the source of thermal energy. The electron beam controls the heat influx, while radiation and conduction control heat outflux. The geometry and meshes of a prismatic block were created using a built-in Python library in DOLFIN [127]. The dimensions of the material on which the beam was rastered were 10 mm (width) × 10 mm (length), and with the height chosen to accommodate each material's parameter sets. This volume is defined as an entirely homogeneous, dense plate with material properties as defined. As such there are no dynamics or powder particles being modeled, though the materials properties have been adjusted to more accurately reflect a the properties found in a powder bed. This computation space is spatially discretized into 400,000 tetrahedral cells, with adiabatic conditions assumed for the vertical surfaces, as in practical experimentation they are wholly surrounded by powder particles. The conductivity of the powder bed is only 0.3-1.5% of the bulk material and thus it is assumed that no heat flux passes through those surfaces [22]. Convectional heat loss is additionally assumed to be negligible due to vacuum operating condition of EBM. Heat loss by radiation is defined by Equation 3.3 given below:

$$q_{rad} = \varphi\varepsilon(T^4 - T_{vac}^4) \tag{3.3}$$

where q is heat flux by radiation loss, φ is Stefan-Boltzmann constant of 5.67 × 10-8 W/m2, ε is emissivity, and T_v is vacuum temperature.

This simplified thermal model does not account for phase changes but has proven useful for estimating PBF process temperatures despite its limitations. The model has been designed to decrease the run time for this model to minutes depending on conditions, whereas full multi-physics modeling of the AM process much more computationally expensive, taking days to weeks to simulate a basic layer melting [126, 128] .

$$q* = Aq/\left[r_B \lambda (T_m - T_0)\right] \tag{3.4}$$

$$v* = vr_B/\alpha \tag{3.5}$$

$$l* = 2 * l/r_B \tag{3.6}$$

Output can be used to simulate process related temperatures for parameter development and input for other models. This helps to give a baseline for the creation of a viable parameter space as the thermal model gives an estimate of the material's thermal history during the AM process. All developed parameter sets are given in dimensionless quantities, with power and velocity calculated using Equations 3.4 and 3.5, respectively where A is absorptivity, r_B is beam radius, λ is thermal conductivity, and α is thermal diffusivity. Energy density is thus dimensionless power over the multiplication of dimensionless velocity and dimensionless layer height, the latter defined by Equation 3.6.

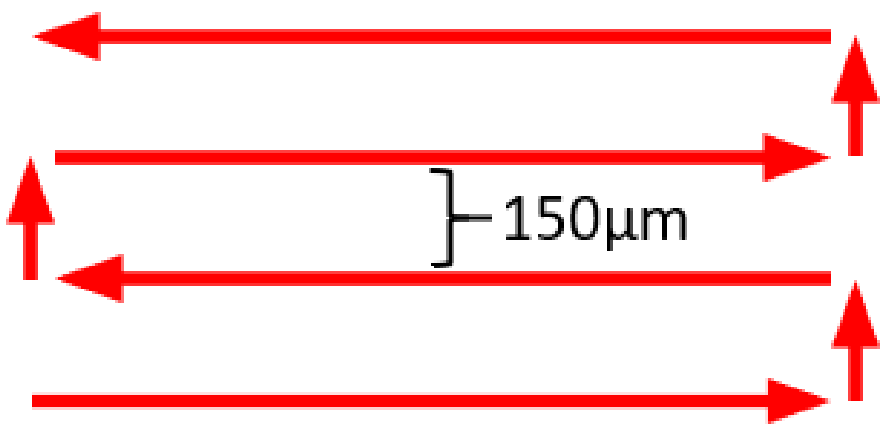

Figure 3.1 Example raster melting pattern in PBF

The initial WC-Co bead experiments used a single line raster as a first approximation of PBF conditions, whereas Figure 3.1 illustrates the scan strategy used to simulate to melting of single layers and full-scale parts in this experimentation. This scan strategy is commonly used in PBF processing, is easily implemented, and allows for more widely applicable results to AM as a whole. In this common raster scan method, the beam first moves horizontally in one direction atop the powder bed. It then moves down by the set hatch spacing, in this case 150 um, and begins the sweep again, however now moving from the right to left, with this process repeating for the full area of the melt geometry.

As in the original model implementation [11, 126, 127], material parameters were defined as drawn from the literature, with thermal and physical properties of the under-researched

Mo-TiC system calculated based on weight percent of incorporated powders [133–139]. Unlike the original work, however, the existence of a powder bed, as opposed to solid plate, was incorporated into material property calculations as defined in the literature [139–141]. Model results were scaled appropriately after comparison with the results from experimentation to better reflect the magnitude of the measured values.

Under these conditions, thermal models were conducted for each parameter set, with the results output as a combination of .xdmf and .h5 files, viewable with Paraview, a program co-developed by Kitware, Sandia National Labs, and CSimSoft. This programs allows for the display of generated thermal data, including temperatures at any given point, contour plots, and changes in temperature of arbitrary locations over time.

3.2 Thermodynamic Phase Modeling

The computational study of the phases was performed using the CALculation of PHAse Diagrams (CALPHAD) technique in order to predict phase formation and evolution in the WC-Co and Mo-TiC systems when melt and solidification conditions are far outside those found in standard processes. While AM is a nonequilibrium process, as the molten material undergoes rapid solidification followed by thermal cycles, performing phase equilibrium calculations at several temperatures, and spanning the entire gradient chemistry can still provide valuable information on the phases present during and after EBM.

ThermoCalc is a thermodynamic and diffusion simulation software package that allows for the generation of many diagrams from any arbitrary elemental composition. This program allows for the generation of many phase diagrams, including binary/ternary phase diagrams, Schiel plots, T-T-T diagrams, and equilibrium phase diagrams [130–132, 142]. The information generated from these diagrams is used in conjunction with that taken from existing literature to create a map of the entire process space. The modeled thermal history will then be used to estimate the regions in which the AM process takes place, and data from sample characterization (once available) is used to further limit the possible space in which the process must occur.

A general alloy thermodynamic database specifically covering Mo-TiC and WC-Co is not available because multi-component thermodynamic databases are often created for a particular alloy system such as the TCFE8 database for steels and TTI3 for titanium alloys from ThermoCalc. Due to this limitation of current multicomponent databases, the TICN9 sytem was used, which is a reasonable approximation due to the relative simplicity of these ternary systems [143].

3.3 Materials

The WC-11Co experimentation was performed on inserts acquired from Moldino Tooling Company, LTD Japan, with each insert being 5mm x 5mm x 30mm in dimensions, to allow for ample room for experimentation and provide homogeneous beam interaction conditions. The WC-Co powder used was WC-11wt%Co, also provided by Moldino Tool Company.

The custom Mo-TiC composition was manufactured from Mo powder acquired from Tekna with a nominal maximum size of 90 μm, which was combined with TiC powder with nominal particle size distribution of 3um to 7um obtained from SAT NANO (Guangdong, China). The Mo-TiC blended elemental feedstock was blended via planetary ball milling at a ratio of 40% Mo to 60% TiC. by weight, utilizing a 2:1 powder to ball ratio in a Retsch PM 100 ball mill with a 500-ml stainless steel jar and 10mm to 13mm-diameter stainless-steel balls, for up to 8 hours.

3.4 Characterization Techniques

Several characterization techniques were performed on all powders prior to experimentation to verify the desired properties and allow for conclusions to be drawn as to the effect of the EBM process on the feedstock powders. The particle size distribution of powder was determined using a Microtrac Turbotrac S3500 laser diffraction particle size analyzer which utilized a wet diffraction method. The evaluation of produced sample microstructures were performed on polished samples, which were prepared by setting in an epoxy mount, and subsequently ground and polished using 240 to 1000 grit paper. Samples were then polished using 9.0um, 3.0um, and 0.05um silica powder suspensions successively on a Mark IV 3B/4B polishing station. A Hirox KH 7700 advanced 3D digital optical microscope was used for preliminary images to aid in identification and measurement of WC-Co beads. A JEOL JSM-6010LA scanning electron microscope (SEM) was used for the assessment of powder morphology and sample microstructure imaging in backscatter composition mode (BEC). Additionally, the EDS capability of the JEOL JSM-6010LA was utilized for the compositional analysis of the produced powder and samples. An FEI Quanta 3D FEG SEM microscope was also used to achieve higher resolution SEM images and EDS mapping for select samples. A Rigaku SmartLab X-Ray Diffractometer was used to generate XRD spectra or phase identification, utilizing a Bragg-Brentano in reflection geometry and Cu K-alpha emission.

The image analysis process for phase identification by area was performed in ImageJ utilizing SEM images taken in BEC mode. The contrast differences between phase regions allowed for window/level profiles to be made for each phase, separating that phase from the rest of the image, and the area of the remaining regions, by black pixels, was recorded. The ratio

of this area to the total area of the selected region was then found. This process was repeated for each targeted phase, and then for each sample.

3.5 Sample Preparation

To observe solely the effect of the electron beam on solid WC-11Co, a single line was melted onto the face of each insert. To ensure consistency and repeatability, the inserts were mounted in a custom plate and affixed in the center of the Arcam Q10+ EB-PBF machine. These inserts were then divided in half and the revealed faces polished for the analysis of the produced beam line cross-sections. All bead experimentation was performed in a Q10+ with no automatic controls turned on, and with beam currents ranging from 4-25mA, beam speeds ranging from 50-2500mm/s, line offsets from 0.05-0.2um, and focus offset of 32mA.

To solely observe the effect of the electron beam on WC-Co and Mo-TiC powders, a single melted layer was formed on a bed consisting only of the manufactured powder. These powder compacts were formed, without binder, from each alloy via a hardened steel die pressed with a 20t manual hydraulic press. Each pressed puck measured 1.905cm in diameter, and between 5 and 6mm thick. Vertical dimension accuracy was variable but inconsequential, as the orientation of samples atop a powder bed allowed for height differences to be easily mitigated through controlled placement in that powder bed. The steel die used in compaction was of a split die design with two mobile punches on top and bottom, with the latter being made stationary by a arbor plate underneath the assemblage. The die was then split open to gently remove the compact, and the process was repeated for each powder composition.

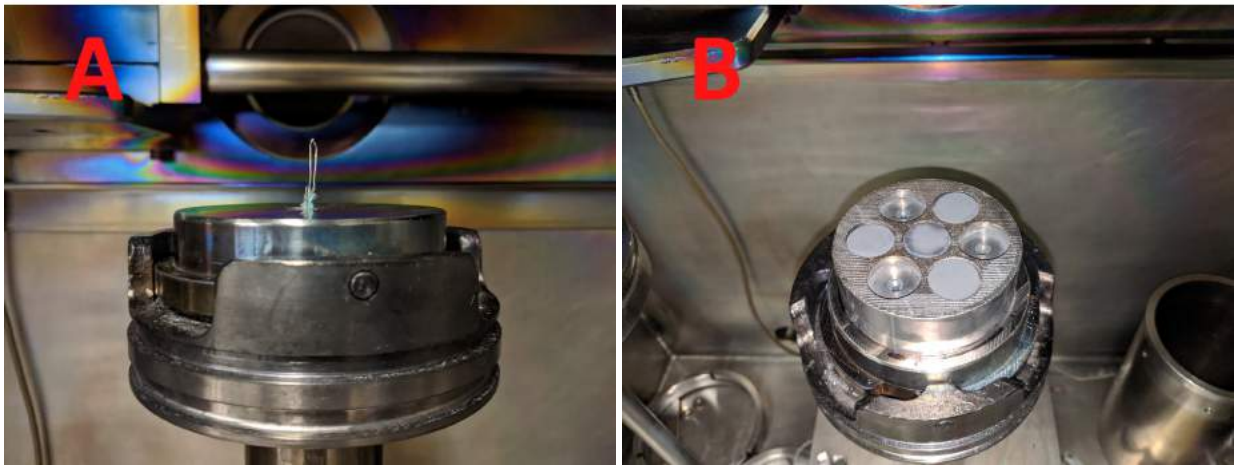

Figure 3.2 Placement of thermo couple wire (A) and typical sample configuration in the custom sample holder (B)

These pucks were then placed within a custom plate and affixed such that the Arcam S12 EB-PBF machine thermocouple was placed through the center hole resting just underneath the surface of the central puck, as shown in Figure 3.2. The samples placed in the center slot were prepared with a blind hole drilled into the underside to 1.2mm below the surface to accommodate the thermocouple wires and facilitate a more representative measurement of the temperature near the sample surface.

3.6 Electron Beam Melting

Single layer EB-PBF experimentation was carried out on a customized Arcam S12 electron beam melting system, while WC-Co bead testing and full-scale build performed an largely standard Arcam Q10+ EBM system. The single layer experimental setup is shown in Figure 3.2, which is comparable across EBM machines, and contains the thermocouple devices and plate used to house the individual samples. Due to the melting of single layer samples, experimentation was simplified over more traditional EB-PBF, while still encompassing the crucial process steps, the first of which is preheating to 900-1000°C. During preheating, a relatively high current (18mA, 60kV) defocused beam is scanned across the surface of the plate and the samples, with this rastering process designed in such a way as to maximize the input of heat energy while avoiding a charge buildup on the plate. An Endurance 2-color pyrometer was used to validate material surface temperature in conjunction with machine thermocouples.

This preheat step is typically utilized in EB-PBF to lightly sinter the powder bed, as is the case in the present experimentation. This sintering process results in the interconnection of powder particles within the compacted samples, which provides both a reduction in powder-scattering events, as well as a pathway to ground for electrons introduced by the electron beam. Next, the melting step is performed in which both beam current and speed are typically reduced as the beam scans across the sample surface. The samples are then left to cool to no more than 60°C before they are removed from the machine for analysis.

CHAPTER

4

RESULTS AND DISCUSSION

4.1 Introduction

This work is a modeling exercise with experimental validation that explores the effect of an EB heat source commonly used in 3D printing on the melting of materials which are traditionally solid state processed. Therefore, it is important to understand and predict the effect of the electron beam on the thermal conditions of the material, as well as the relationship between these variables and the observed phases in the respective material. A common first experiment in 3D printing development is to make single bead lines at different parameters to determine the influence of the heat source on material structure under varying conditions [144].

This work first models the expected thermodynamic and thermal responses of solid WC-Co to a single bead line EB heat source, at varied beam parameter settings. The next step in this thesis focuses on raster melting the top surface of WC-Co to model melt pool temperature, predicting possible phases and observe the effect of beam parameters on the material microstructure followed by multi-layer fabricated articles. A second custom produced alloy, Mo-TiC, is used to again test this raster methodology in a significantly different system, while still utilizing a material with high refractory content and significant proportion of second phases. This modeling methodology for melt pool temperature, pool depth, and phase prediction is a

first step in incorporating a fast and efficient predictive methodology for future 3D printing research at NCSU CAMAL.

4.2 WC-Co Results

Table 4.1 Parameters used during bead experimentation

Sample Number	Beam Power	Beam Velocity	Focus Offset	Energy Density
1	27.8	8	32	8531
2	34.7	8	32	10663
3	43.3	8	32	13308
4	51.9	8	32	15952
5	61.1	8	32	18767

Beam tracks melted on WC-11Co solid rectangular insert bars were used as starting point for the methodology. Since the tracks were single melt lines, it was a logical first simple condition to test the methodology [144]. The thermodynamic modeling, thermal modeling, and experimental results were all combined to investigate and make predictions for the response of the WC-11Co system to electron beam parameters comparable to those used in full-scale AM. Experimentation on the WC-Co alloy was initially limited in scope to single line bead scans on pre-made WC-Co inserts, with the purpose of this experimental set-up to limit as many variables as possible, in an attempt to observe solely the effect of the EB source on material microstructure.

The basic parameters used in the bead testing are shown in Table 4.1 where the beam power (dimensionless), beam speed (dimensionless), beam size (Focus Offset FO, mA), energy density (dimensionless), and a constant 60kV beam voltage were used, with only the beam power modified from 27.8 to 61.1, respectively. The modeling results are useful as a guide to the effect of the parameter space on microstructural features of WC-Co, as opposed to ideal PBF manufacturing parameters.

4.2.1 WC-Co Thermodynamic Phase Modeling

Due to the well-studied nature of the WC-Co alloys, especially as compared to Mo-TiC,

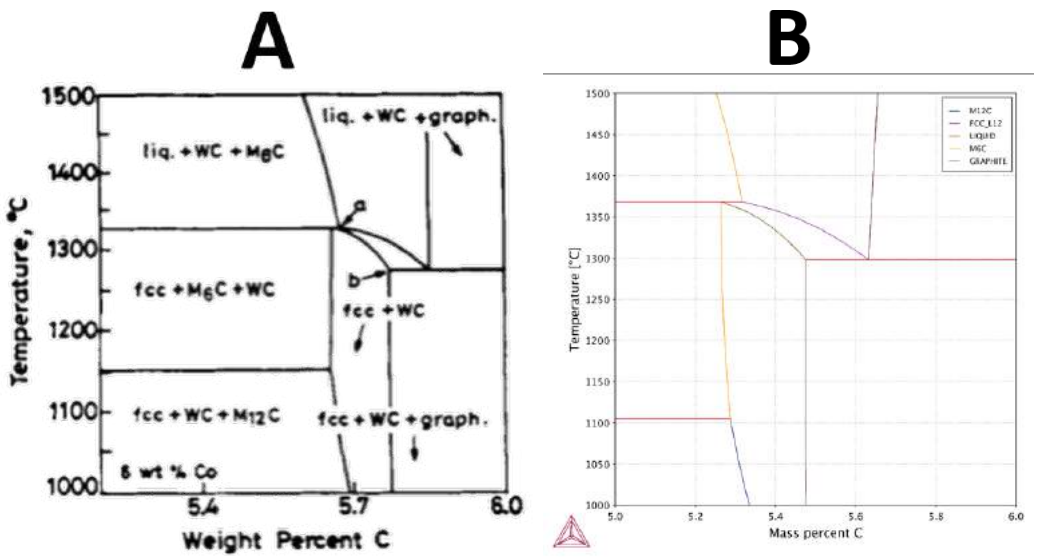

Figure 4.1 Binary phase diagram (A) for WC-Co, courtesy of Springer-Verlag, Metallurgical Transactions. Generated binary phase diagram (B) for WC-Co, generated by ThermoCalc. [72]

thermodynamic modeling was done as a confirmation of the methodology's ability to produce results compatible with those found in the literature, as well as extend beyond the range of commonly reported temperatures and compositions. This was useful in this system due to the non-traditional processing space explored in this research, where the experienced material conditions are expected to deviate greatly from traditional processing routes. Figure 4.1A shows a phase diagram commonly used for the WC-11Co system [72], whereas Figure 4.1B shows the same diagram as generated by ThermoCalc using the TICN-9 database with data verified for carbide calculations [143]. A cursory comparison of the two diagrams shown in Figure 4.1 reveals very little difference between the presented literature data and calculated phase diagram; thus the major advantage of generating phase diagrams via ThermoCalc is the easily customizable range of both temperature and composition.

At low carbon contents, the M6C phase is present above 1150°C, though as carbon content increases past 5.6 mass%, this phase is not present at equilibrium, as is also reported in the literature. Below 1150°C, this M6C phase is not found alongside the Co FCC and the WC phase, however a similar phase, M12C is found instead, and is also not observed above 5.7 mass% C, which is again well-supported in the literature. At temperatures below 1300°C and carbon concentrations above 5.75 mass%, graphite is predicted to form at equilibrium, a trend that is also found in studies on this system [145]. The dotted line in Figures 4.1A & B indicates the approximate carbon composition of the WC-Co bars, and is a stoichiometry commonly found in commercially available WC-11Co solids and powder.

4.2.2 WC-Co Thermal Modeling

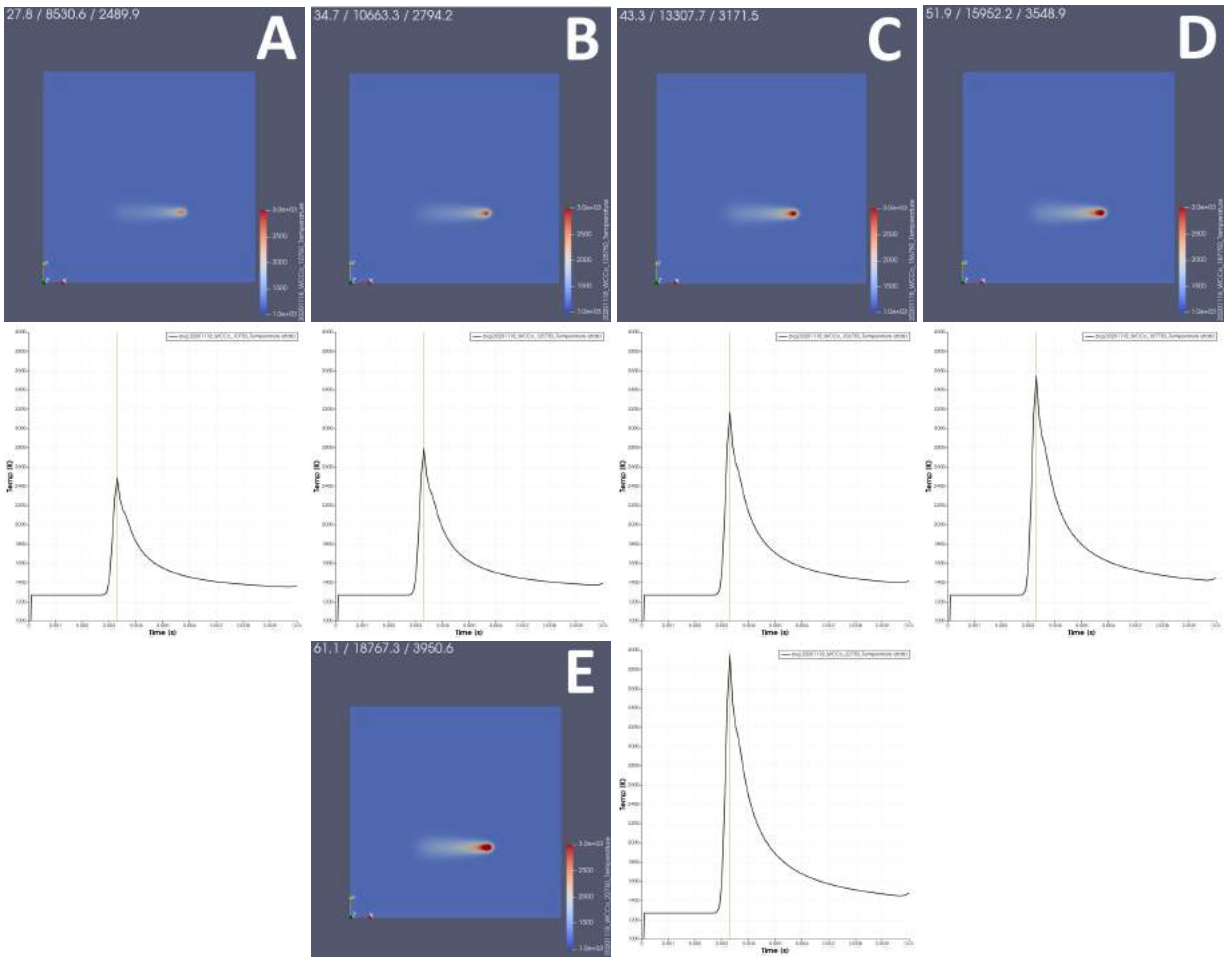

Figure 4.2 Thermal model results for WC-Co bead tests, including thermal profile for each sample parameter set, showing the average temperature of an area on the simulated surface as it changes with time

The results of the thermal model for the given parameters are shown in Figure 4.2A-E. Figure 4.2 includes a top view of a snapshot of the melt pool visualization, with temperature scale bar shown for each beam condition, and with the beam power, energy density, and maximum average temperature are also listed at the top of each snapshot.This maximum average temperature was found by taking the average temperature of 9 mesh points, forming a square 75um a side on the material surface, equivalent to an area of 0.00563mm2. A thermal profile is associated with each melt condition and provides an estimation of the melt track thermal profile for a given condition and maximum temperature experienced by the material.

Fig 4.2A shows that the 8530 energy density condition produces a maximum temperature rise from 1273K base preheat temperature to 2490K (2217 C), approximately 900 C higher than the equilibrium melt temperature of Co for the system composition. As the beam current increases, Figures 4.2B-E illustrate that the bead melt pool temperature continues to rise until a maximum value is reached at nearly 4000K in Figure 4.2E at an energy density of 18767; a temperature nearly twice the melting point of Co for the system. This condition is the result of an extreme parameter set design to explore the limits of the methodology.

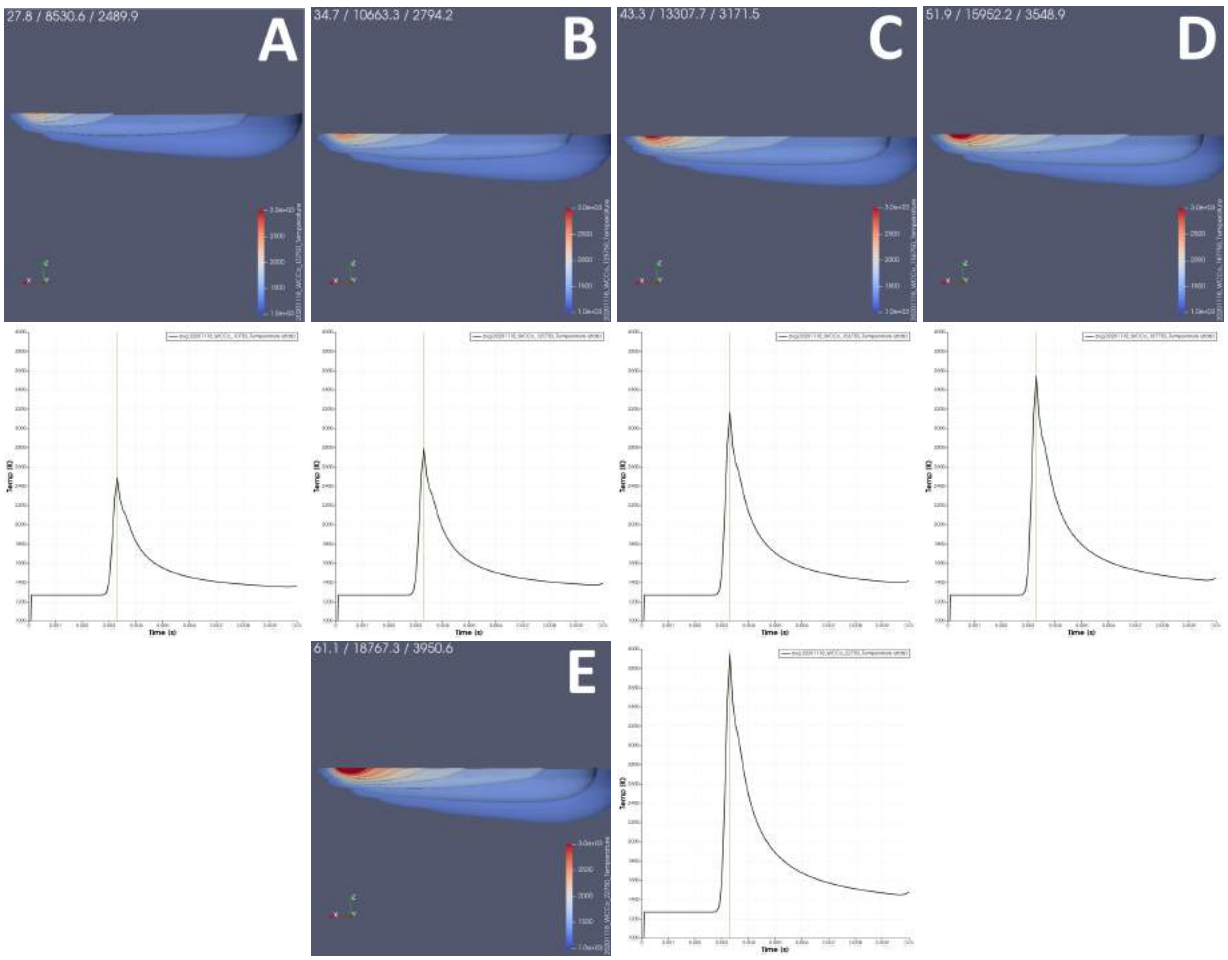

Figure 4.3 Thermal model results for WC-Co bead tests, including contour profiles and time-temperature plots for each sample parameter set

Figure 4.3 represents the thermal model by evaluating a cross-sectional view of the beam area to gain insight concerning temperature penetration in the Z-direction within the single melt track. These contour plots show the boundaries between temperature regions in 500°C increments, which are used evaluate the effect of different beam parameters on the material.

Furthermore, these contour plots are utilized to estimate the melt pool depth through an estimation of the temperature at which the material would exhibit observable changes to its internal structure. The associated temperature-time plots are duplicates from Figure 4.2, as a reference for the thermal profile of the hottest point in contour plots in Figure 4.3.

Differences between the model conditions and the real-world melting conditions are important to consider, most notably the dynamic/non-dynamic gap, and will as such require an estimation of melt pool depth and temperature. Additionally, the contour lines during a still frame from the model show regions of the material that attained that temperature, even instantaneously, and thus may not exhibit changes in microstructure even when the modeled temperature is greater than a given phase's melting temperature. In this case, 1350°C and 2000°C were chosen as likely contour lines for forming an upper and lower bounds, respectively, on the as-measured boundary between melted/unmelted material. 1350°C was chosen due to its proximity to the melting temperature of the eutectic composition, as calculated by the generated phase diagram shown in Figure 4.3. The measured melt pool depths would likely be lower, due to a number of factors previously outlined, not least the very short time spans in which the material may be above 1350°C. 2000°C was chosen as a secondary line due to this temperature being well above even the solidification temperatures of all predicted phases of WC-Co, excepting WC itself, and the effect of even short exposures to these temperatures should be visible in the resultant microstructures. These two values allow for a range of possible profiles, necessary due to the highly non-equilibrium conditions associated with 3D printing.

Figure 4.4 illustrates the measurement of the contour lines as calculated by the thermal model, with the overall depth of the simulated material at 1mm, which was sufficient for most experimentation parameters. At the lowest energy density value of 8530 the contour line for a temperature of 2000°C reaches only 31.1um into the solid surface, as shown in Figure 4.4, with the temperature quickly dropping below 1350°C, the eutectic melting temperature, after 122um from the surface. Again, as the energy density increases, the bead temperature is significantly impacted. Sample 3, with an energy density value of 13307 and a 2000°C contour line depth of 79um, was calculated to have a maximum average temperature approaching 3000°C with the system likely is fully melted near the surface. The model estimates that the melt pool becomes further exaggerated with 2000°C contour depths in excess of 160um as the energy density exceeds 15952, resulting in a processing space which is far from equilibrium for traditionally produced WC-11Co [75].

With these caveats in mind, these boundaries for melt pool depth for each bead parameter set is shown in Table 4.2, and are graphed together in Figure 4.5. Figure 4.5A shows the overall trend of pool depth increasing with beam energy density, but with predicted depth increasing by a smaller amount with each successive increase in energy density, with a very similar trend

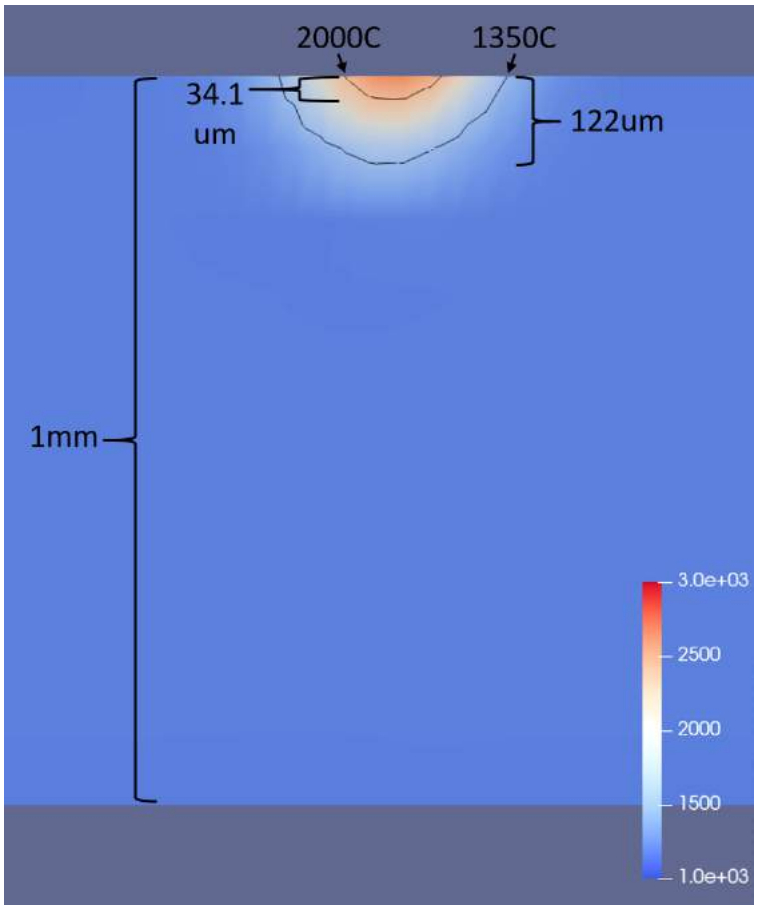

Figure 4.4 Thermal model results for 8530 energy density sample, with thermal contour lines and measured depths labelled.

Table 4.2 Thermal model results for WC-Co bead tests, including calculated depths at 1350°C and 2000°C boundaries.

Sample Number	Beam Power	Beam Velocity	Focus Offset (mA)	Energy Density	Max Temp (C)	Mod. Depth: 1350C (µm)	Mod. Depth: 2000C (µm)
1	27.8	8	32	8531	2216	122.0	34.4
2	34.7	8	32	10663	2521	138.1	57.7
3	43.3	8	32	13308	2898	154.6	79.0
4	51.9	8	32	15952	3275	160.4	90.4
5	61.1	8	32	18767	3677	165.2	98.8

shown when plotting calculated melt pool depth against simulated maximum temperature in Figure 4.5B. Though this overall trend is trivially found, and has been shown in numerous AM studies [116], the specific results are important in refining the model for predictive purposes, as it allows for the accurate estimation of melt pool depth after even limited experimentation. Since traditional HIP or LPS processing does not produce fully liquid WC-Co systems, the

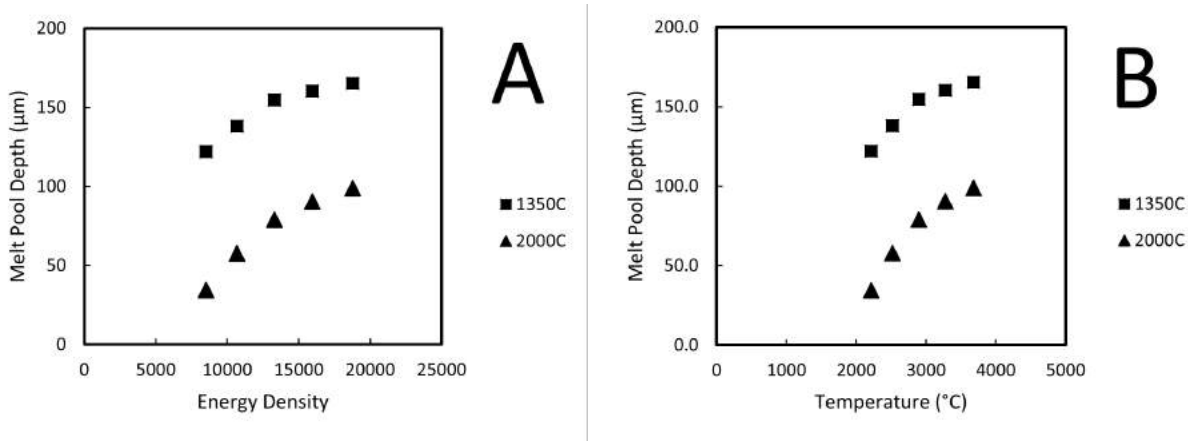

Figure 4.5 Thermal model results for WC-Co bead tests showing the modeled depths for each parameter set at 1350°C and 2000°C boundaries, relative to both energy density (A) and modeled maximum material temperature (B).

thermodynamics were evaluated in an attempt to understand the effect this may have on phase formation and microstructure.

Table 4.3 Thermal model results for WC-Co single layer tests, including calculated depths at 1350°C and 2000°C boundaries.

Sample Number	Beam Power	Beam Velocity	Focus Offset (mA)	Energy Density	Max Temp (C)	Mod. Depth: 1350C (µm)	Mod. Depth: 2000C (µm)
1	27.8	8	25	8531	2582	386.4	62.3
2	34.7	8	25	10663	3010	531.7	123.1
3	43.3	8	25	13308	3585	617.0	206.2
4	51.9	8	25	15952	4113	714.6	254.5
5	61.1	8	25	18767	4635	786.5	283.0

Though the parameter sets remained the same, additional melt conditions such as beam interaction with a sufficiently deep powder bed, no solid substrate, and multi-melt line interactions meant the model data used to predict bead test would be insufficient to accurately predict the single layer experimentation. Thus a similar methodology was utilized to calculate the expected depths of the single layer raster experimentation, with the results shown in Table 4.3. As expected, these results follow a similar trend as observed in the bead test model results, with estimated melt pool depth increasing as energy density increases, while decreasing when changing the boundary from 1350°C to 2000°C.

These modeled melt pool results were also graphed together in Figure 4.6, where Figure 4.6A

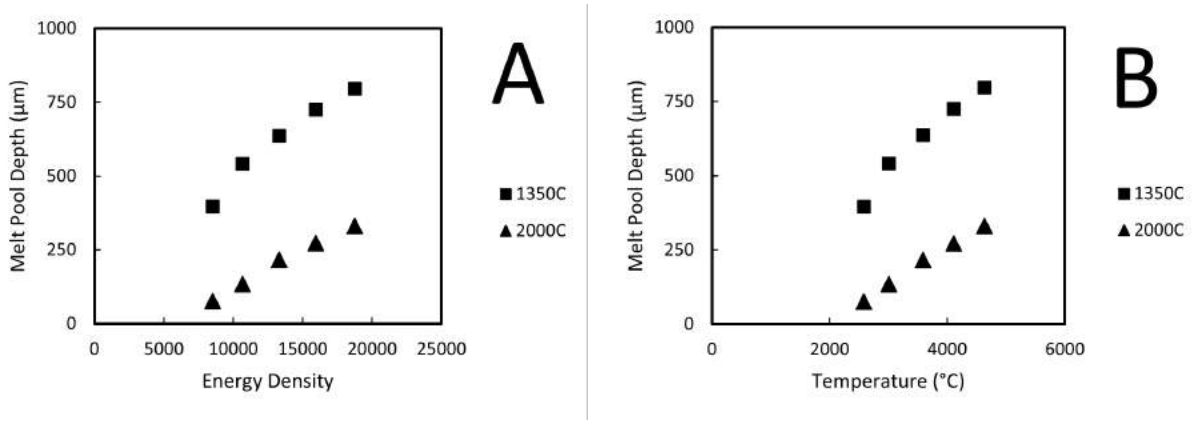

Figure 4.6 Thermal model results for WC-Co single layer tests showing the calculated depths for each parameter set at 1350°C and 2000°C boundaries, relative to both energy density (A) and modeled maximum material temperature (B).

again shows the overall predicted melt pool depth increasing with increasing energy density, however with each subsequent increase in energy density the magnitude of the additional depth decreases. A similar trend is shown in Figure 4.6B, where simulated melt pool temperature is plotted against modeled melt pool depth. From this data, as in the bead tests, the depth of the samples to be manufactured will likely be between the values predicted by the 1350°C and 2000°C melt pool lines

4.2.3 WC-Co Combination of Models

Figures 4.7A-D are ternary isotherms which represent the equilibrium composition of WC-11Co, in weight percent, and where the utilized WC-11Co composition is identified on each respective figure. For traditionally processed WC-Co, one of the more critical areas of the phase diagram is the ability to produce liquid Co + solid WC, then solidifying in the FCC (Co) + WC portion designated by the blue point near 5.7 wt%C in Figure 4.7C. If the system remains in this composition and temperature range during HIP or LPS processing, the phases produced will be only solidified FCC-Co evenly distributed in the matrix surrounding WC particles or grains. Normally, the most detailed phase diagrams, such as the one traditionally used shown in Figure 4.1A, go up to approximately 2000°C, and represent the normal processing space for this material composition. If the composition or processing space goes outside these boundary conditions, deleterious phases such as HCP W12C (eta phase) may form which can significantly affect mechanical properties and toughness [145, 146]. Certainly, the systems are not traditionally intended to go fully liquid as suggested by the thermal model.

The result of the thermal modeling is that high temperatures are likely required for the

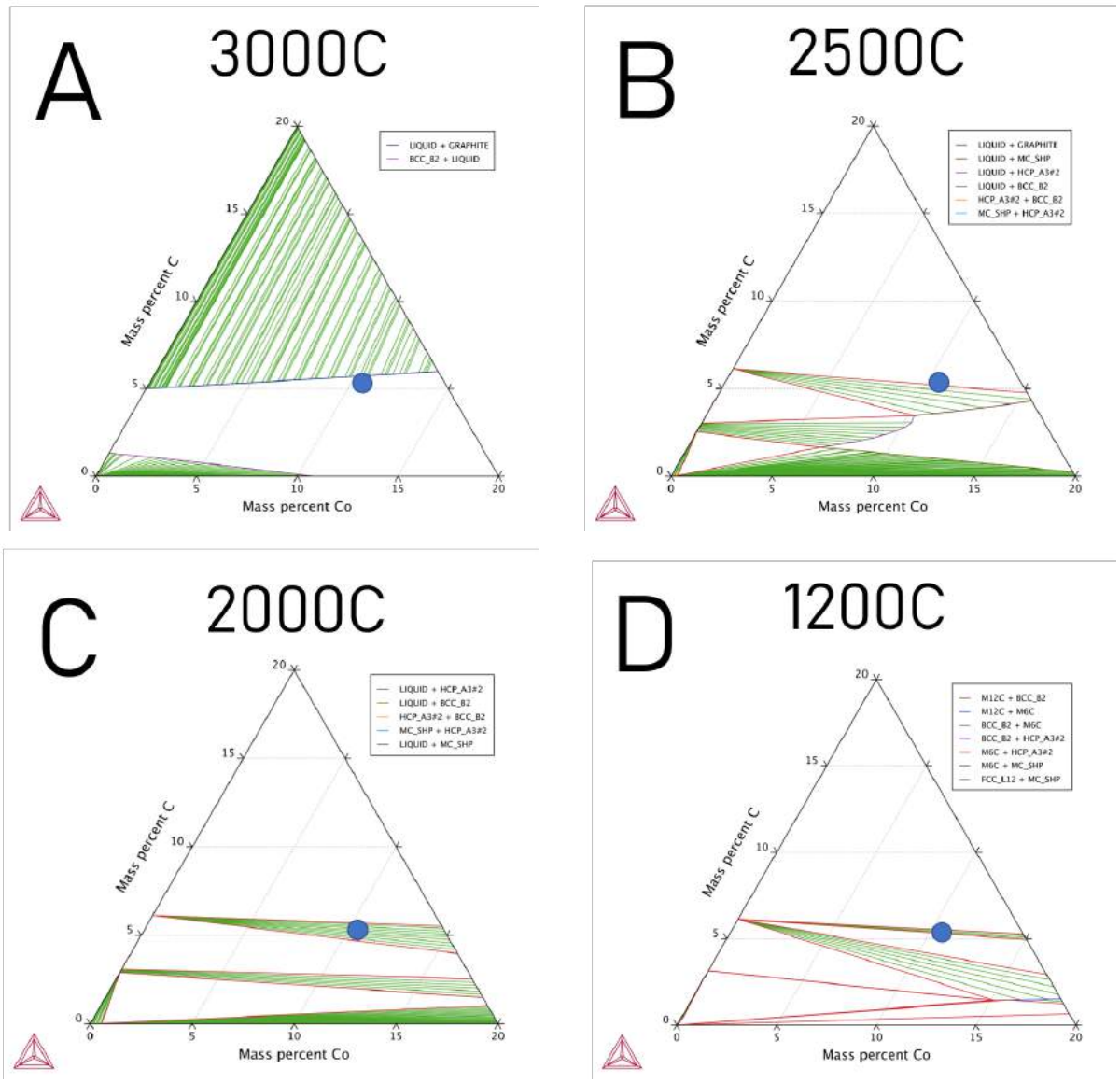

Figure 4.7 Calculated ternary phase diagrams with associated temperatures and experimental WC-11Co composition indicated in each figure.

melting of layers of significant depth, which is required for multi-layer AM. However, at such extreme temperatures, change in composition is possible, and the thermodynamic phase modeling suggests that even small changes in composition, locally or globally, could have significant changes to the microstructures produced by EBM.

4.2.4 WC-Co Bead Experimentation

Solid rectangular bars of commercially manufactured WC-11Co tooling inserts were heated

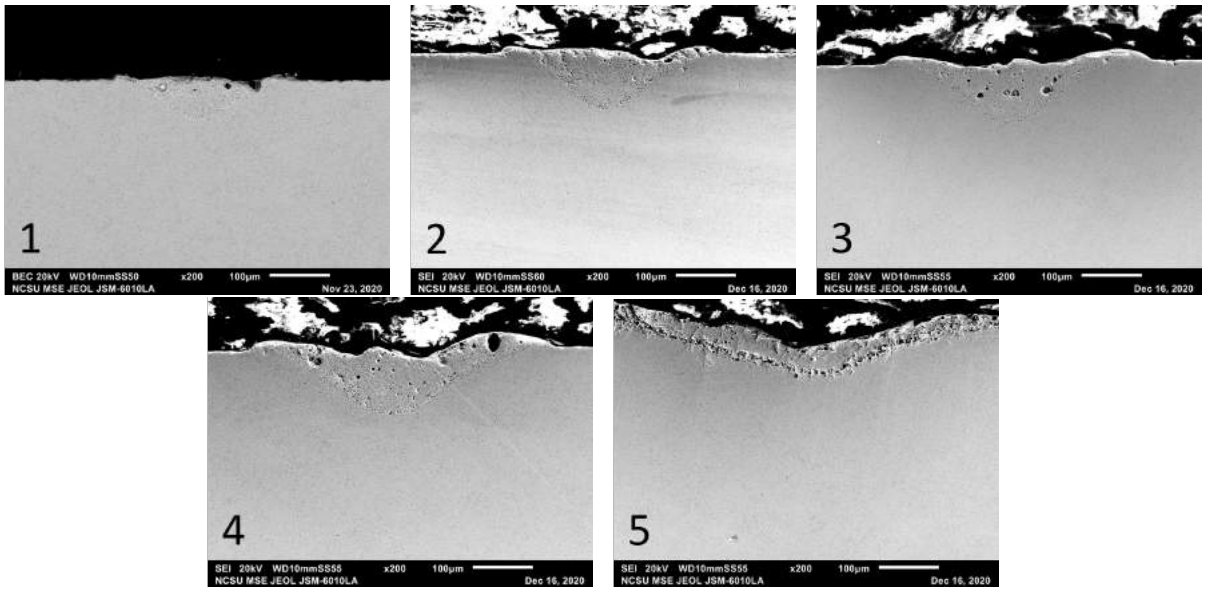

Figure 4.8 SEM images of polished cross-sections for each WC-Co bead parameter set 1-5, taken at 200x magnification

Table 4.4 Thermal model results for WC-Co bead tests, including calculated depths at 1350°C and 2000°C boundaries and measured melt pool depths.

Sample Number	Beam Power	Beam Velocity	Focus Offset (mA)	Energy Density	Max Temp (C)	Mod. Depth: 1350C (µm)	Mod. Depth: 2000C (µm)	Measured Depth (µm)
1	27.8	8	32	8531	2216	122.0	34.4	65.8
2	34.7	8	32	10663	2521	138.1	57.7	92.4
3	43.3	8	32	13308	2898	154.6	79.0	106.3
4	51.9	8	32	15952	3275	160.4	90.4	112.7
5	61.1	8	32	18767	3677	165.2	98.8	116.5

to above 900°C in an Arcam Q10+ EB PBF 3D printing machine and single melt tracks were performed at the parameter settings shown in Table 4.4. Figure 4.8 shows a cross section of the bead results. The melt pools were measured by optical microscopy and SEM as determined by the interruption of the initial manufactured microstructure by the beam, with these results also shown in Table 4.4. As expected, the general melted bead microstructures show significant changes from the initial microstructures present in the stock WC-11Co bars prior to melting. The pools in Figure 4.8 also show an increase in depth with higher beam currents, which is also expected based on thermal modeling results.

Closer inspection of the bead cross-sections reveals the microstructural changes undergone by the alloy during melting and solidification. Figure 4.9A shows the traditionally processed microstructure. This typically contains prismatic shaped WC grains nearing 0.5-5 um in size surrounded by a matrix of Co. The beaded samples exhibit a markedly different microstruc-

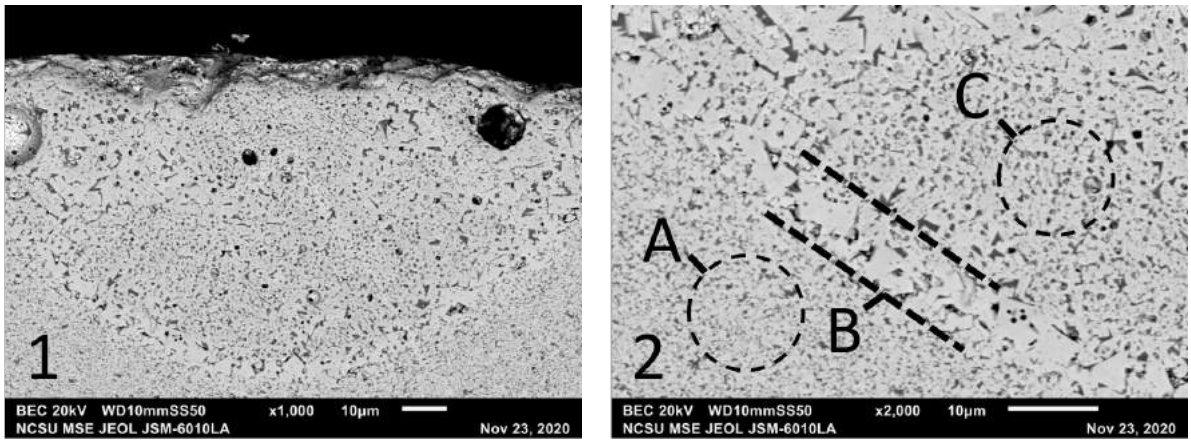

Figure 4.9 SEM images of polished cross-sections for Sample 2, a representative WC-Co bead parameter set, taken at (1) 1000x and (2) 2000x magnification, with added annotations labelling (A) unaffected WC-Co substrate, (B) transitional region with large WC grains, and (C) melted WC-Co region with round porosities and few large WC grains.

ture with three significant characteristics shown in Figure 4.9B: A) Clear and sharp boundary between the manufactured bar and the bead pool, B) a thin region of larger WC grains at the bead & rectangle interface, and C) a region within the bead with fewer large WC grains with many small, spherical pores, not observed in the initial bar material.

The internal microstructures inside the ring of large WC grains share similarities between beads. Notable features include porosity of varying sizes, but are generally spherical in their morphology. These pores are likely the result of Co and C evaporation within the melt pool, as have been observed and conjectured by contemporary research [94], with this paper reporting similar structures by melting WC-25Co single tracks in a laser PBF system. Attempting to obtain densities nearing 95% theoretical, a separate paper reported significant changes in the microstructure was found including round pores similar to those in Fig. 4.9A [96], with both Ulmann and Ibe attributing these pores to the release of C and Co during the melting process. Ibe et al. reported the existence of eta and W2C phases, which were conjectured to be largely a result of local changes in composition, specifically a decrease in C content. This generally agrees with the results presented in Figure 4.9, as EDS mapping of the WC-Co beads clearly shows significant amounts of W in the Co-rich regions, the likely result of eta phase formation, which is also seen from Ibe et al. Thermodynamic modeling in their report revealed phase formations of Co at 1350°C, WC at 1880°C, and W2C and eta phases at 1920°C by examining Schiel and equilibrium phase diagrams similar to those in Figures 4.9A & B. While it is difficult to compare laser PBF energies to EB PBF energy inputs, it does show that significant energy inputs can significantly disrupt traditionally observed microstructures.

Figure 4.10 compares a representative melt pool and the modeled thermal contour lines

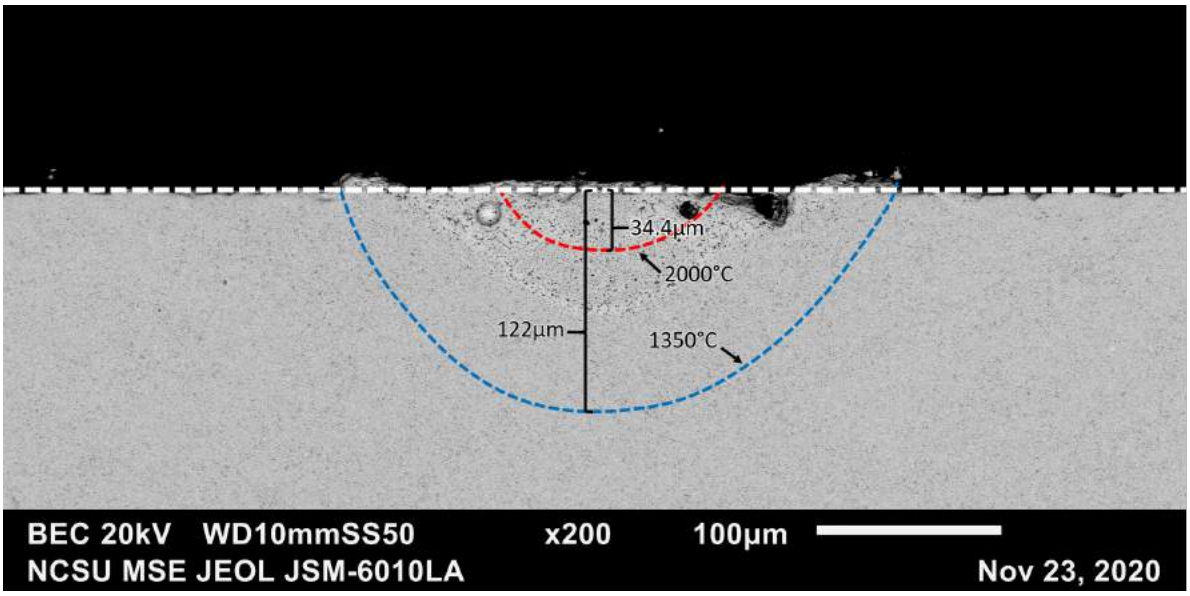

Figure 4.10 Example thermal result for the middling, 13307 energy density sample, showing modeled 1350°C and 2000°C contour boundaries overlain on a SEM micrograph.

at 1350°C and 2000°C for the middling 13307 energy density sample, showing the differences between the depths and overall conformations. There is less symmetry present in the melted beads as compared to the modeled melt pool, likely due to the lack of dynamic information in the model. This gap in dynamic information is most apparent when examining the differences between the starting bar surface (dashed white line) and the final bead formed. Here, significant amounts of material has been pushed out of the melt pool and are now atop the bar surface, leading to a wider bead than the expected beam diameter would imply; however, the bead morphology below the surface largely follows a parabolic curve similar to that as predicted by the thermal model, as shown in Figure 4.10.

As there is an easily observable change in structure associated with the melt pool, with the melt pool depth trivially estimated from SEM images by measuring the deepest point with observable changes from the initial surface of the stock WC-Co bar. The measured values are presented in Figure 4.11, and plotted against energy density (A) and modeled temperature (B), and with the depths of the modeled contour lines shown again for comparison. The measured values closely follow the trend of the simulated values, tending to fall between the upper and lower bounds as predicted previously, with a small and relatively consistent variation. As expected, the 1350°C boundary was an overestimation of the melt pool depth, with the measured values falling closer to the predicted melt pool depths of the 2000°C boundary. Indeed, by taking the average difference between measured and simulated depth per degree C, the temperature boundary that best predicts the real melt pool depths is 1775°C, accurately

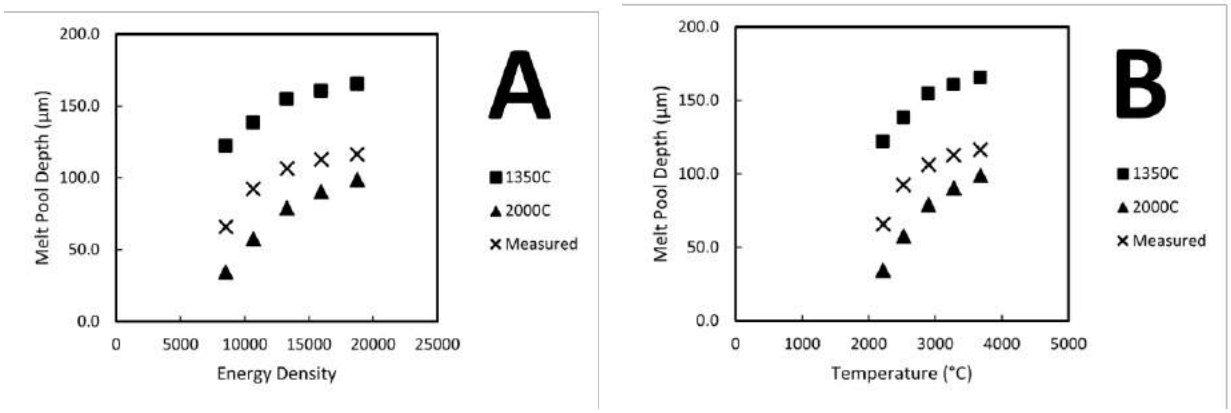

Figure 4.11 Thermal model results for WC-Co bead tests showing the measured and calculated depths for each parameter set at 1350°C and 2000°C boundaries, relative to both energy density (A) and calculated maximum material temperature (B).

predicting melt pool depth with less than 5% deviation in all but one sample; that of the highest energy density parameter set. In each modeling condition, the melt pool depth of this highest energy density parameter set was overestimated, likely a result of the exaggeration of imperfect model assumptions at the extremes of the parameter space.

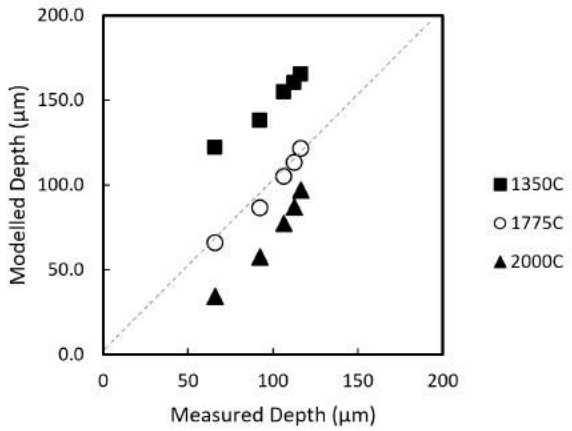

Figure 4.12 Thermal model results for WC-Co bead tests showing the modeled depths for each parameter set at 1350°C, 2000°C boundaries, and the projected contour line of 1775°C plotted against to the measured depths for each parameter set. An 'ideal' 1:1 correlation is represented by the dashed grey line.

Of interest to AM as a whole, and this research, is found when comparing these observed microstructures to those microstructures found in the bulk material of AM fabricated WC-

Co. Research has been reported on laser systems [47, 147], EB systems [95] and binder jet 3D printing [47, 148]. While the extreme microstructural changes observed in Figure 4.12 are not often reported during the melting of powder; serious issues such as cracking, significant WC grain growth, Co evaporation and deliterius phase formation are often reported, indicating the difficult in printing materials sensitive to melting and traditionally produced by solid state processing or LPS.

4.2.5 WC-Co Single-Layer Experimentation

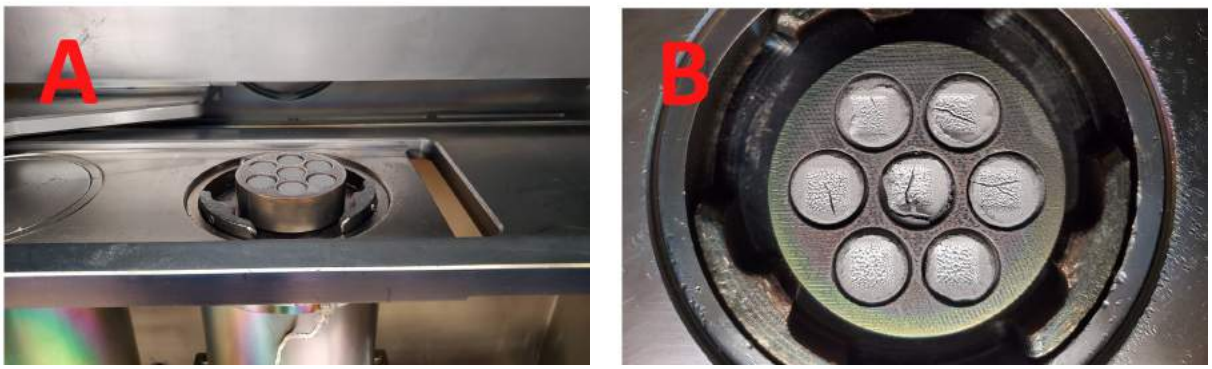

Figure 4.13 Custom socketed plate featuring A) pucks after pressing and B) pucks after melting.

The single bead experiments with WC-Co show how dramatically the material can change due solely to interaction with an electron beam, and thus the importance of being able to understand and predict this behavior, especially in materials that are not traditionally processed via melting prior to 3D printing. However, the melting of powder layers is crucial to the broader application of this methodology and a useful step between bead experimentation and full-scale AM, and so the parameters derived from bead testing were again examined in single layer experimentation.

For the WC-Co single layer experimentation, the electron beam was used to heat a custom socketed plate to approximately 1000°C as measured by machine thermocouple and two-color pyrometer. In these sockets were pressed WC-11Co powder pucks, configured as shown in Figure 4.13A. These pucks were then melted via the electron beam in square rasters, resulting in a single melted layer on the top surface, shown in Figure 4.13B, with similar parameters as in the bead experimentation, shown in Table 4.4. These samples were melted in an Arcam S12, unlike the bead experimentation, however the Arcam S12 and Arcam Q10+ are very similar in their operation, and differences between machines were accounted for. These changes

Table 4.5 Beam parameters utilized during single layer raster experimentation.

Sample Number	Beam Power	Beam Velocity	Focus Offset	Energy Density
1	27.8	8	25	8531
2	34.7	8	25	10663
3	43.3	8	25	13308
4	51.9	8	25	15952
5	61.1	8	25	18767

most notably included ensuring the beam size was comparable between the two machines, which involved adjusting the focus offset appropriately. Figure 4.13B shows the tops surfaces of several samples cracked after melting, likely resulting from rapid cooling after melting,a commonly reported phenomenon when investigating the AM MMC's like WC-Co, though more commonly found in laser-based AM [95, 96].

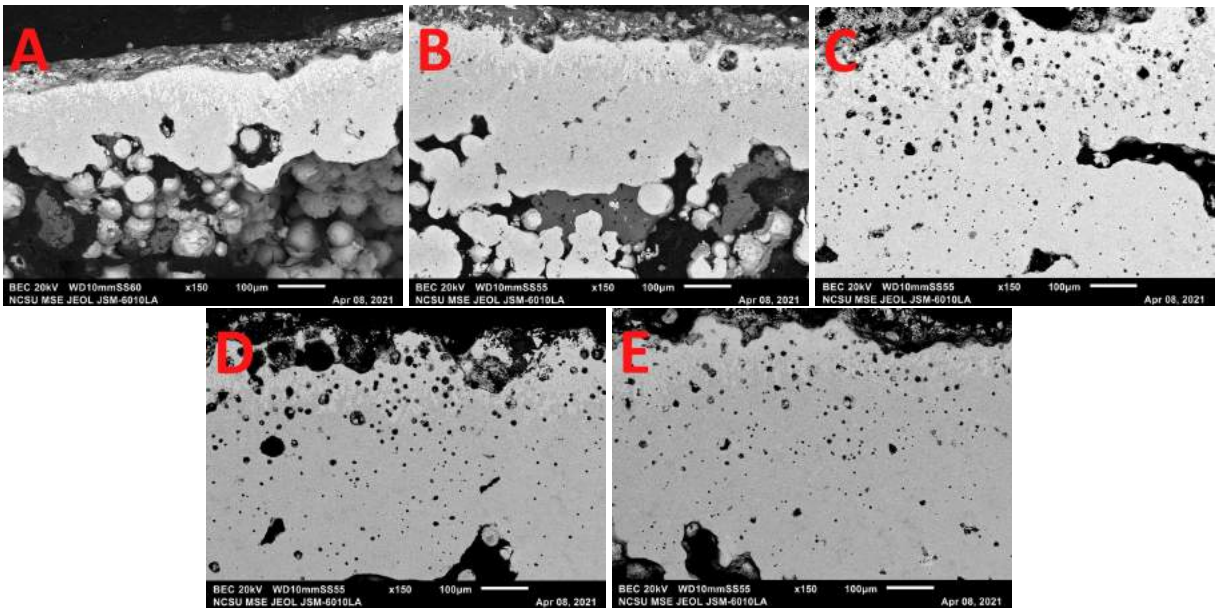

Figure 4.14 Representative, 150x magnification SEM images of cross-sections for single layer WC-Co Samples 1-5. Images were taken in backscatter detection mode.

The resulting samples were then sectioned and polished for the examination of microstructures, with BEC SEM images of the sample cross-sections shown in Figure 4.14A-E at 150x

magnification for Samples 1 to 5, respectively. The produced samples were generally cohesive, single layers between 100 and 800um in depth, with significant variation within and between samples. As expected, as beam energy density increased, the average depths of the single layers tended to increase from Samples 1 to 5.

Porosity was also observed in all samples, though the morphology and distribution also varied between samples, with more spherical porosities observed at the higher energy densities of parameters sets 3-5, which correspond to Figures 4.14C-E, respectively. These spherical porosities, where present, are also observed to increase in size closer to the top surface of the melted later, though they will not be the focus of the present investigation. Other microstructural features were also observed to be affected by proximity to the top of the melt pool, such as a lighter gray region shown in greater detail in Figure 4.15.

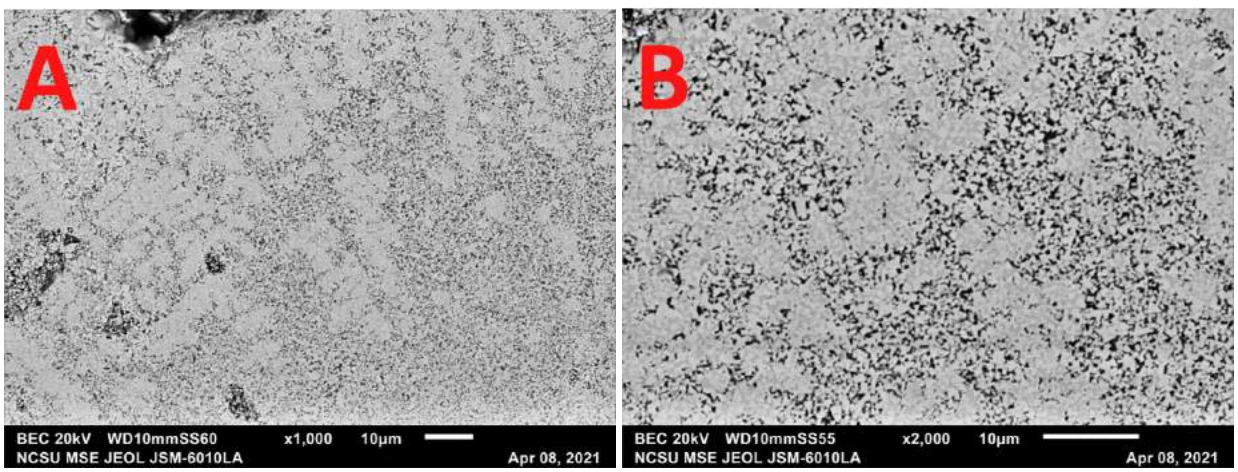

Figure 4.15 Representative A) 1000x magnification and B) 2000x magnification SEM images of cross-sections for WC-Co Sample 1. Images were taken in backscatter detection mode.

Figure 4.15A shows these lighter gray structures to be dendritic-like in conformation, extending from the top surface down largely vertically into the melt pool. These structures remain consistent in size and shape between samples even with large differences in predicted melt temperature and beam energy densities, indicating their formation is more dependent on solidification conditions as opposed to melting conditions, which largely follow similar gradients between samples. Additionally, Figure 4.15B shows these structures to differ in terms of the Co binder phase rather than the WC phase, as WC grain size and morphology remain the same within and without these regions. This is further supported by EDS results shown in Figure 4.16 below.

Figure 4.16 shows the EDS map data gathered from a representative section of Sample 1,

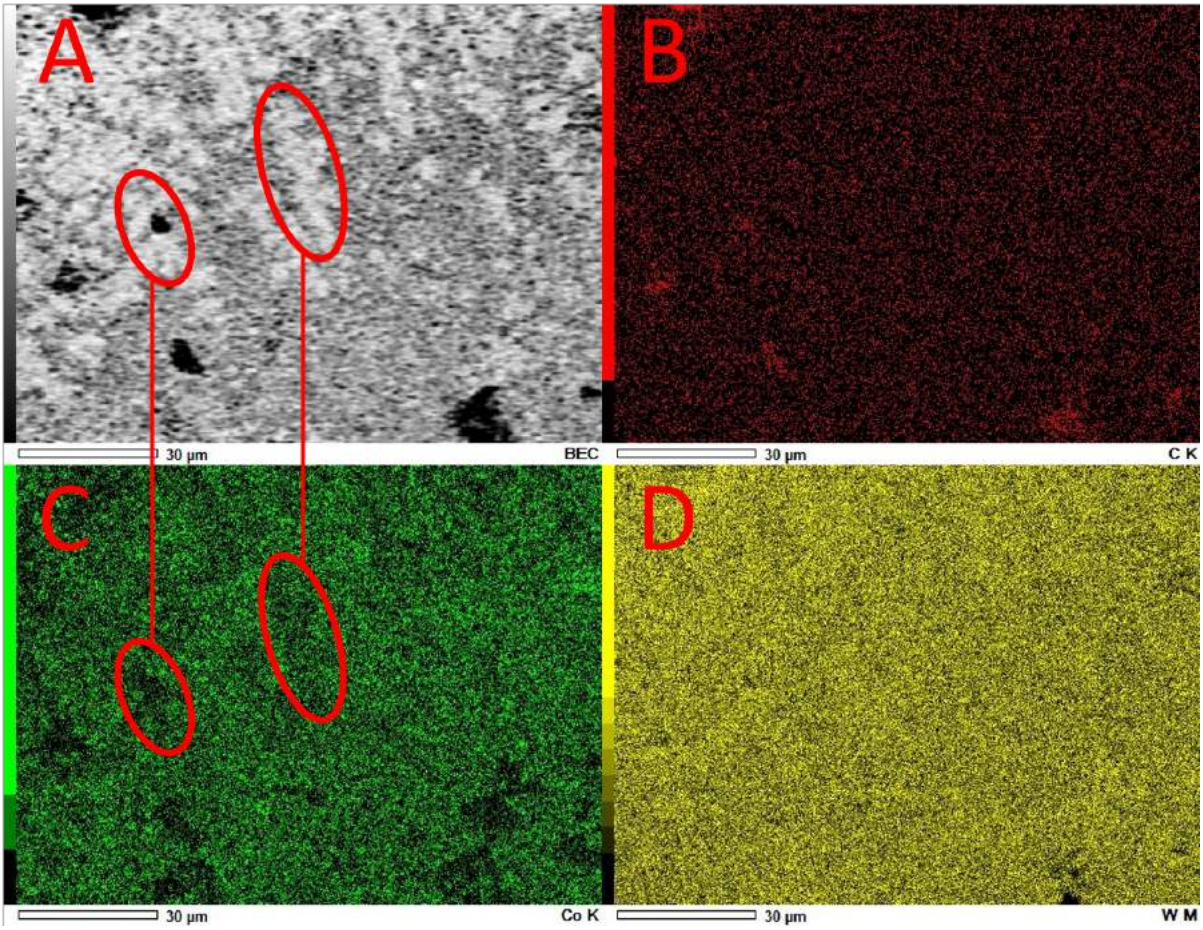

Figure 4.16 Representative SEM and EDS map data from 1000x magnification cross-sections for WC-Co Sample 1. Images were taken in backscatter detection mode.

where A) is the standard BEC image, B) is the detected Carbon content, C) is the detected Co content, and D) is the detected W content. Based on this data, the C and W contents remain relatively consistent across the sample, changing very little as the microstructures change. However, as indicated by the red annotations, regions with the light gray, dendritic structures are associated with a moderate decrease in relative Co content. This supports the conclusion that these lighter gray regions are the result of WC dissolving into the Co matrix, which would lead to the formation of eta phase and the relative increase in regional image brightness that is characteristic of of heavier elements with backscatter electron detection used to image the samples.

Additionally, the EDS data shown in Figure 4.16 shows that other possible phases, such as graphite, are likely not present given the relatively even and low detected C through this and other samples. As it is unlikely the either C or Co increased in composition locally, the final

composition is more prone to the formation of eta phase, as predicted by the thermodynamic phase modeling. Overall the internal microstructures are largely consistent, with small WC grains surrounded by Co, with the preference for eta phase to form near the top surface of the samples though, as expected, there is significant variation between the result of the bead testing and these single-layers, though parameters remained the same in both sample sets.

Table 4.6 Parameters used during raster experimentation, with modeled and measured melt pool depths also shown.

Sample Number	Beam Power	Beam Velocity	Focus Offset (mA)	Energy Density	Max Temp (C)	Mod. Depth: 1350C (µm)	Mod. Depth: 2000C (µm)	Measured Depth (µm)
1	27.8	8	25	8531	2582	386.4	62.3	174.5
2	34.7	8	25	10663	3010	531.7	123.1	357.6
3	43.3	8	25	13308	3585	617.0	206.2	484.7
4	51.9	8	25	15952	4113	714.6	254.5	566.1
5	61.1	8	25	18767	4635	786.5	283.0	633.8

Melt pool depth was also determined for each parameter set, with the results recorded in Table 4.X, along with the modeled melt pool depths for both the 1350°C and 2000°C boundaries. As expected, these measured depths fell between these 1350°C and 2000°C boundaries, with the depths plotted together in Figure 4.17.

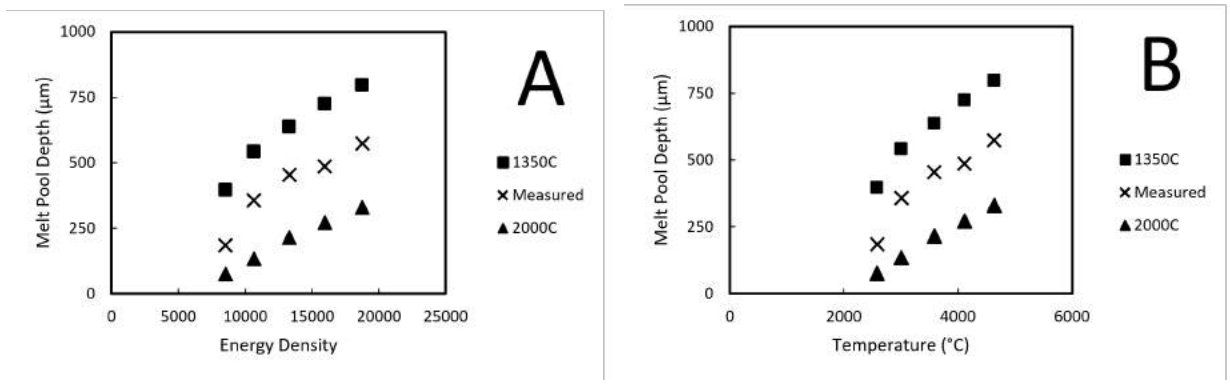

Figure 4.17 Thermal model results for WC-Co single layer tests showing the calculated and measured depths for each parameter set at 1350°C and 2000°C boundaries, relative to both energy density (A) and calculated maximum material temperature (B).

Figure 4.17A shows the average melt pool depth as measured from each sample along with the predicted melt pool depths calculated from the thermal model results, all plotted against

the energy density for each sample set. The melt pools were measured by taking the average depth of observable microstructural changes from the surface of the melted layer, giving a definitive upper bound on the depth at which any microstructural change would occur. The observed trend mirrors that found in the WC-Co bead testing, though the melt pool depths appear to follow the 2000°C depths less closely than in the bead testing. This trend is also seen in Figure 4.17B, where measured depth is plotted against modeled melt pool temperature, along with the modeled melt pool depths for the 1350°C and 2000°C lines.

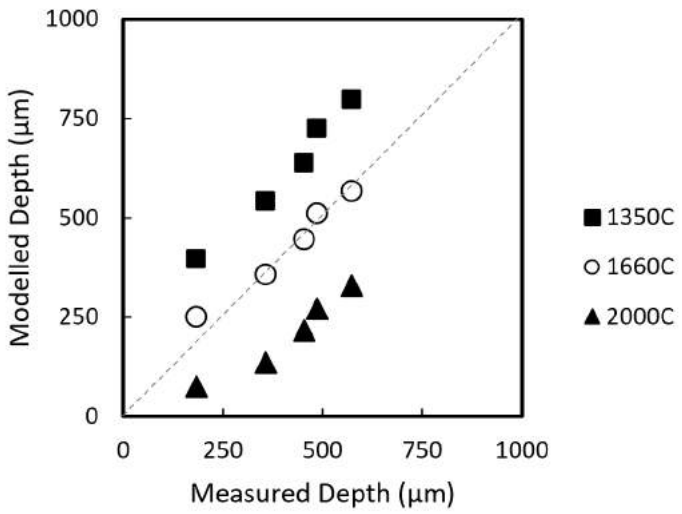

Figure 4.18 Thermal model results for WC-Co bead tests showing the modeled depths for each parameter set at 1350°C, 2000°C boundaries, and the projected contour line of 1660°C plotted against to the measured depths for each parameter set. An 'ideal' 1:1 correlation is represented by the dashed grey line.

When plotting modeled melt pool depths against measured melt pool depths, as shown in Figure 4.18, allows for a better comparison of the accuracy of the modeled depths to those measured. As in the bead experimentation, the relationship between the measured and modeled depths is largely linear, though this linearity does appear to break down at the extremes in energy density and temperature. Figure 4.18 also presents the modeled vs. measured depths for the boundary line at 1660°C that was found to be most accurate for predicting melt pool depth. By taking the average difference between measured and simulated depth per degree C, the temperature boundary that best predicts the real melt pool depths in the single layer experimentation is 1660°C, accurately predicting melt pool depth with less than 5.5% deviation in all but one sample; that of the lowest energy density parameter set. This 'ideal' contour line

of 1660°C differs significantly from that calculated for the bead test experimentation; however, due to the markedly different experimentation conditions, a significant change is expected, with the fundamental trends and observations shown in both experiments.

4.2.6 WC-Co Multi-Layer Experimentation

Additionally, limited proof-of-concept, select multi-layer WC-11Co builds were examined to improve on broader methodology applicability, as bead test and single layer experimentation differ from full-scale AM.

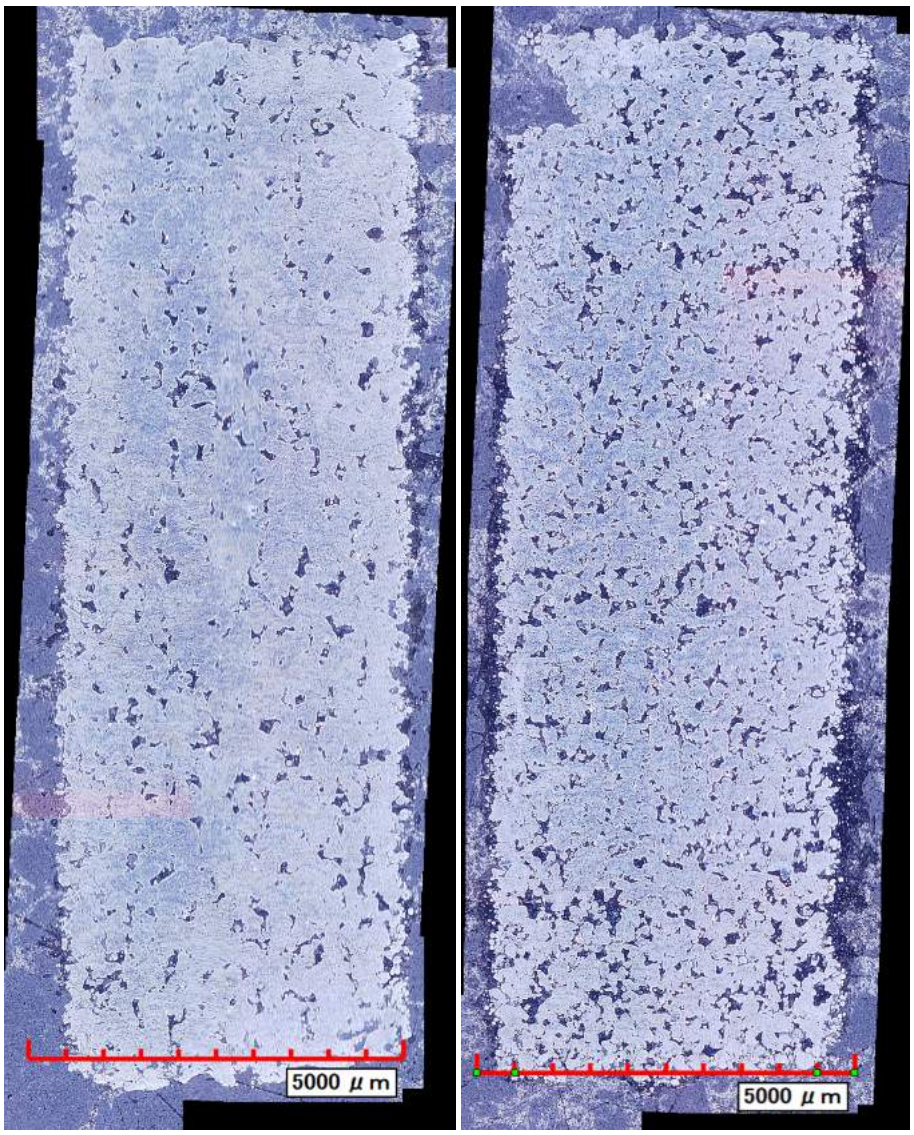

Figure 4.19 Optical microscopy images of representative cross-sections of WC-Co multi-layer builds.

The manufactured samples shown in cross-section in Figure 4.19 were manufactured in an Arcam Q10+ atop WC-11Co substrate, similar to that used in the WC-Co bead tests. These samples were then examined via optical microscopy to examine the viability of the methodology to full-scale AM. Analysis of the internal microstructures was performed to observed the effect of the multi-layer EBM process on the WC-Co alloy, with typical sample geometry shown in Figure 4.19 in cross-section. This optical microscopy imaging shows large scale microstructural features typical of the EBM of WC-Co, such as porosity, cracking, and part surface irregularity, with similar observations reported from EB PBF of WC-Co [95].

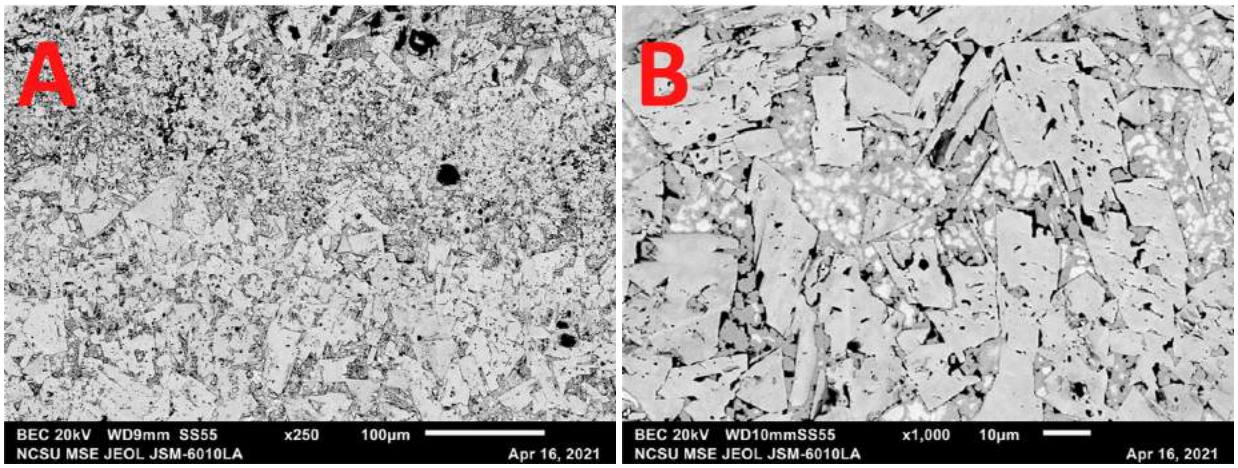

Figure 4.20 Representative SEM micrographs of the cross-sections of WC-Co multi-layer builds taken at A) 250x magnification and B) 1000x magnification.

Closer inspection of the as-built samples, shown in Figure 4.20, reveals a wide distribution of WC grain sizes, and is often a bimodal distribution, which is especially clear in Figure 4.20A. At greater magnifications, as shown in Figure 4.20B, a light gray, globular phase is observable in the Co matrix between WC grain. Given the images were taken in backscatter detection mode on the SEM, it can be inferred that this phase contains heavier element(s) than Co. Utilizing the generated binary phase diagram for this alloy system, the W6C6Co eta phase is the likeliest candidate for the constituent of this phase due to the likelihood of a decrease in C and/or Co content. This change in composition is indicated by the presence of spherical porosities formed by gas evolution observed in WC-Co experimentation. XRD analysis confirms this to be the case, as significant eta phase was detect in all manufactured WC-Co.

When plotting the gather XRD data, as shown in Figure 4.21, clear trends can be observed, with higher modeled melt pool temperatures (Figure 4.21A) and higher energy densities (Figure 4.21B) correlating with higher eta phase content within the material. While both factors are

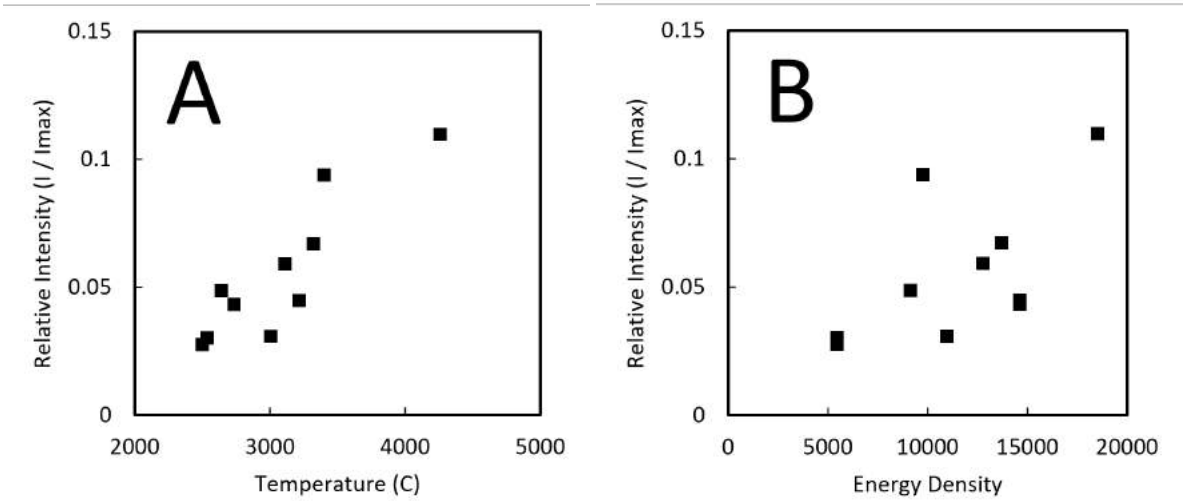

Figure 4.21 Plotting XRD data of eta phase peak intensity against A) modeled temperature and B) energy density for as-built WC-Co samples.

generally indicative of this trend, the correlation is much stronger when plotting eta phase peak against modeled temperature as opposed to energy density.

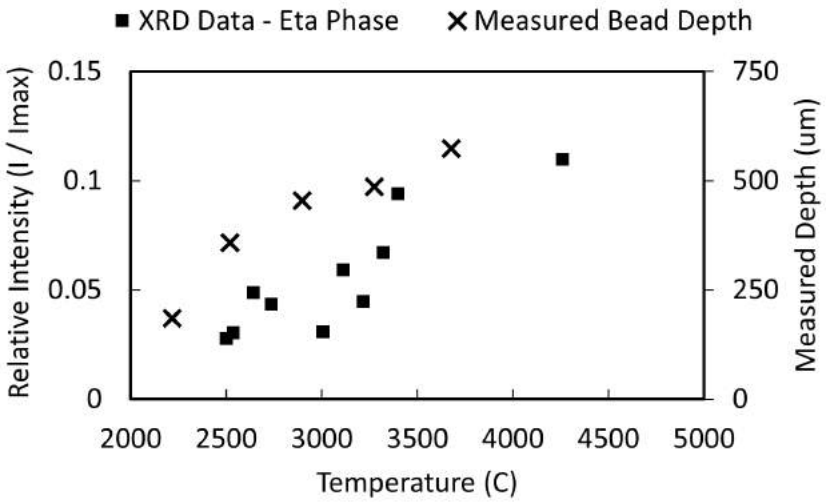

Figure 4.22 Combined plot of relative intensity of eta phase peak from XRD data and measured single-layer depth against average maximum modeled temperature.

The thermal modeling data has been shown to consistently provide more accurate and precise prediction of actual PBF characteristics than other commonly utilized metrics such

as energy density, in both bead testing, single-layer, and multi-layer WC-Co experimentation. Additionally, this thermal data can be combined with the phase compositional data from XRD analysis to target specific properties of the parameter space of WC-Co EBM. Figure 4.22 illustrates this combination of calculated thermal and thermodyamic information with experimental data, showing eta phase composition and melt pool depth as they change with modeled melt pool temperature. Given the detrimental properties of the eta phase in WC-Co as well as the necessity of forming layers that adhere to one another in the vertical direction, this data can be used to determine a practical balance of the two variables by predicting the maximum eta phase composition allowable, while still maintaining a cohesive part. This opens up additional processing paths as well, such as HIP after EBM, which may be a viable option if phase composition is optimal but part density is not.

4.3 Mo-TiC Results

4.3.1 Mo-Ti-C Powder System

This section studies the Mo-Ti-C system as an extension of previous work looking into the development of AM processing of MoTiC alloys for use in fusion applications. The additive manufacturing of MMC's, especially those including refractories, has been the subject of limited additive manufacturing research [74, 97]. The preceding research on WC-Co was useful as a foundational analysis of the EBM process on refractory MMC's in general, and compositional control specifically, within a system similar to Mo-TiC, but utilizing a well-researched and better understood system.

Previous research has covered limited EBM of Mo-TiC, and this present work sought to further the scope of that research as well as incorporate insight provided by previous work to improve model applicability. This prior study, which utilized a 10.5 wt.% Ti - 1.9 wt.% C starting powder, is located in a significantly different space on the phase diagram, and thus will be useful in expanding the methodology to very different compositions. That work showed that small changes in local and global compositions resulted in significant changes to internal microstructures. The present research utilized a nominal composition of 40wt%Mo and 60wt% TiC to explore a different phase space of the Mo-TiC system from previous research, confirmed by EDS and XRF.

The powder produced was validated in their phase content by XRD. XRD also being performed later on melted samples to quantify any subsequent changes in composition as well as ensure that the incorporation of unintended elements did not occur at any point in the processing of Mo-TiC samples. The XRD spectra for each composition are shown in Figure

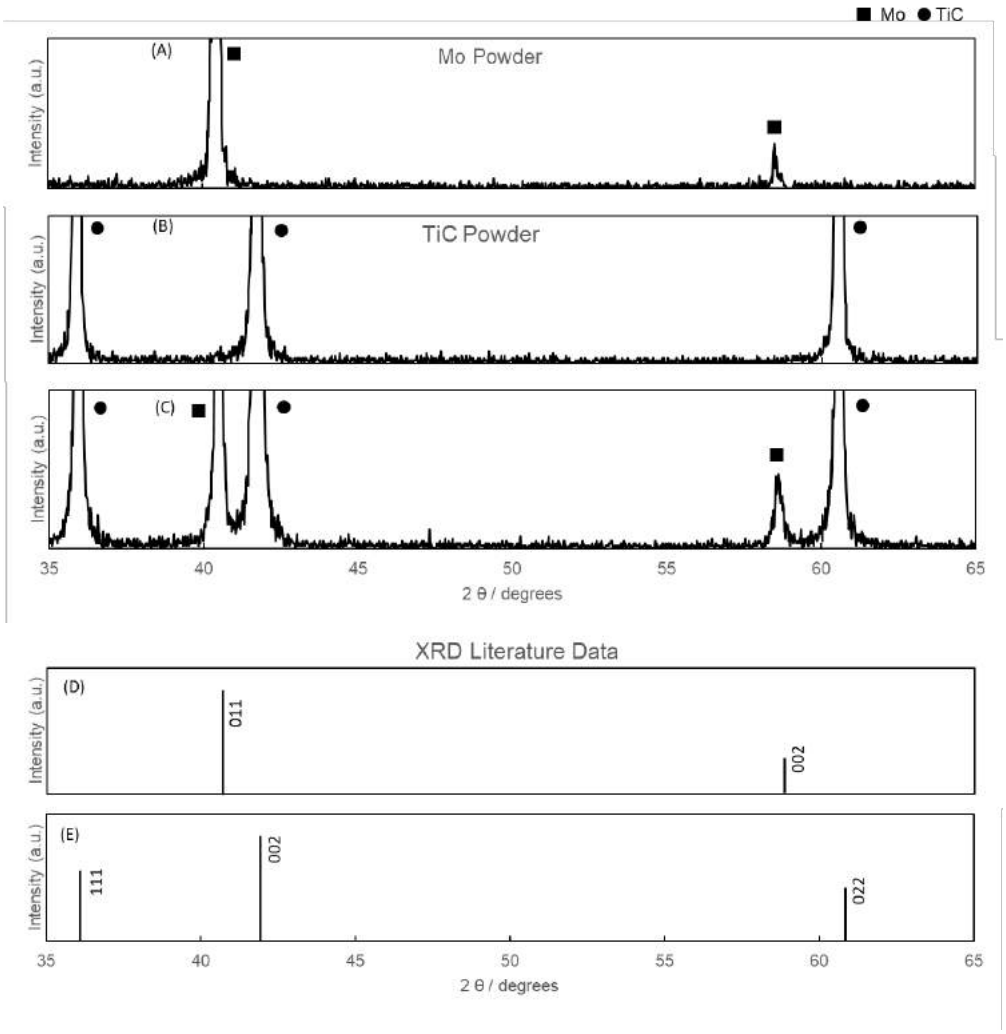

Figure 4.23 Identified phases in starting and blended powders via XRD, as compared with literature data for (D) Mo [149] and (E) TiC [150].

4.23, and reveal no unexpected phases, with only the starting molybdenum and TiC phases being detected.

The morphology of the as-blended powder at 8 hours milling time was also characterized to ensure the blending was sufficient in combining the two powders into a uniform starting powder. Figure 4.24 presents the PSDs for the starting and blended powders as measured by laser diffraction. For the blended powder, the measured d10-d90 was 0.96-70.3 um, indicating the blending process evenly incorporated both starting powders. Many of the fines present in the starting powder are most likely due to the large fraction of added TiC, since it is not expected that the soft Mo particles would be ground to a small fraction of the original particle size and the fines are comparable to the size range of the measured pure TiC powder.

The SEM micrographs are in line with the PSD results discussed previously, with a large

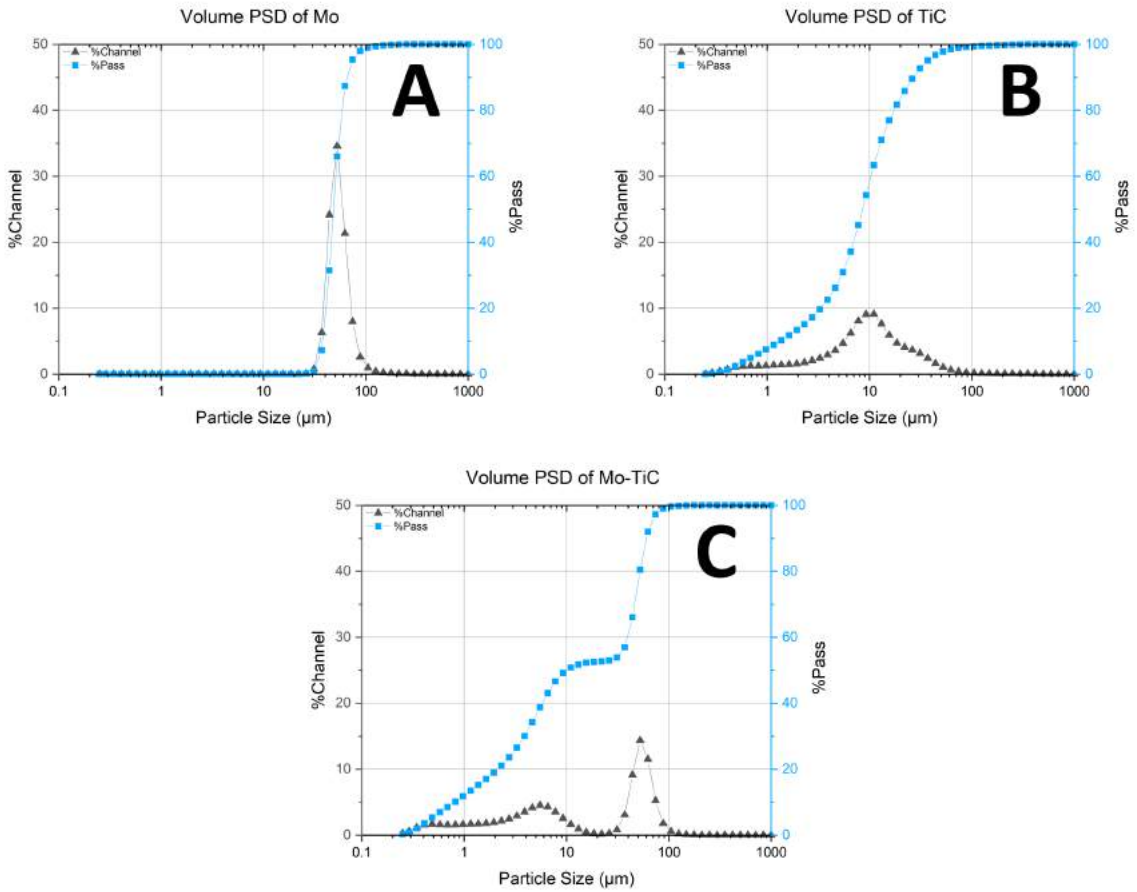

Figure 4.24 Measured PSDs for (A) Mo, (B) TiC, and (C) Mo-TiC powders. Horizontal scale is logarithmic, with frequency denoted the %channel for each size demarcation.

number of both very (1-10um) fine particles and larger particles (40-70um) observed. SEM analysis also reveals the compositional discrepancy between these two distributions, with a preponderance of Mo-rich large particles, and relatively few large TiC particles observed, as shown in Figure 4.25. The inverse is true for the distribution of small particles, with a majority observed to be TiC, while fewer Mo-rich, small diameter particles are observed. This is primarily indicative of the initial PSD of the constituent powders used in the blending process to initially produce the two compositions, with the average particle size being much higher in the starting Mo powder than in the starting TiC powder, as shown previously.

This section shows Thermocalc results of the selected compositions, modeling results from the FEniCS thermal model during rastering on the Mo-TiC MMC, and experimental observations of the raster and how the models and experimental results relate. From an experimental standpoint, the goal is to melt the system at many energy densities to target those energies required for layer adherence at the lower ends and those that cause the TiC particles to lose

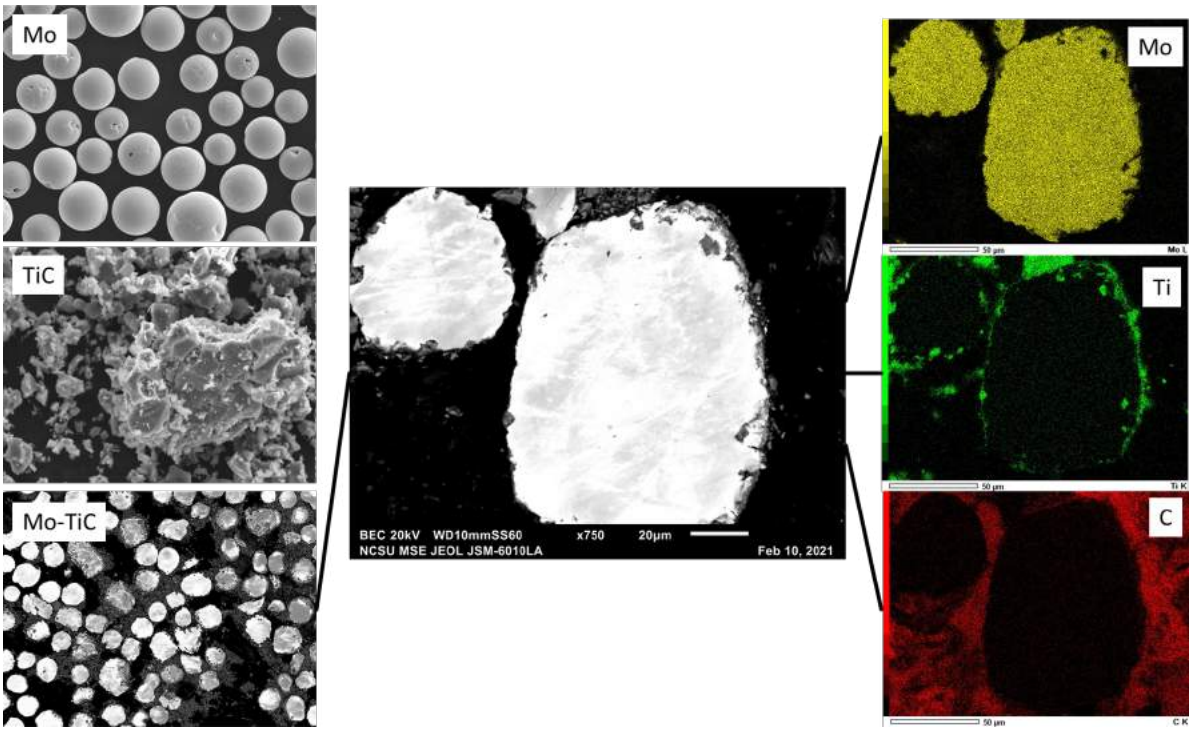

Figure 4.25 SEM micrographs of the blending process results, showing initial component powder morphologies and final powder shape and composition

their dispersoid shape or forms other (non-TiC) phases. This will allow for a wider applicable range of the predictive modeling methodology.

4.3.2 Mo-TiC Thermodynamic Phase Modeling

Ternary phase diagrams were also generated via ThermoCalc, with a wide range of temperatures to better capture the full set of conditions the material experiences during processing, and a representative subset of these diagrams are shown in Figure 4.26. This figure shows Mo, Ti, and C on each axis from 0-100 wt%, with the modeled composition identified by the blue markers at the bottom of each isotherm. Figure 4.26A shows that at 3000°C the material exists in an almost entirely in liquid form at lower carbon compositions. However, upon cooling to 2250°C as shown in Figure 4.26B, the composition lies close to the boundary between two phase spaces, one which includes the HCP, Mo_2C phase and one which does not. This trend remains consistent even as the temperature drops to 1000°C, shown in Figure 4.26C, and lower. This implies that even slight changes in local composition could have significant changes on local microstructures, as the formation of certain phases are or are not present, making this a useful tool to quantify the conditions present locally in the material during melting.

To this end, Figure 4.26 can also be used to approximate the desired process temperatures

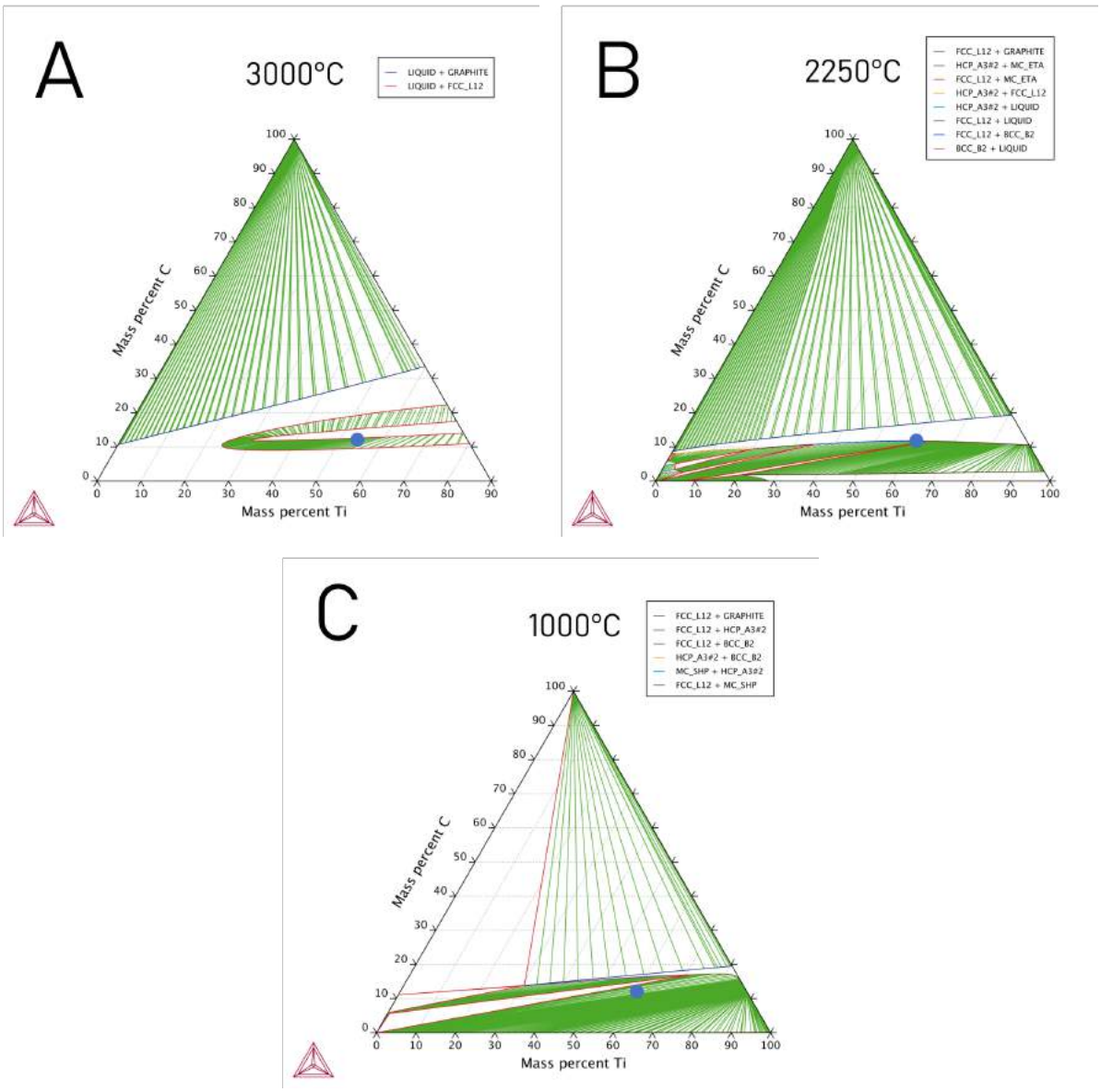

Figure 4.26 Generated ternary phase diagrams show phase space changes as the temperature decreases.

that would prevent the dissolution of the TiC particles at the produced powder composition.The significant solubility of Mo in TiC, as reported by Kitsunai et al., decreases the solidification temperature of the FCC TiC phase, which is an important factor in the decrease in melting temperature of TiC from 3160°C alone to approximately 2750°C, according the the phase diagram in Figure 4.26. The result of which is that, should the liquid Mo impregnate the TiC particle, those particles may melt and stay liquid for longer, re-solidifying at a much lower temperature than would be expected of pure TiC. This same effect would take place should

any TiC particles melt and mix with the surrounding molten Mo.

This data matches well with thermodynamic modeling from Shim et al. and Ida et al. where they reported on the CALPHAD method in the Mo-Ti-C system. Illustrated in all ternaries, however, is that the detrimental Mo_2C phase will likely be difficult to prevent from forming due to the close proximity of the powder composition to the phase boundary. If combined with thermal modeling data, these diagram can help guide parameter development through better understanding the effect of heating on potential microstructures.

4.3.3 Mo-TiC Thermal Modeling

Table 4.7 Parameters used during Mo-TiC experimentation, with maximum modeled temperature vs dimensionless energy density for three sets of parameters.

Group (Sample #)	Beam Power	Beam Velocity	Line Offset (mm)
A 1	67.5	35.7	0.05
A 2	80.0	30.2	0.05
A 3	94.5	25.5	0.05
B 1	71.1	13.3	0.05
B 2	26.7	1.67	0.15
B 3	53.3	3.33	0.15
C 1	26.7	1.67	0.05
C 2	53.3	3.33	0.05

The phase diagrams produced by the thermodynamic model are crucial in developing a simple, fast, but useful representation of the conditions experienced within the melt pool due to the difficulty of accurately gathering information as to the nature of the phases and their formation in custom or under-researched alloys. Once this information is in hand, however, the relationship between machine parameters and useful regions of these phase diagrams can be investigated. The parameters used in the thermal modeling and experimentation are detailed in Table 4.7.

Figure 4.27 plots maximum average temperature of each parameter set from the model against energy density to estimate the effects of parameters on material temperature. The three labelled groups indicated in Figure 4.27 were split for analysis purposes, allowing for easier comparison between changes in specific parameters between samples. Group A is made up of three different, equidistant energy densities: (1) 5445, (2) 7626, and (3) 10661. Each energy

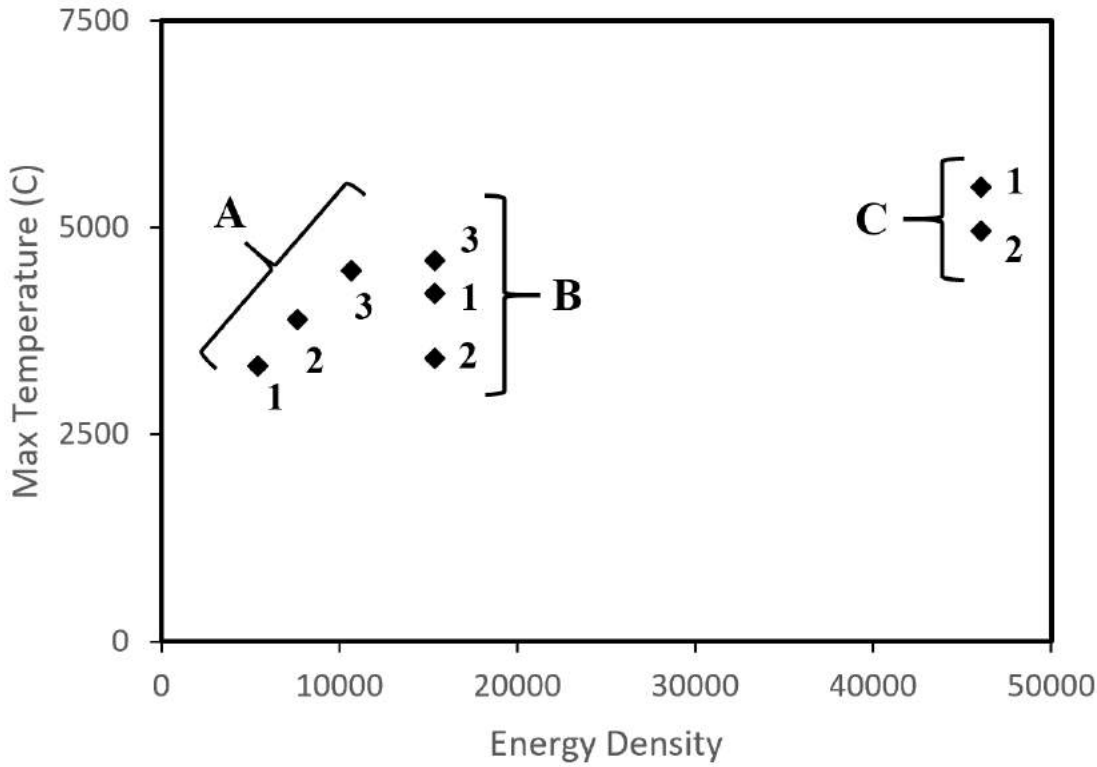

Figure 4.27 Parameters used during Mo-TiC experimentation, with maximum modeled temperature vs dimensionless energy density for three sets of parameters.

density value is a factor of 1.4 smaller or larger than the adjacent parameter set, with power and velocity adjusted proportionally. In this way, the effect of a change energy density can be analyzed independent of the change in velocity or beam power. Group B is made up of three equivalent energy densities, all 15355; however, the raster hatch spacing (line offset) was changed from 0.05mm in sample B1 to 0.15mm in Samples B2 and B3. This allows for a better understanding of what effect such line offset variations might have on the model's predictive ability. Group C consists of two very high energy density samples of equal value, which were performed to evaluate to efficacy of the methodology at the extremes of the parameter space. Samples C1 and C2 have the same beam power and velocities as samples B2 and B3, respectively, however the line offset value was changed to 0.05mm, effectively tripling the energy density of the C-group samples.

The results of the thermal model for these parameters are shown in Figure 4.28 consisting of a top view of a 0.03 sec snapshot of the melt pool visualization, with a color scale bar shown, for each beam condition. In Figures 4.28A-C, a positive correlation is seen between energy density and maximum temperature reached; however, introducing line offset changes

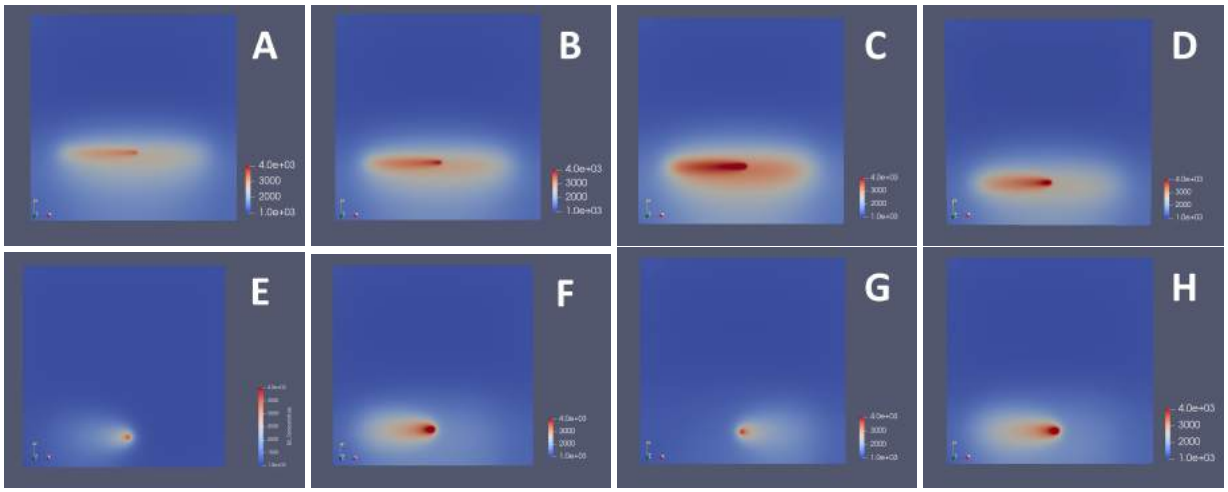

Figure 4.28 Thermal profile for each sample parameter set, showing the average temperature of an area on the simulated surface as it changes with time

modifies the raster by increasing the distance between beam lines which changes the maximum temperatures experienced by the material, even as energy density of the beam remains constant. As expected, the overall temperature of the system tends to increase with increasing energy density, though the changes in line offset indicate that energy density is not the only important raster parameter during EBM.

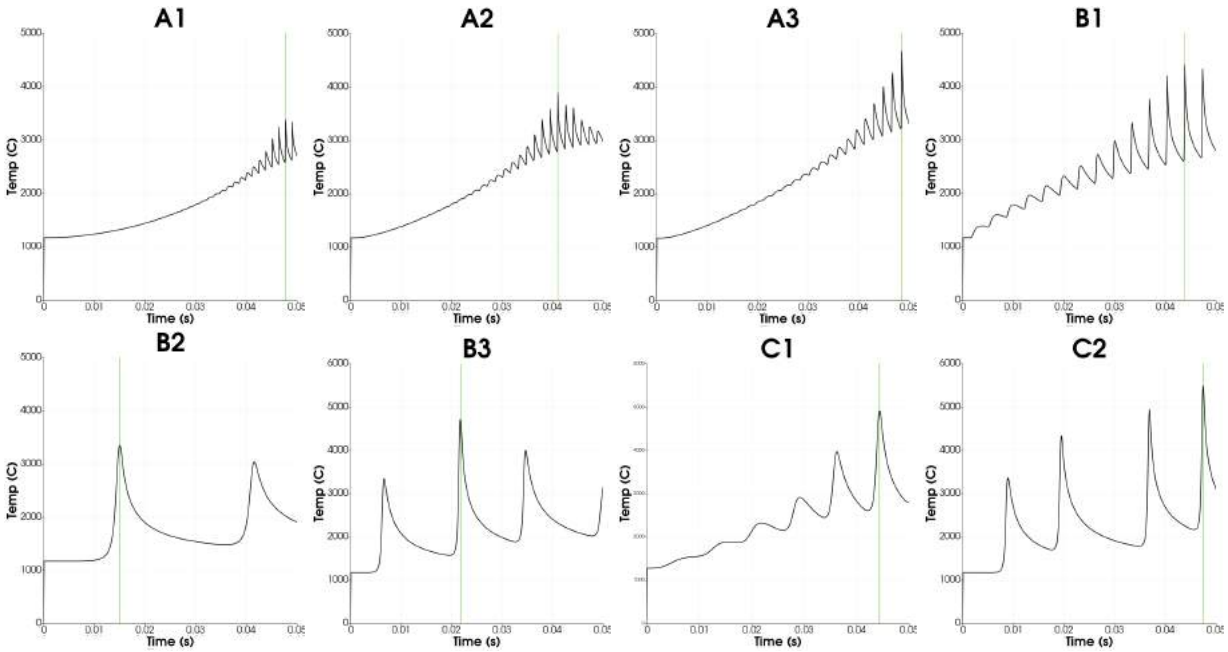

Figure 4.29 Thermal profile for each sample parameter set, showing the average temperature of an specific region of interest on the simulated surface as it changes with time.

The thermal profiles for the hottest region of the given snapshots are shown in Figure 4.29, presenting the average temperature over time of a square of 9 mesh points 75um a side, equivalent to an area of 0.00563mm2. These thermal profiles are associated with each melt condition and provide an estimation of the melt temperature for a given condition. Figure 4.29 shows that parameter set A1, the 5445 energy density condition, produces a maximum temperature rise from 1173K, the base preheat temperature, to 3326°C. This is relatively high, approximately 1000°C higher than the equilibrium melt temperature of Mo for the system composition. As the energy density increases to A2 (7626) and further to A3 (10661), the bead melt pool temperature rises proportionally to 3893°C and then 4480°C, respectively. This maximum temperature of 4480°C is nearly twice the equilibrium melting point of Mo for the system, which will almost certainly lead to full melting of some portion of the material. Taking the parameter sets as a whole, the maximum modeled temperature does generally increase with increasing energy density. However, there are large variations in maximum temperature even as energy density stays the same, as in Groups B and C, an indication that the produced microstructures will shows significant differences, even when energy density remains constant.

Fig 4.30 represents the thermal model by evaluating a cross-sectional view of the beam area to gain insight concerning temperature penetration in the Z-direction within the single layer raster to estimate a melt pool depth. Again, differences between the model conditions and the real-world melting conditions are important to consider, most notably the lack of dynamic information provided by the model, and thus necessitates an estimation of melt pool depth and temperature. In this case, 2250°C and 3250°C were chosen as likely thermal contour lines for bounding the actual boundary between starting powder and observable microstructural changes. A contour line of 2250°C was chosen due to its proximity to the melting temperature of the eutectic composition , as calculated by the generated phase diagram shown in Figure 4.30. As shown in the previous WC-Co experimentation, in practice such a value would likely overestimate the melt pool depths due to the numerous of factors previously outlined. A second temperature of 3250°C was chosen as this temperature is just above the melting temperature of pure TiC, and thus even short exposures at these temperatures were likely to be visible in the resultant microstructures. Additionally, 3250°C was the highest temperature contour line that was visible in all parameter sets. These two values allow for a range of possible profiles, necessary due to the highly non-equilibrium conditions associated with 3D printing.

At the lowest energy density value of 5445, the contour line for a temperature of 3250°C reaches 99.7um into the solid surface, with the temperature dropping below 2250°C within 500um, as described in Table 4.8. Again, as the energy density increases, the bead temperature is significantly impacted. By an energy density of 10662, the temperature is nearly 4500°C, with the contour depths reaching 345.9um and 694.4um for the 3250°C and 2250°C boundaries,

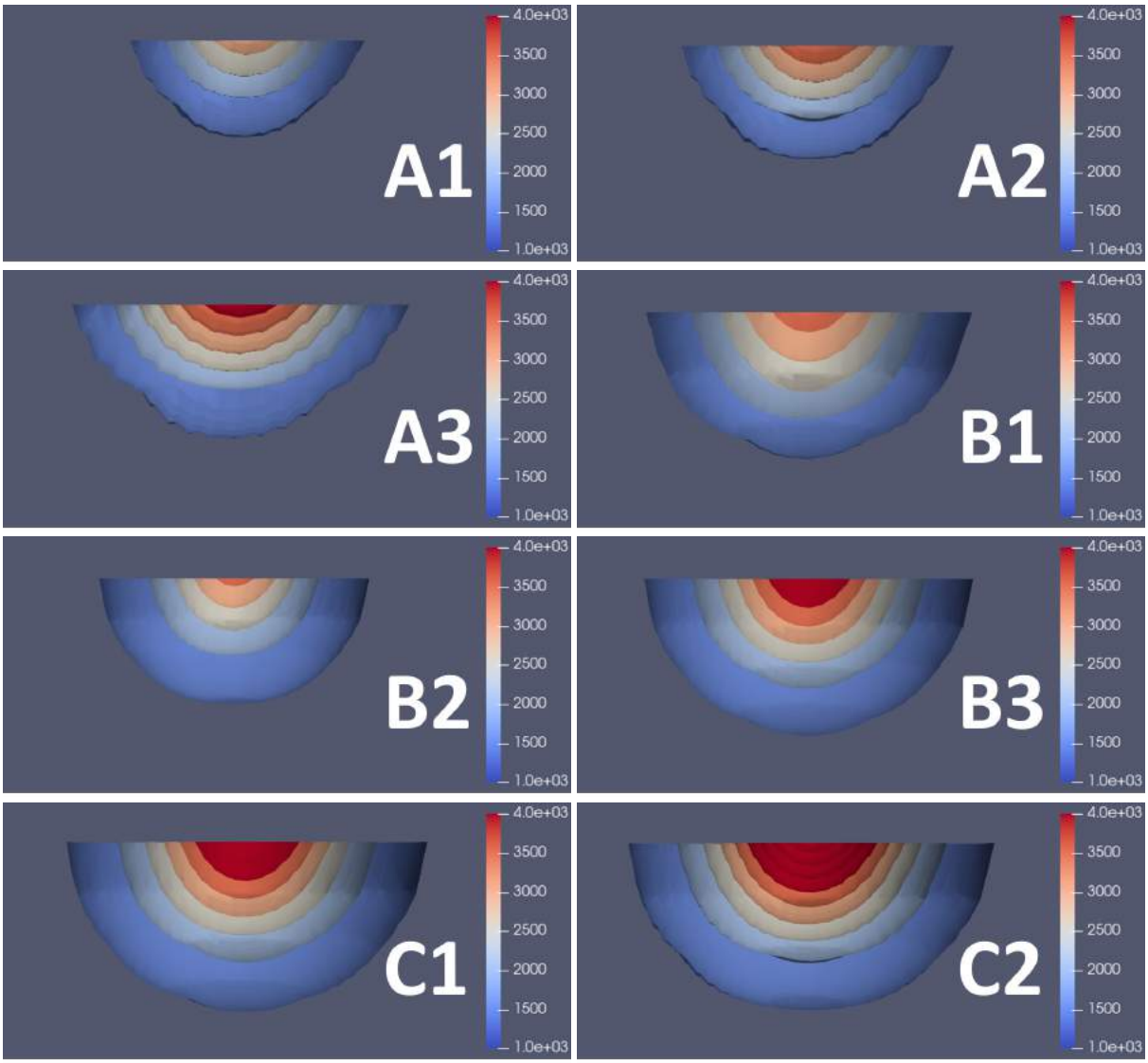

Figure 4.30 Thermal Profile contour results for MoTiC

respectively, and thus this system likely fully melted near the surface. The model estimates that the melt pool becomes further exaggerated with depths in excess of 500um as the energy density of the beam exceeds 15000, resulting in a processing space which is far more extreme than any solid state or LPS process. These results show that temperatures significantly higher than the melting point of molybdenum, such as the maximum average temperature of 3326°C of the lowest energy density parameter, are necessary to produce a cohesive, single layer during experimentation. Even at such temperatures, the predicted melt pool depth reaches only 100um-435um in depth, with this lower bound hardly larger than the Mo particles themselves.

Table 4.8 Parameters used during experimentation, with maximum modeled temperature, 2250°C and 3250°C contour line depths, along with dimensionless beam velocity, power, and energy density for each Mo-TiC parameter set

Group (Sample #)	Beam Power	Beam Velocity	Line Offset (mm)	Energy Density	Max Temp (C)	Mod. Depth: 2250C (μm)	Mod. Depth: 3250C (μm)
A 1	67.5	35.7	0.05	5445	3326	434.6	99.7
A 2	80.0	30.2	0.05	7626	3893	593.9	184.1
A 3	94.5	25.5	0.05	10661	4480	694.4	345.9
B 1	71.1	13.3	0.05	15355	4208	617.1	255.3
B 2	26.7	1.67	0.15	15355	3423	534.8	139.3
B 3	53.3	3.33	0.15	15355	4607	800.9	391.4
C 1	26.7	1.67	0.05	46065	4961	868.7	452.9
C 2	53.3	3.33	0.05	46065	5495	932.6	567.6

4.3.4 Mo-TiC Combination of Models

Thermal profile data is leveraged to guide thermodynamic calculation boundary conditions for temperature and a conception of the process can begin to be formed, while remaining flexible enough to accommodate adjustments later in the process based on the results of experimentation. Microstructure and phase prediction are the main goals of this methodology, and in a controlled environment under equilibrium conditions ThermoCalc alone would be sufficient. However, due to the non-standard nature of AM and its relative fast solidification rates, as well as the difficulty in validating accurate temperature information during experimentation, the thermal model is used in conjunction with ThermoCalc to evaluate the path the material takes through the processing space.

Figure 4.31 shows the pseudo-binary phase diagram that is generated for the Mo-TiC system by ThermoCalc, using TiC9 database, with mass% of C on the X-axis and Mo balance. These results also correspond well with those presented by Shim et al., and is useful in examining the potential effect of compositional changes, with this particular diagram assuming Ti content remains approximately the same. The diagram shows that significant HCP Mo_2C is expected to form after TiC has re-solidified. However, this assumes that the TiC particulates are fully melted and their components homogeneously mixed in the system, which, though unlikely, illustrates the motivation to maintain a discrete second phase through methodological process control.

From the thermal model, a temperature profile was found that caused temperatures experienced by the material were sufficient enough to melt the Molybdenum components. This is the minimum effect that must occur to ensure a continuous, dense melted layer to be formed during experimentation. This thermal profile was then mapped onto the phase diagrams gen-

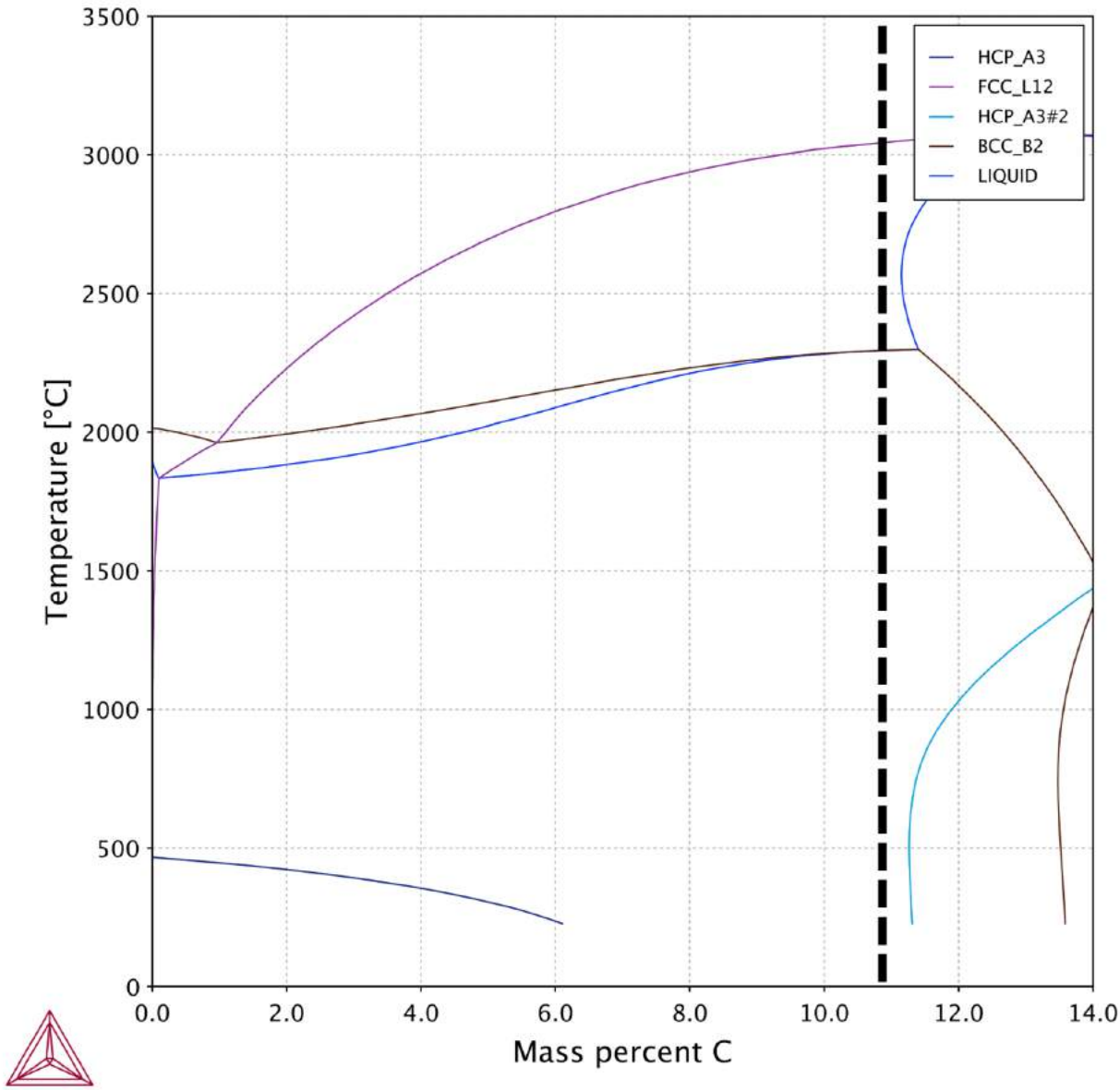

Figure 4.31 Generated binary phase diagram showing the location of the MoTiC composition relative to mass percent carbon. Dashed line indicates approximate location of as-blended Mo-TiC composition.

erated for the specific composition, as indicated by the dashed line in Figure 4.31, while also allowing for slight compositional changes that are expected during processing.

The presence of phases outside this region would indicate either compositions and/or temperatures outside those predicted by the modeling work. The information generated from these diagrams and the thermal model will be used in conjunction with that taken from existing literature to predict and identify phases formed with the material as a response to interaction

with the electron beam, with predictions subsequently by additional experimental results.

4.3.5 Mo-TiC Single-Layer Experimentation

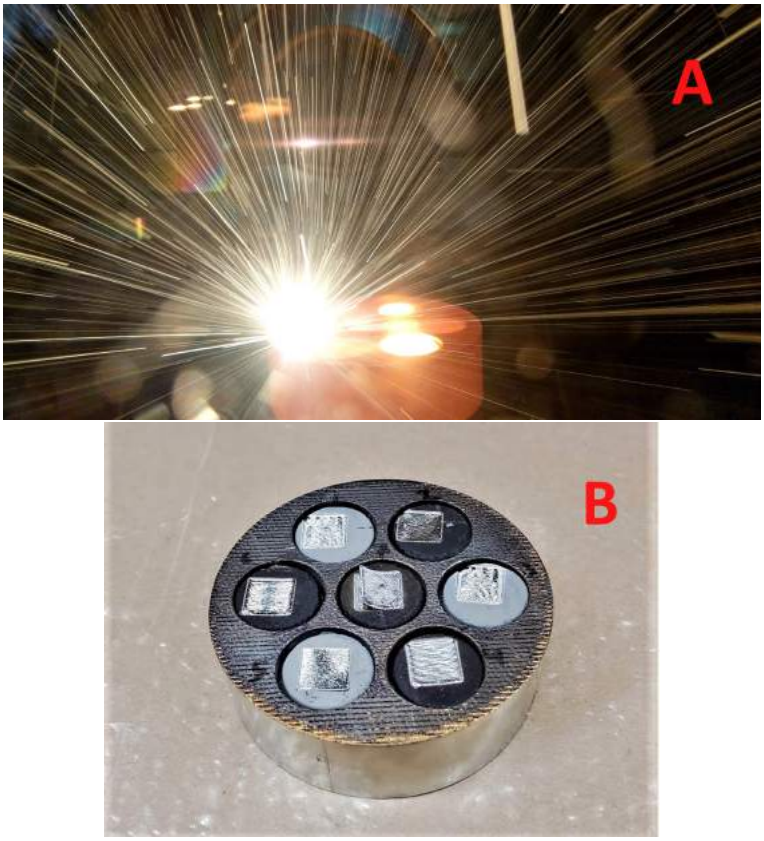

Figure 4.32 Image of spatter generated during Mo-TiC samples experimentation, and representative experimental samples post-processing in the EBM machine

Initial experimentation utilized parameters drawn from prior research that produced solid, cohesive parts [112]. The experimental setup during and after melting is shown in Figures 4.32A and B, respectively, with Figure 4.32B showing the sample surfaces as they have been melted by the beam. Figure 4.32A shows a representative photograph taken during the rastering of the Mo-TiC pucks, and shows a large quantity of spatter generated during melting. While this is a significant degree of spatter formation, no obvious interruptions of the process occurred. The produced spatter is likely the result of the ejection of the fine TiC particles, which was expected to some degree due to the lack of full incorporation of the TiC into molybdenum. The custom, multi-socketed design allowed for multiple parameter sets to be performed at once, serving to increase experimental efficiency.

The electron beam was used to heat the socket plate with a current of 16mA, until the plate was relatively stable near 900°C, as measured by the machine thermocouple and two-color pyrometer. This melting process and use of pressed pucks was utilized to emulate the EBM process, while introducing as few additional variables as possible. The top surface of each pellet was then melted with the raster parameters corresponding to those calculated and shown in Table 4.7. This method of heating and melting was used to emulate the standard Arcam layer melt process while still only melting a single layer.

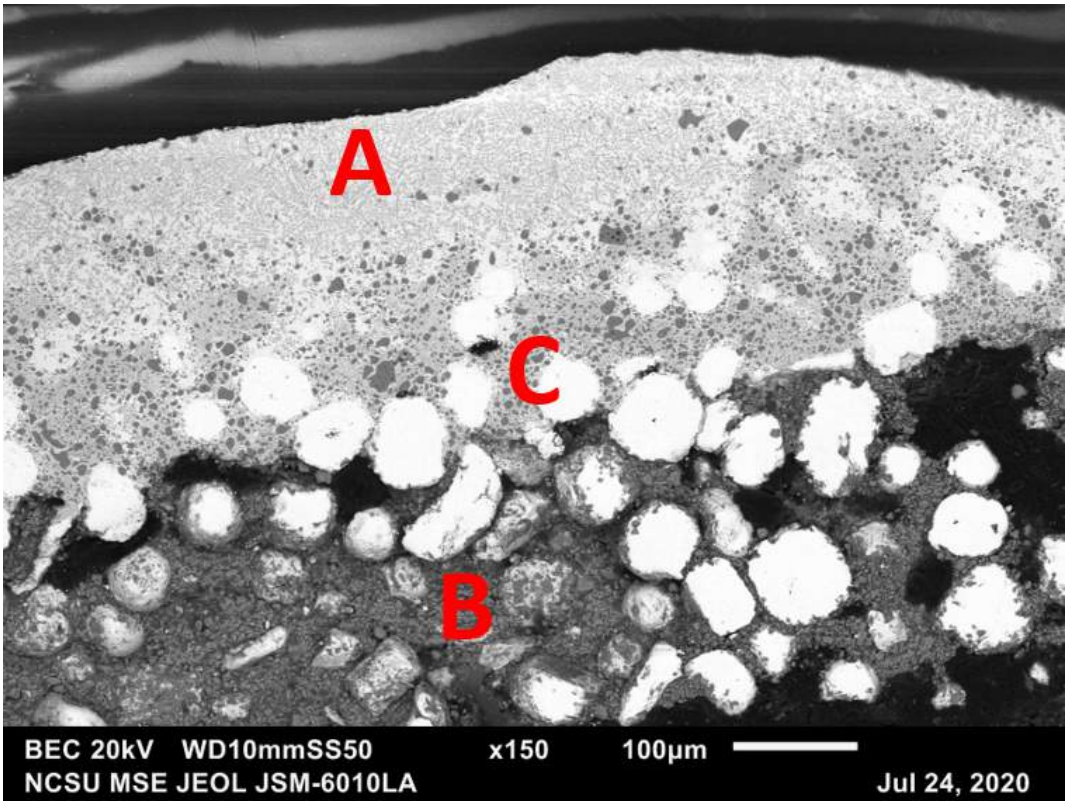

Figure 4.33 Representative low magnification SEM image illustrating general trends within the Mo-TiC samples, denoting commonly observed regions where A) the material is fully melted, B) no microstructural changes are observed, and C) the area of transition between the two.

On a macroscopic level, the overall morphology of the melted sample cross-sections is as expected from similar literature analysis of single-layer additive manufacturing (Chen). The cross-sections for all samples can be divided into three distinct regions, all of which can be seen in Figure 4.33, a sample with typical microstructures, and melted at an energy density of 15355 and a line offset of 0.15mm. These three regions are (A) the clearly melted and re-solidified region along on top, (B) the largely unaffected region of unmelted powder along the

bottom, and (C) the area of transition between (A) and (B). This observation also supports the contour modeling results, shown previously, that indicated the temperatures reached beyond approximately 1mm from the melted surface would be insufficient for significant phase changes to occur within any parameter set.

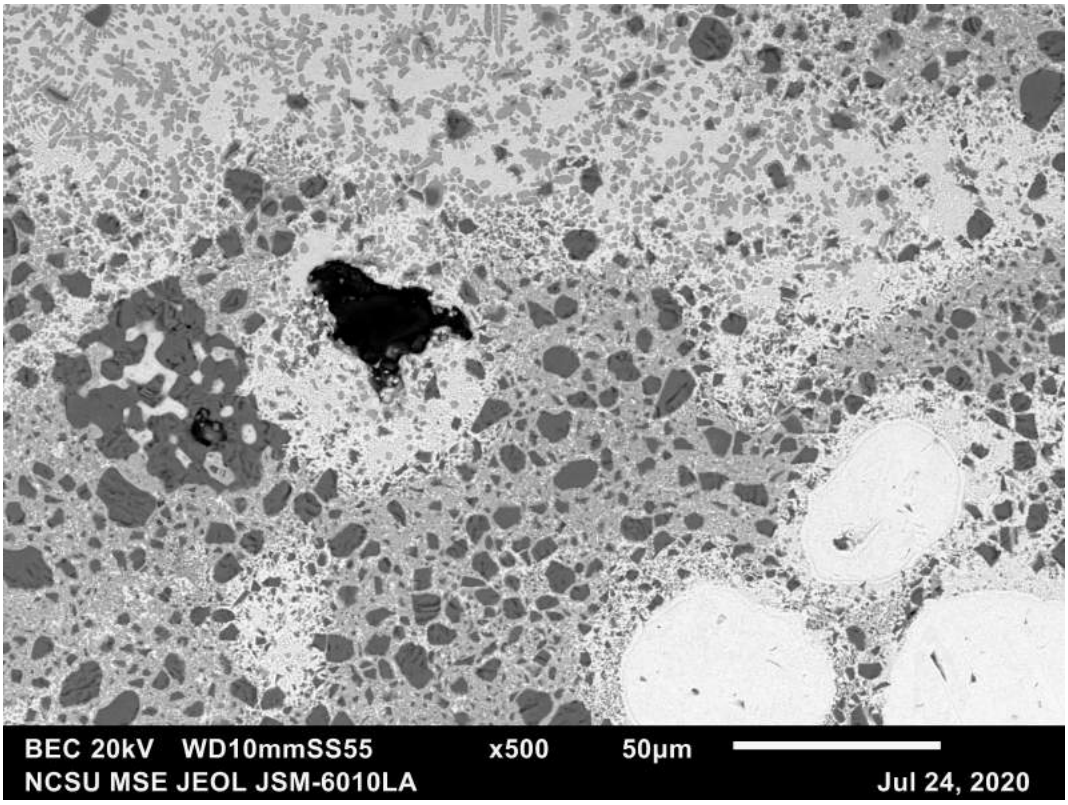

Figure 4.34 Close-up images of typical porosity observed in Mo-TiC samples

The samples exhibited an irregular surface with a wide variety of phases and structures. The observed microstructures were largely the same between sample parameter sets, with an representative sample image shown in Figure 4.34, and will be covered in more detail in the following sections. Macroscopic cracking, a feature commonly reported by studies involving the AM of refractories, was not observed in any samples [35]. Whether larger-scale AM productions with this composition would exhibit significant cracking cannot be determined solely from this study

Porosity was observed in every parameter set, and while each sample contained some degree of porosity, the quantity and morphology varied across parameter sets. Fine, intra-granular pores can be seen in Figure 4.34, and are often found near Mo-rich regions. These porosities also form most numerously in or near to the transition region between the fully

melted surface and the entirely unmelted substrate, indicating their existence is likely due to persistence of pores from the powder compact and incomplete melting that failed to fully densify the region. Given the single-layer nature of experimentation, as well as the dynamic limitations of the thermal model, porosity analysis was not an major factor in experimentation or analysis

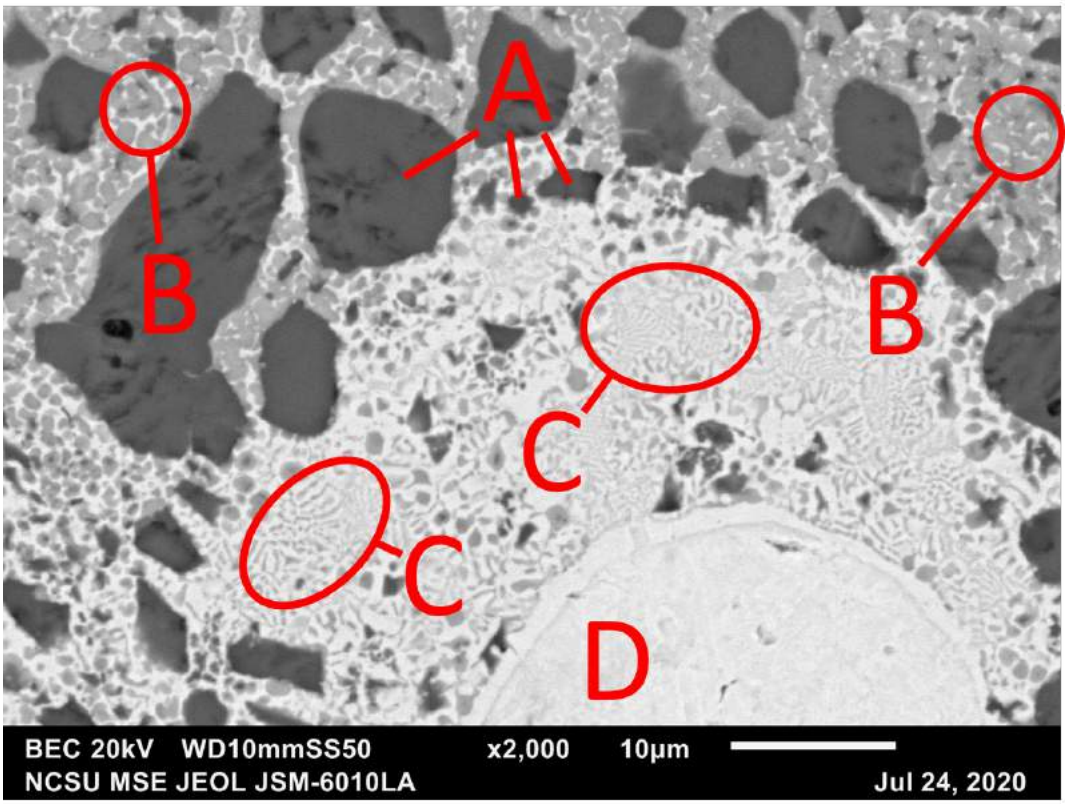

Figure 4.35 Representative, large magnification image of various regions found in the Mo-TiC samples.

Figure 4.35 is a representative image of the most prominent microstructural features observed in the Mo-TiC samples. These most common features are (A) the approximately 10um large, dark, and unmelted TiC particles, (B) the precipitated, commonly dendritic TiC-rich structures, (C) the very fine, Mo-rich lamellar structure, and (D) fully unmelted Mo particles. This terminology will be used to reference sample features in the following discussions. The lamellar structures are observed most often adjacent to or in the shape of unmelted Mo-rich particles similar in morphology and composition to the starting powder.

The general identification of these microstructural regions was confirmed by EDS results

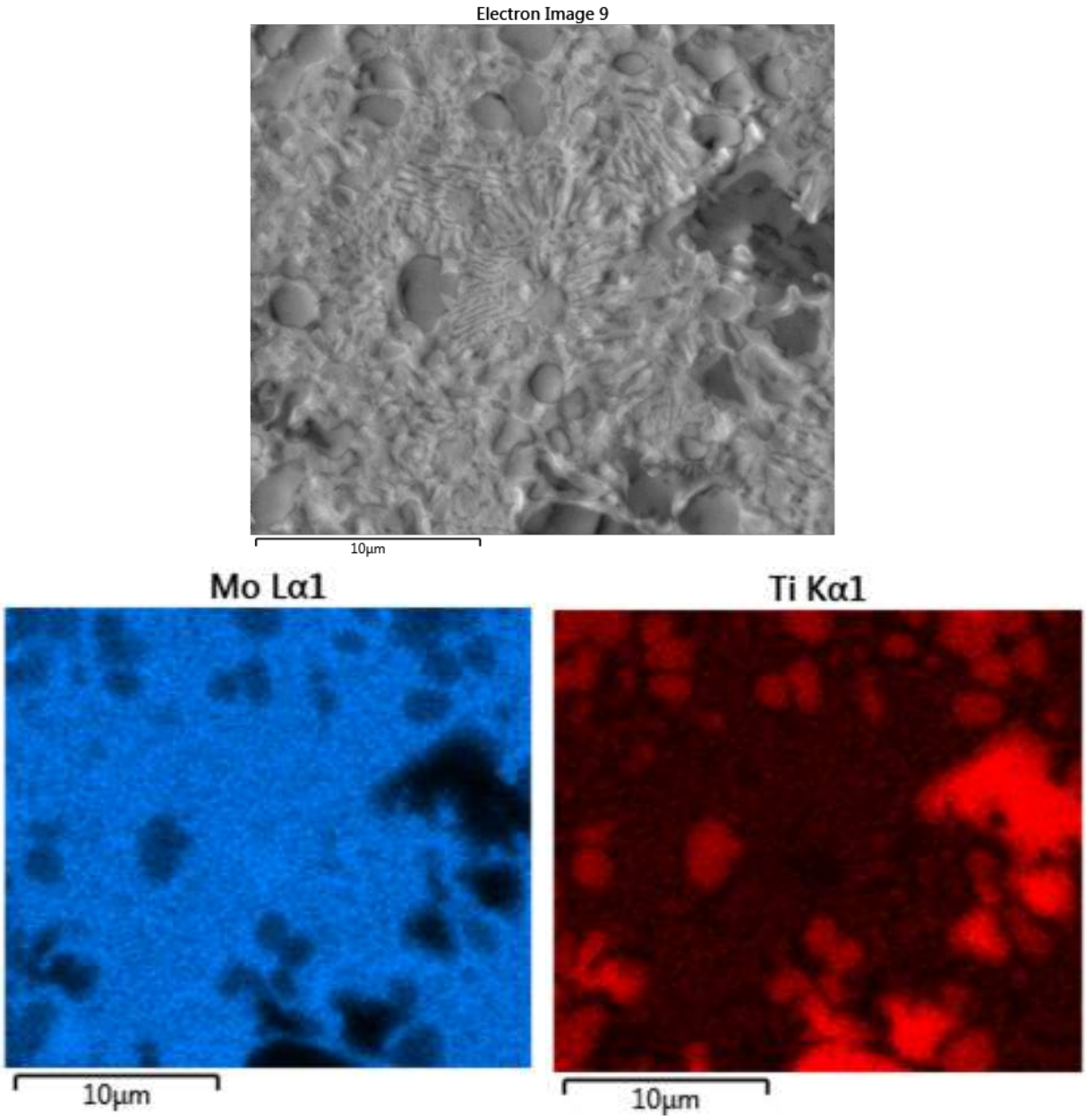

Figure 4.36 Representative EDS of Mo-rich eutectic regions in Mo-TiC samples from Group I.

shown in Figure 4.36A. Figure 4.36 shows SEM (top) and EDS maps (bottom) taken of a sample from the parameter set B2, and illustrates a common morphology of these Mo-rich, eutectic regions that contain a very fine lamellar structure and which are often surrounded by TiC-rich particulates. Given their small scale, these fine lamellar structures are difficult to image and resolve, as shown through EDS of the structures, with individual bands being submicron in size and unable to be resolve via EDS detection. Here the FEI Quanta was used to identify the general composition structures, where Mo and Ti are the predominant detected elements, which is

consistent with previous work. This implies that these eutectic regions are likely a combination of TiC-rich and Mo-rich bands, with the largest areas of lamellar structures created as a result of fully melted Mo particles, which appears in Figure 4.36 as a circular region of Mo-rich eutectic surrounded by TiC particles in a Mo-rich matrix.

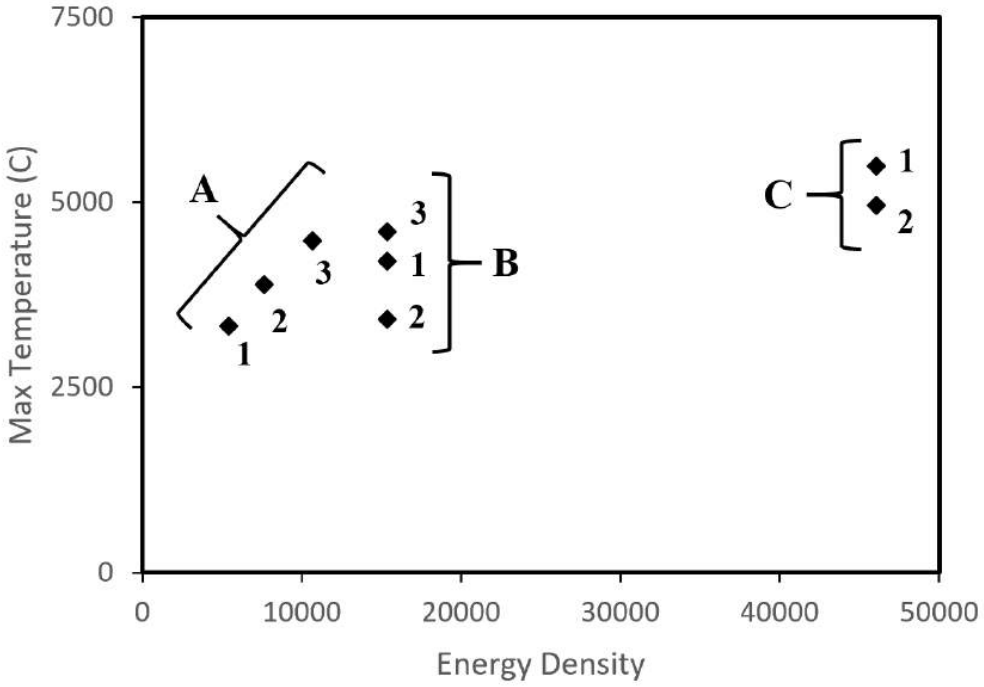

Figure 4.37 Parameters used during Mo-TiC experimentation, with maximum modeled temperature vs dimensionless energy density for three sets of parameters.

For clarity, the samples and associated groups are again shown in Figure 4.37, with the maximum modeled temperature for each parameter set plotted against beam energy density. This sample nomenclature will be used throughout the following discussions.

Figure 4.38 is a composite of the results from Group A, with contour thermal model results on the top, low magnification SEM image of the cross-section of the melted puck surface. The energy density of the samples increases from left to right. from 5445 to 7626 to 10662 for A1, A2, and A3, respectively. As expected, A1, with the lowest energy density, had the smallest average sample depth, as also shown by cross-section thermal model the included contour models in Figure 4.38. In the leftmost image of Figure 4.38, the melted region of the lowest energy density sample A1 is shown to be very shallow, and A1 is the only parameter set in which the transition region was found to be larger, on average, than the fully melted region.

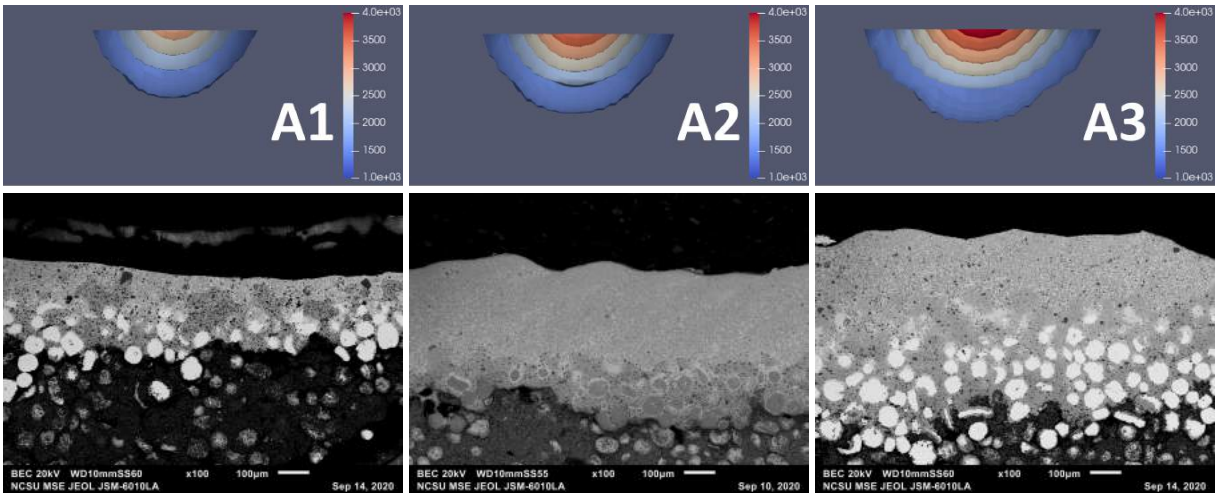

Figure 4.38 Representative, small magnification images of samples with associated temperature profiles for the samples of Group I.

This leads to a large portion of the sample being made up of un- or semi-melted Mo and TiC particles persistent from the pressed puck. Such an internal structure leads to a relatively high proportion of discrete and largely unmelted TiC particles found in the solid part of the sample, which itself results in a microstructure more comparable to the results of traditional MMC processing than the other parameter sets of Group A. The higher energy densities of A2 and A3 led to larger melt pool depths, a result that conforms with the thermal model results and broader EBM research.

Figure 4.39 presents representative, higher magnification images taken within the bulk of the melted regions of the samples in 4.39, with these more detailed BEC SEM micrographs showing that unmelted TiC particles, TiC-rich dendritic regions, and Mo-rich eutectic regions are present in all samples, regardless of energy density. Though their individual prevalence varies, overall trends will be discussed later. However, the morphology of the TiC does appear to be influenced by energy density and melt temperature, with more unmelted TiC particles tending to be present at lower energy densities and temperatures.

EDS mapping data is displayed in Figure 4.40 to illustrate the local changes in composition that are observed after melting, as the fine eutectic displayed in the top electron image was never observed in the powder prior to melting. The sample shown in Figure 4.40 was that of A3, and was representative of structures seen in all samples. Overall, the results are as expected from initial SEM analysis, with the dark grey regions being rich in Ti and the lighter grey regions in between being Mo-rich. The detected presence of both Mo and Ti in these lighter grey regions, combined with the observed lamellar structures, clearly indicate a eutectic composition during solidification. Additionally the existence of a high proportion of Ti, and some Mo, in the darker

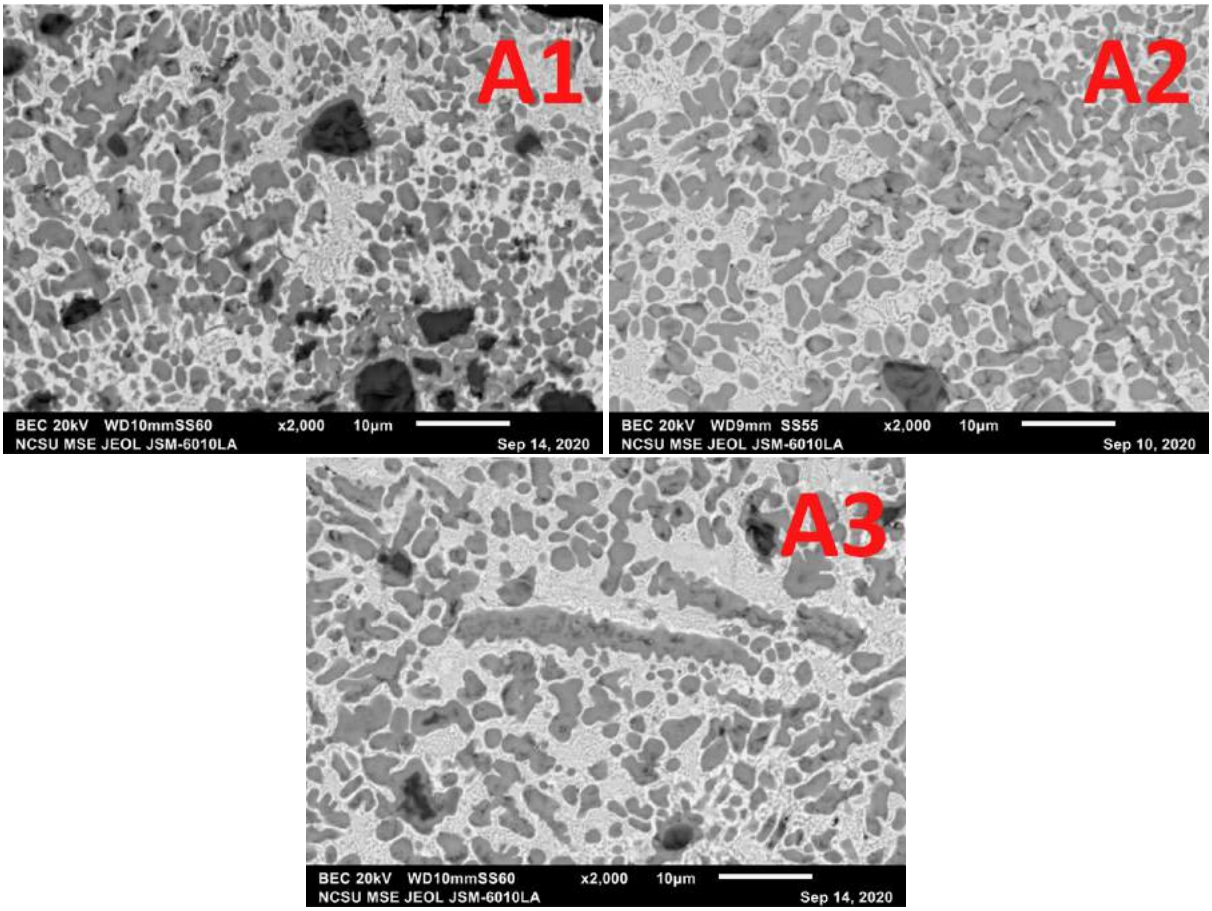

Figure 4.39 Representative, large magnification images of the samples in Group A.

grey, dendritic structures indicates that they are likely not structures of Mo_2C, a phase which would be detrimental to the mechanical properties of the material. This also reveals that, while these darker grey, dendritic regions are likely the FCC TiC structures predicted by the generated phase diagrams, the presence of Mo suggests that molybdenum has been incorporated into the TiC lattice. This phenomenon of the solubility of Mo in TiC has been reported by the literature, and also is supported by the difference in contrast between the unmelted TiC particles and the melted TiC regions when imaged using the BEC mode of the SEM, as the detection of heavier elements results in a lighter pixel value.

From these samples alone, however, clear differences in microstructure between parameter sets can be observed, most notably in TiC and eutectic morphologies in the fully melted regions of the samples. Across parameter sets, as energy density and beam power increases, finer features are observed in the TiC-rich regions and with more clearly defined, longer dendrites visible in the very high energy density samples. By contrast, the dendritic structures, where visible in the lower energy samples, are coarser and less well-defined.

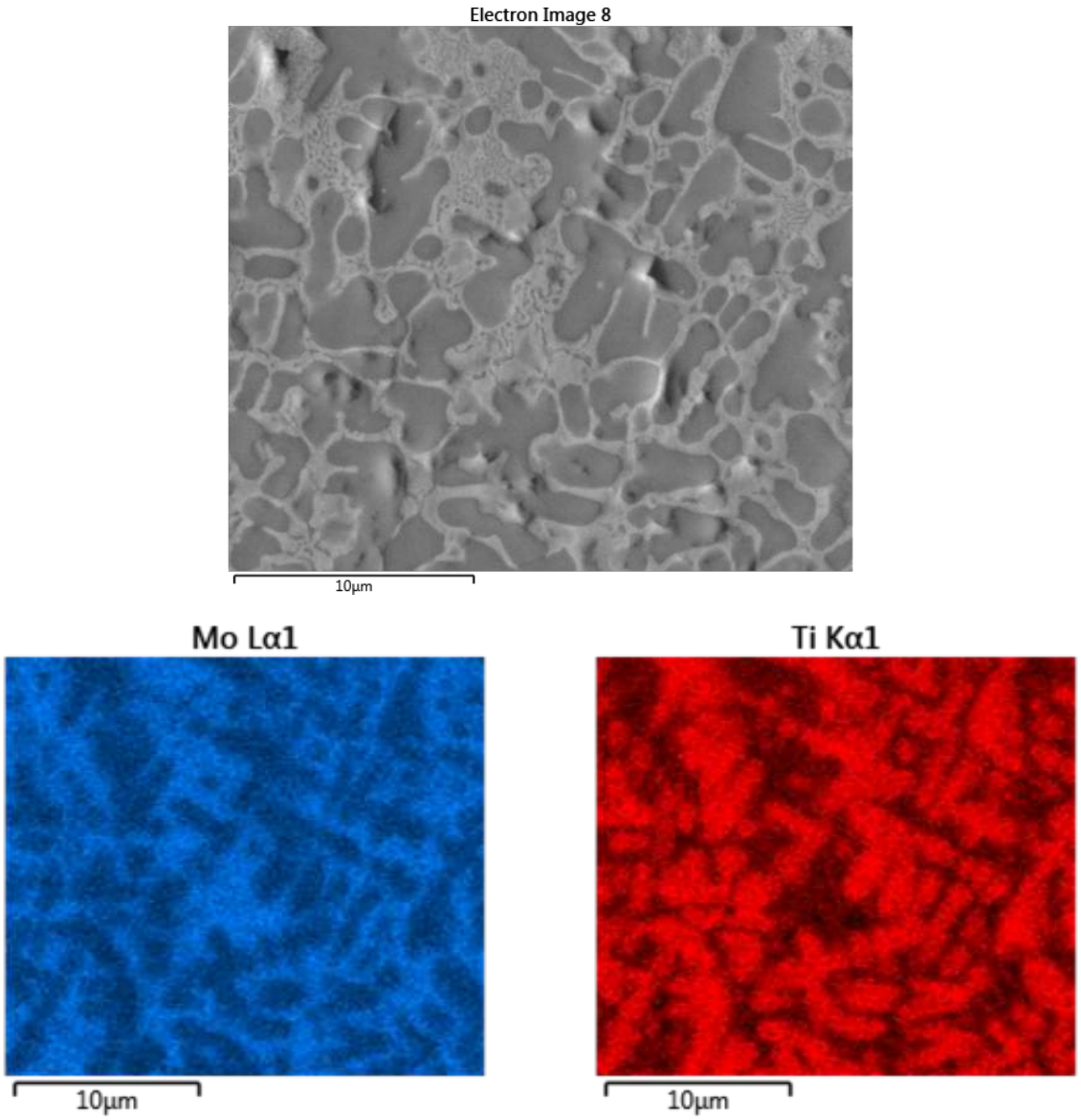

Figure 4.40 Representative EDS of dendritic regions in Mo-TiC samples from Group A, from sample A3.

Figure 4.41 is a composite of the results from Group B, with contour thermal model results on the top and low magnification SEM images of the melted regions below. Unlike the previous set of samples, all samples in the B group have the same energy density of 15355, but with different line offsets to explore its effects on the produced microstructures. As such, these parameter sets were specifically designed to experience different thermal conditions during melting, despite their equivalent energy densities, allowing for the further exploration of beam parameters on the Mo-TiC system. Figure 4.41A show the thermal model contour results

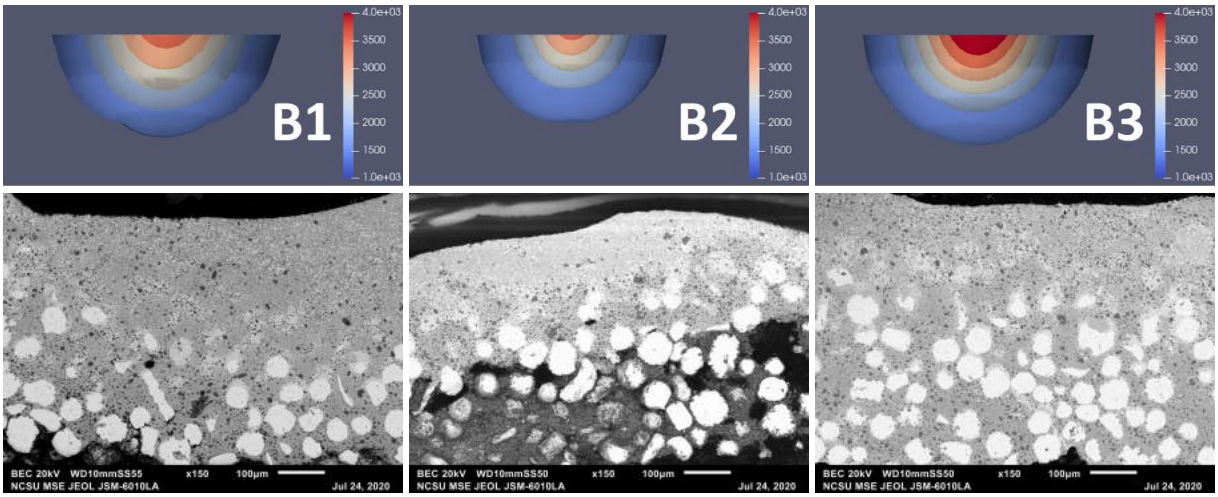

Figure 4.41 Representative, small magnification images of samples with associated thermal contour plots for the samples in Group B.

of the sample with a line offset of 0.05mm, the same as the previous set of samples, and a maximum average temperature of 4208°C. Figures 4.41B and C show the contour model results for samples B2 and B3, respectively, each with a line offset of 0.15mm and with the parameter set in Figure 4.41B having half the velocity and power of the parameter set shown in Figure 4.41C. Despite equivalent energy densities and line offsets, the maximum average temperatures were calculated to be 3423°C and 4607°C for samples B2 and B3, respectively. The result of this difference in thermal conditions is that, as expected, sample thickness increased as the maximum modeled temperature increased, with the middle sample having both the lowest estimated temperature and lowest sample depth in Group B. Unmelted TiC particles, TiC dendrites, and fine lamellar eutecic regions were found in all samples, as well as limited porosities in the transition region, largely consistent with the previous sample set and published data.

Figure 4.42 presents representative, higher magnification images taken within the bulk of the melted sample regions of Group B, with overall TiC morphology differing significantly between the different parameter sets. As shown in the B1 sample in Figure 4.42, a higher speed but smaller line offset results in the solidified TiC morphologies being much coarser than the B2 or B3 samples, despite all samples being at the same energy density. Thus the energy density is not the only factor in the control of internal microstructure, and there are likely other major factors to consider. Of primary interest in this Group B is the variation in line offset, and its effect on the internal microstructures. A line offset value of 0.05mm was chosen for initial experimentation to allow for easier comparison to previous research. A value of 0.15mm for the line offset was chosen specifically due to the contrast between the size of the starting

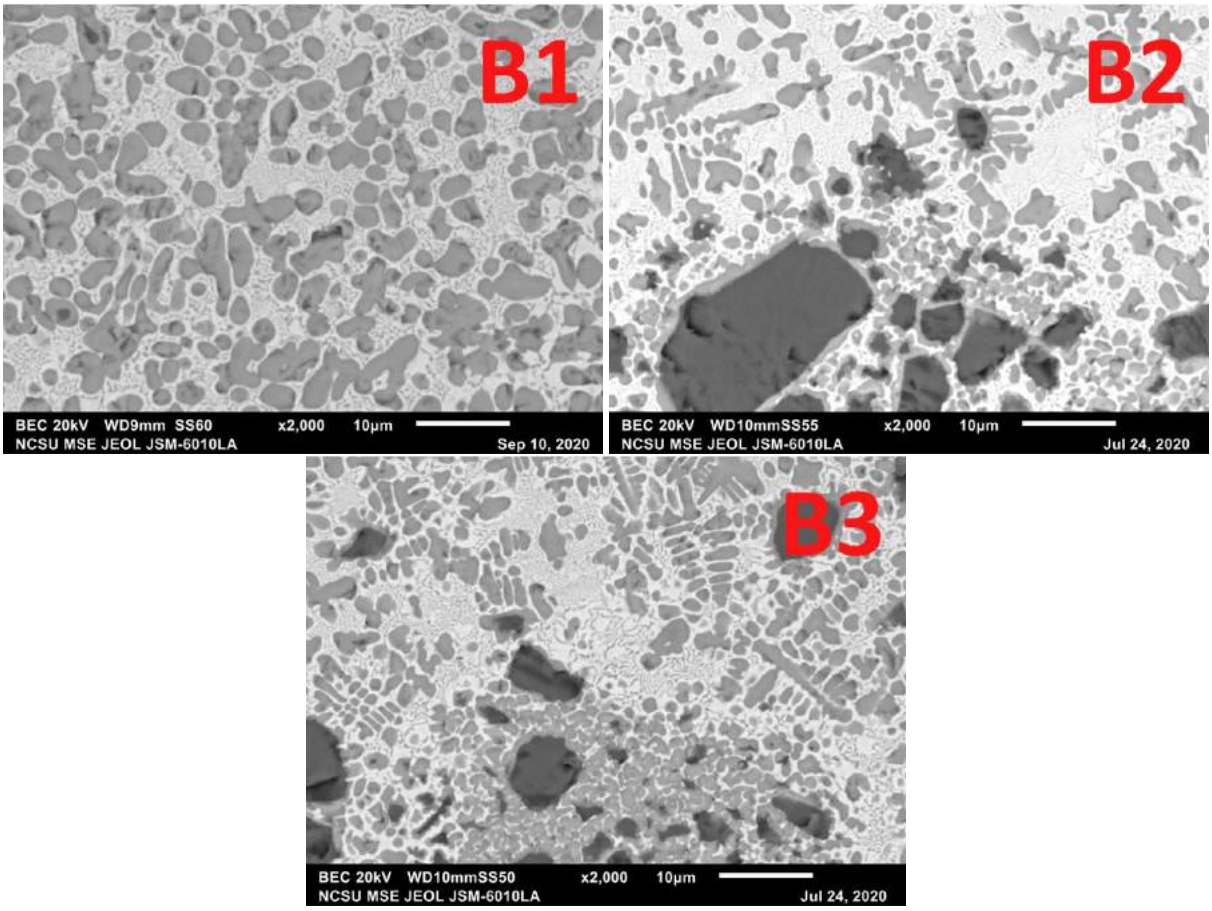

Figure 4.42 Representative, larger magnification images of the samples in Group B.

powder and the electron beam hatch spacing, with the line offset being larger than the d90 of the starting powder. The effect of this larger line offset is the limiting of powder particles melted repeatedly, as is certainly the case with the 0.05mm line offset samples.

Figure 4.43 is a composite of the results from Group C, with contour thermal model results on the top, low magnification SEM of the total beam interaction region on the bottom. These samples both have the same, very high energy density of 46065, with parameters designed to experience extreme thermal conditions during melting. The contour profiles shown in Figures 4.43A & B reveal that the thermal conditions are extreme, with maximum average temperatures of 4961°C and 5495°C, respectively. These temperatures are far beyond the melting point of any possible component or phase in the Mo-TiC system, which is useful in ensuring that the microstructures associated with fully melted Mo and TiC are confirmed as such. Additionally, these samples are used to evaluate the modeling methodology at an extreme end of the possible parameter space.

Figure 4.44 presents representative, higher magnification images taken within the bulk of

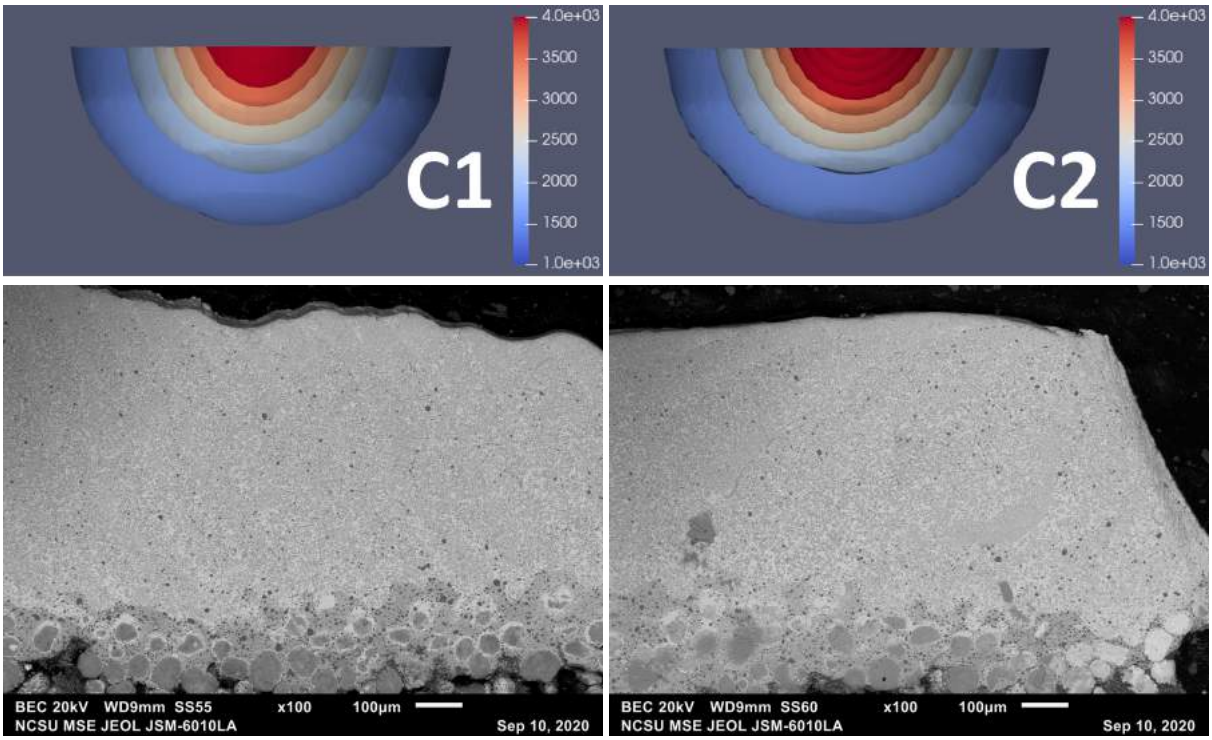

Figure 4.43 Representative, small magnification images of samples with associated thermal contour plots for the samples in Group C.

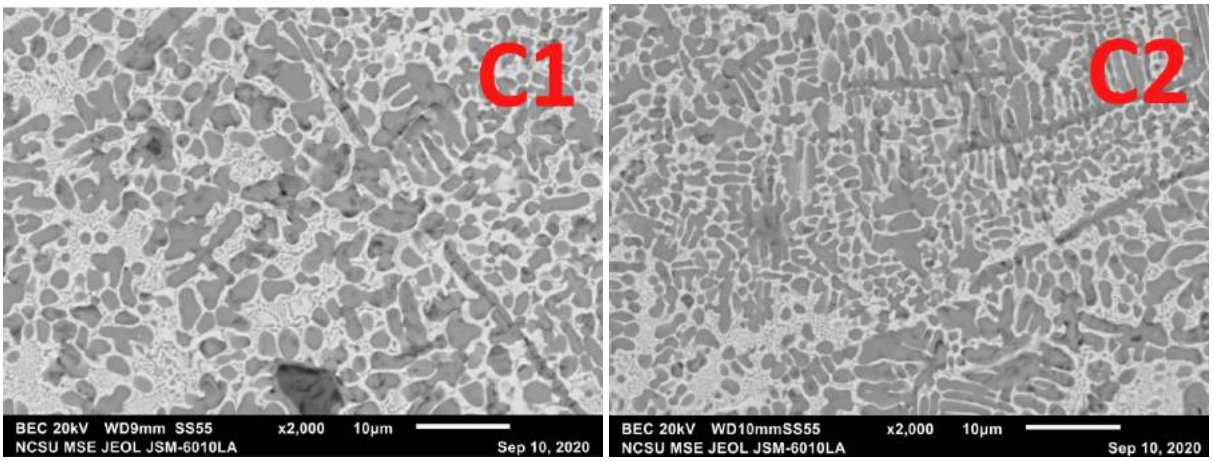

Figure 4.44 Representative, larger magnification images of the samples in Group C.

the melted sample regions of Group C, with overall TiC morphology observed to differ between parameter sets. Sample C1 contains precipitated TiC that has observable but more limited dendritic qualities when compared to the microstructure of C2 shown in Figure 4.44. C2, with as higher beam speed and power, shows a finer and significantly more defined dendritic structure in the re-solidified TiC regions, with long primary and secondary dendrites clearly visible. This further supports the trend seen in previous sample groups where higher maximum average

temperatures are associated with a finer, more dendritic TiC structure.

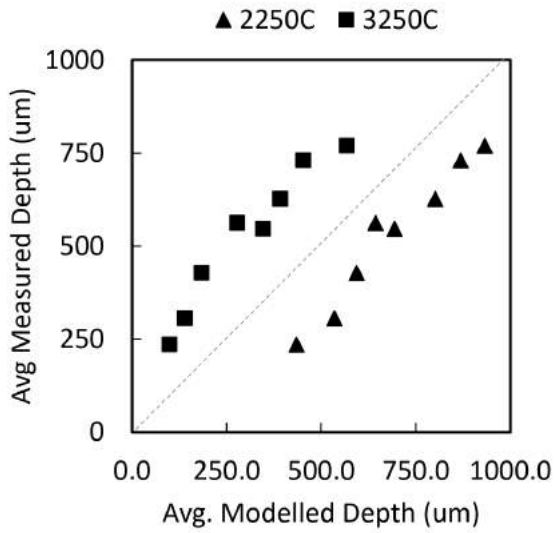

Figure 4.45 Measured melt pool depth relative to modeled contour line depth for all Mo-TiC samples, with dashed grey line showing 'ideal' 1:1 correlation between the measured and modeled depth.

Figure 4.45 compares the 2250°C and 3250°C contour lines, used to estimate the trend in melt pool depth, with the values measured for all samples. This plot reveals both sets of contour lines to be largely proportional with each other and the measured depths. There is a consistent gap between the two model data sets and the measured depths, with the 3250°C contour line underestimating the melt pool depth as measured and the 2250°C line overestimating the melt pool. These results also correlate with those generated during WC-Co experimentation, and indicate that a contour temperature value higher than 2250°C but lower than 3250°C would more accurately predict measured melt pool depth. Based on these results, the model predicts the overall trend in melt pool size well, though with deviations from linearity likely a results of nominal experimental variation.

The contour line corresponding to a temperature of 2628°C was the most accurate in predicting measured melt pool depth from all Mo-TiC samples, with an average error of 8.1% which, though more than that seen in the WC-Co experimentation, still provides valuable information about and confirmation for the thermal model's ability to consistently predict conditions during the melting of Mo-TiC. These results, plotted in Figure 4.46, suggest that the temperature must reach at least 2628°C before noticeable melting will occur, and thus this temperature can be used in conjunction with the thermal model to provide parameter sets

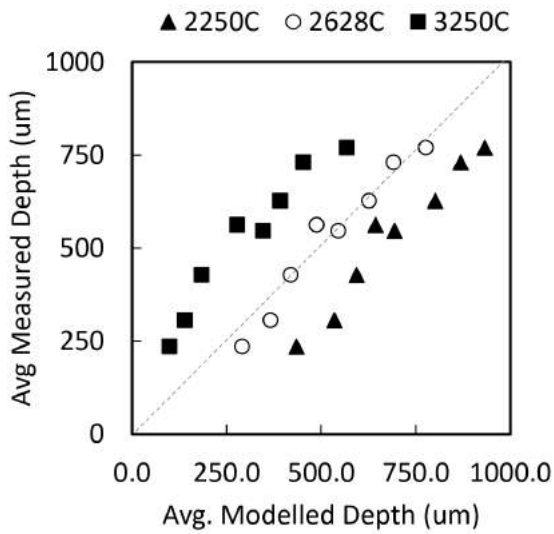

Figure 4.46 modeled contour line depths, including calculated 'ideal' contour line depth, plotted against measured melt pool depth for all Mo-TiC samples, with dashed grey line showing 'ideal' 1:1 correlation between the measured and modeled depth.

that target specific melt pool properties, or in targeting different EBM results, can be utilized to ensure sufficient melting will occur with any given parameter set.

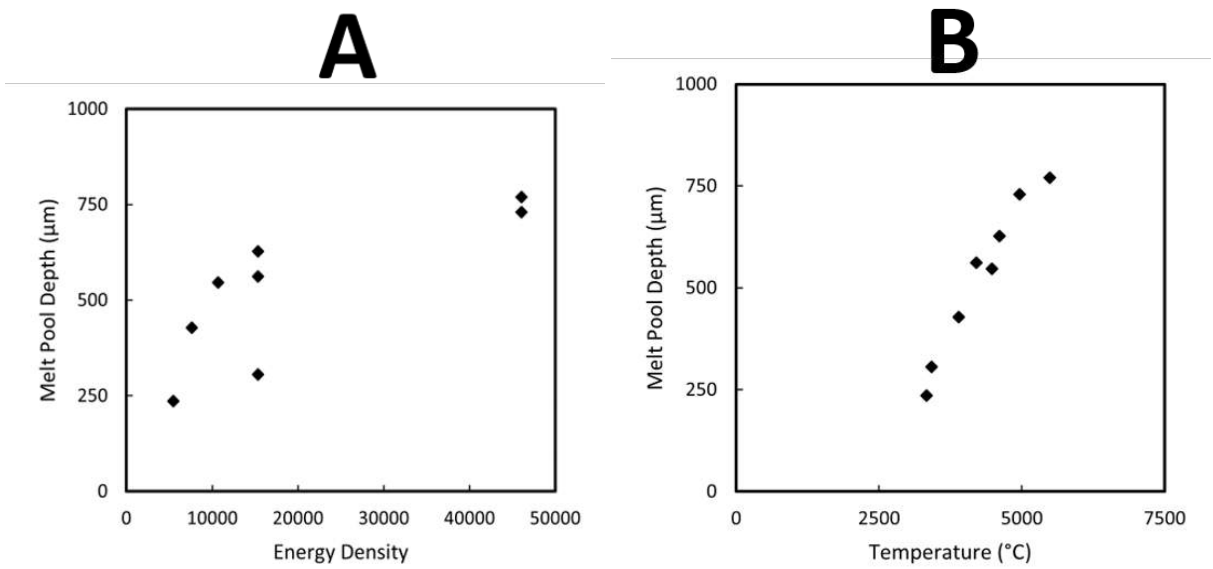

Figure 4.47 Measured melt pool depth as a function of (A) energy density and (B) maximum average temperature for all Mo-TiC samples

Plotting energy density against measured melt pool depth, as shown in Figure 4.47A, confirms that as energy density increases, the sample melt pool depth increases, from the lowest value of 236um at an energy density of 5445 to 770um at an energy density of 46065. This trend does not appear to be linear, with very high energy densities yielding diminishing increases in melt pool depth for each subsequent increase in energy density. This correlates well with the conclusions drawn in the previous WC-Co section, as a similar non-linearity was also observed. Figure 4.47B also illustrates a positive trend when plotting measured melt pool depth versus average maximum temperature for each sample, with the melt pool depth increasing as maximum average temperature increases. The strong linearity of the relationship between maximum modeled temperature and measured melt pool depth indicates that the former is a more useful metric for predicting melt pool size, as samples with equivalent energy densities can exhibit large differences in melt pool depth as shown in Figure 4.47A. Energy density is a common way to illustrate and compare parameters, however it may not fully communicate their effects, especially when operating in the extreme of the parameter space.

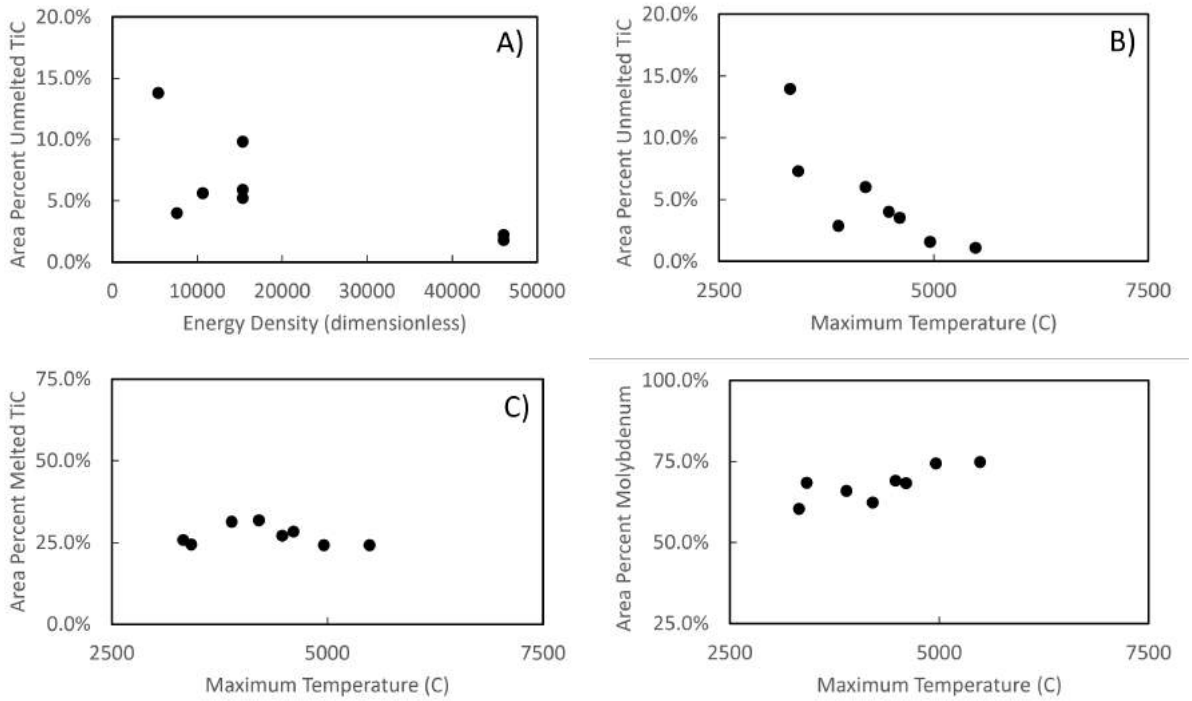

Figure 4.48 Average area fraction of microstructural features as a function of thermal properties as detected through image analysis, including the average area fraction of A) unmelted TiC particles vs. energy density, B) unmelted TiC particles vs. maximum average temperature, C) melted TiC vs. maximum average temperature, and D) Molybdenum vs. maximum average temperature.

Figure 4.48 shows the results of image analysis performed on SEM micrographs of the Mo-TiC samples, relating the calculated area of given microstructural features as a percent of the total area. The purpose of this analysis was to examine the effect of energy density and maximum average temperature on the formation and retention of certain phases of interest, including unmelted TiC particles, melted TiC regions, and the Mo-rich regions. These results are not directly related to real chemical compositions, as no assumptions are made here about the exact composition of these phases, e.g. TiC precipitate regions could likely contain a significant quantity of dissolved Mo. Figure 4.48A shows a positive correlation between energy density and % melted TiC by area, however Figure 4.48B shows a much clearer correlation between area fraction of unmelted TiC when plotted against average maximum temperature as derived from the thermal model. The comparison of the two plots indicates that maximum modeled temperature is a better predictor of microstructural properties than energy density. This positive correlation in Figure 4.48B supports the qualitative observation, made previously, that increasing size and number of the intact, unmelted TiC particles corresponded with decreased modeled temperatures.

Figure 4.48C shows no strong trend when comparing maximum temperature and melted TiC-rich regions, while Figure 4.48D exhibits a positive correlation between maximum temperature and Mo-rich regions in the manufactured samples. These results would appear to contradict those shown in Figure 4.48B, as a decrease in unmelted TiC particles as temperatures increase would intuitively imply that the amount of melted TiC present in the manufactured samples would increase as TiC particles go from unmelted to melted. However, the relatively consistent amount of melted TiC across samples as shown in Figure 4.48C shows this is not the case; indeed, the opposite may even be occurring. This indicates that, rather than the presence of unmelted TiC decreasing as a result of melting, the presence of unmelted TiC particles decreases due to TiC being removed as a result of the beam interaction with the powder bed, with the degree of removal increasing as energy density increases. This phenomenon has been seen in many other alloys systems in AM, and is not improbable given the highly energetic conditions that occur in conjunction with higher temperatures.

When comparing modeled and measured depth to the presence of the different compositional regions, as is done in Figure 4.49A-B, similar trends are observed as those illustrated by the previous Figure 4.49. This is expected given the strong linearity shown earlier between the contour depth of the thermal model and the measured sample depths as shown previously in Figure 4.48. For ease of viewing, the data of the average area fraction of unmelted TiC particles is shown by itself and plotted, in the lower graphs, against modeled and measured depths, respectively.

From EDS mapping data, as shown in Figure 4.50, illuminates the compositional changes

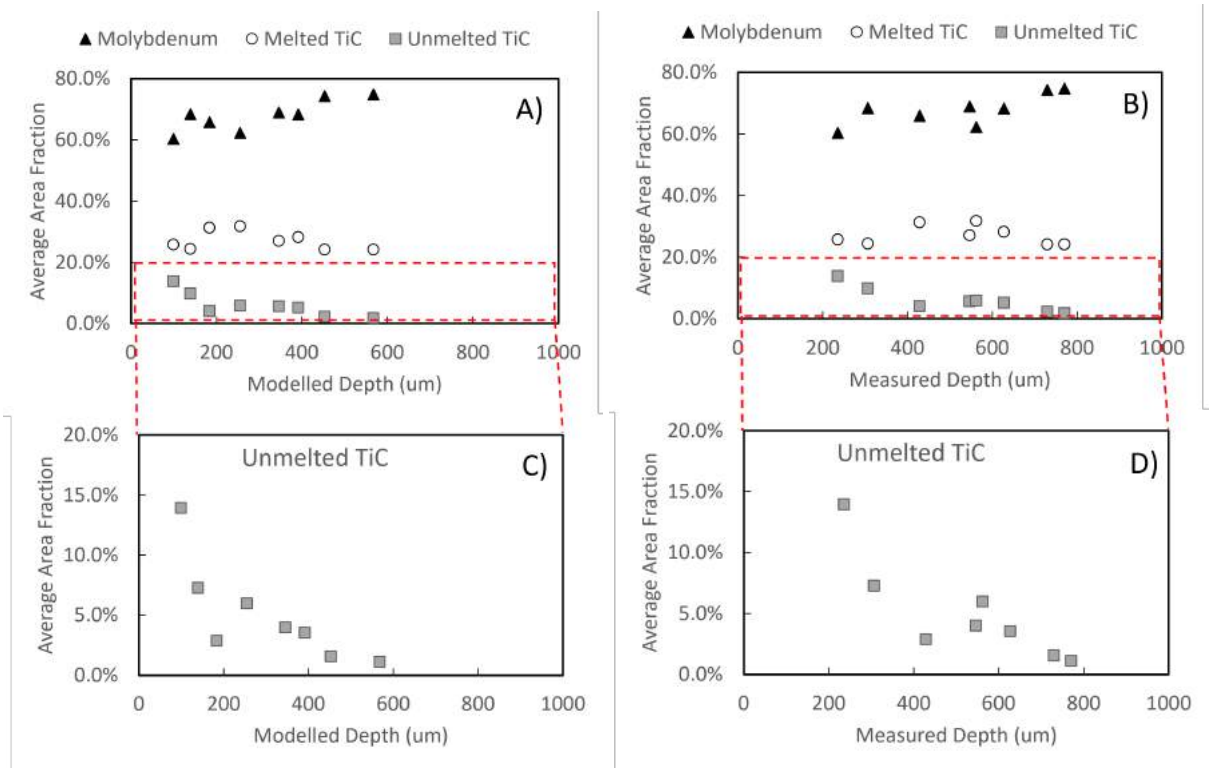

Figure 4.49 Average area fraction of microstructural features as a function of modeled depth as based on the calculated 'ideal' contour line of 2628°C as well as measured sample depth as detected through image analysis. The figures include the average area fraction of A) all features vs. modeled depth, B) all features vs. measured depth, C) unmelted TiC particles vs. modeled depth, and D) unmelted TiC particles vs. measured depth.

that occur during and after melting within the Mo-TiC samples. In Figure 4.50, a representative area of the non-dendritic TiC precipitates are mapped, including regions of unmelted or semi-melted TiC particles seen in the top-left electron image. These unmelted TiC regions lack detectable Mo by EDS, however Mo is detectable in the regions surrounding and adjacent to these TiC precipitates, indicating that Mo is indeed incorporated into these TiC regions, as is made possible by the up to 25mol% solubility of Mo in compositions of more than 25mol% TiC.

With this information the thermal and thermodynamic models are shown to be useful in the prediction of conditions during melt pool solidification, and control of microstructural features within the material. Eutectic compositions are clearly seen throughout the samples, indicating that incorporation of liquid TiC into a liquid Mo melt pool is most likely inevitable when melting this system to any significant degree. This would be necessary in full-scale AM due to the need to adhere multiple layers together to form a cohesive part, and especially in the manufacturing of high temperature, more brittle materials like Mo-TiC and WC-Co, which are prone to high degrees of thermal stresses.

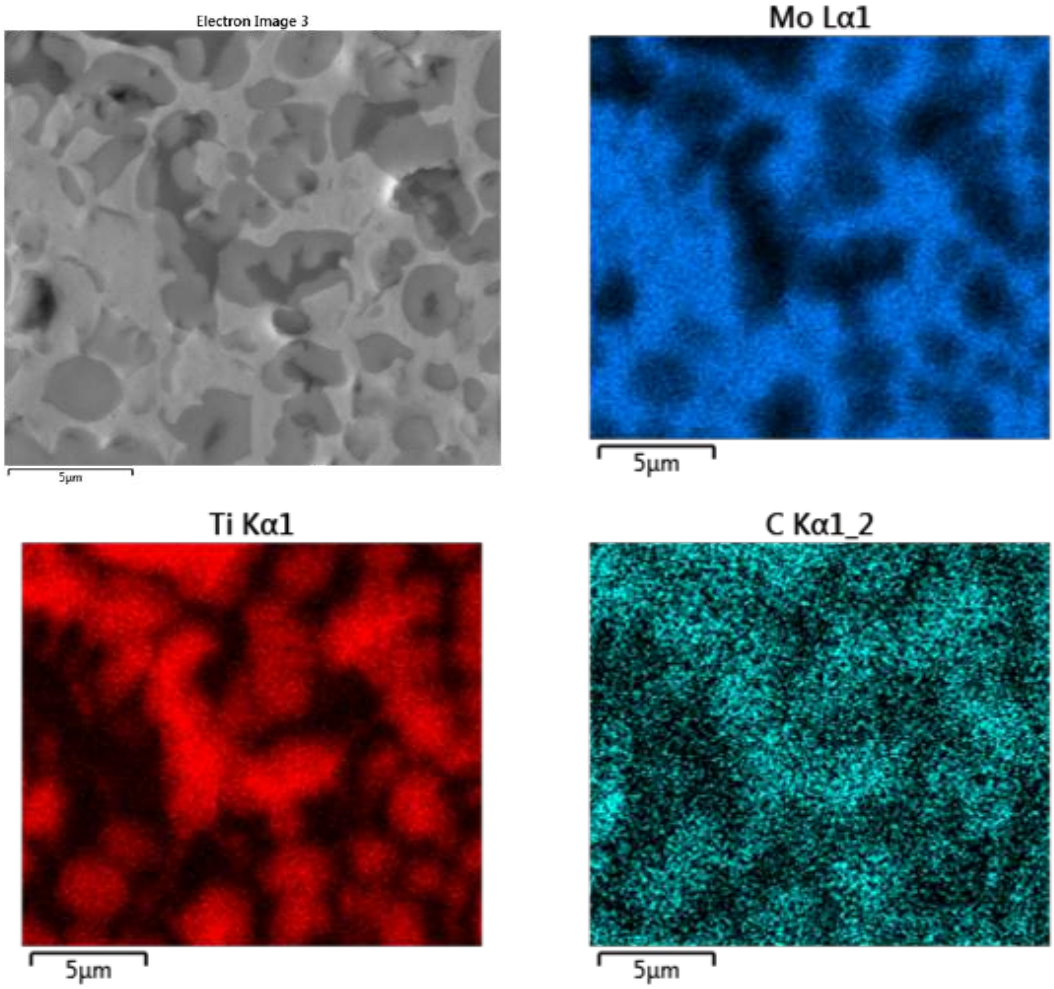

Figure 4.50 Representative EDS mapping of typical non-dendritic regions in Mo-TiC samples

Given that there were many Mo-rich and TiC-rich particulates that appear unmelted, especially in the lower energy samples, this better indicates both the duration and the magnitude of temperatures reached during melting could preserve some TiC particles in practice. However, the re-melting of layers that occurs in full-scale AM may further reduce or eliminate these second phase particles, changing local compositions and microstructures. No graphite or other majority-carbon phases were observed, which indicates that local compositions of carbon do not reach high enough thresholds to form, even in the most extreme conditions. The elemental composition was found to be approximately 75 wt% Mo, 21 wt% Ti, and 4 wt% C as determined by XRF spectrometry.

Through Rietveld refinement of XRD spectra data from selected samples, small quantities of Mo_2C were revealed to have been formed during the single-layer EBM, indicating that a significant portion of the EBM process occurred outside equilibrium, as the ThermoCalc

phase diagrams predicted significant quantities of Mo_2C based on the initial composition. However, the final composition was much richer in Mo than the feedstock powder, changing the microstructures expected to form and confirming significant removal of TiC from the melt pool during the melting process as discussed previously and resulting in a solidification path that differed significantly from that predicted for the initial Mo-TiC alloy. Despite this, the thermal modeling was shown to accurately and precisely predict melt pool conditions for a broad range of parameter sets, allowing for clear trends in melt pool dimension and general composition to be found.

4.4 Conclusions

The studies presented in this research have shown that the results of EBM were highly dependent on the specific combination of many parameters, leading to the need for a comprehensive predictive methodology that could combine the information from several modeling systems to produce an efficient but accurate estimation of material properties post-processing . In this framework, it was shown that a combination of thermodynamic information from ThermoCalc and the FeNICs-based temperature modeling could be utilized to quickly and accurately predict key properties of a material as a result of interaction with an electron beam, with increased flexibility and computational efficiency than other contemporary methods. Such predicted properties include melt pool size, thermal profiles, and the presence and preservation of material phases, allowing for the evaluation of machine parameters for the purposes of AM research or production in a more efficient manner than is widely adopted.

Specifically:

- In the WC-Co single line and single layer experiments, the melt pool depth was shown to have a strong, linear relationship when comparing the predicted and produced material melt pools. An 'ideal' temperature value was also found in WC-Co experimentation that accurately predicted melt pool depth in samples with less than 5% deviation in all but one parameter set.

- The single layer EBM of Mo-TiC also revealed predictability of the measured melt pool dimensions by the thermal model, with a strong linear correlation with the modeled depths, and after very limited experimentation was consistent in predicting melt pool dimension, with a temperature of 1660°C found to accurately predict melt pool size with less than 5.5% error in all but one parameter set.

- While produced microstructures differed at times from those predicted by equilibrium thermodynamic phase modeling, the thermal model data was found to more accurately

and consistently correlate and predict the formation of different phase compositions, such as TiC retention in Mo-TiC experimentation and eta phase formation in WC-Co experimentation.

- Additionally, the maximum average modeled temperatures for a given parameter set was found to more accurately and precisely predict microstructural features and melt pool depths than the more commonly used beam energy density, in both WC-Co and Mo-TiC experimentation.

4.5 Future Work

While the result of the present research are positive, there is more that could be done to improve the efficacy of the methodology, beyond simply a larger sample size.

Given the high degree of spatter generated, and the significant change in composition in the Mo-TiC experimentation, it is likely that TiC was removed from the material in significant quantities during melting. This issue could be mitigated by using lesser compositions of TiC or by better incorporating the TiC particles into the Mo powder; however, the poor conductivity of the TiC powder may inherently limit these benefits.

The application of additional characterization techniques, such as inductively coupled plasma mass spectrometry or electron backscatter diffraction analysis, could further characterize the material and microstructures created through EBM, aiding in the validation and extension of model results to compositions and parameter sets outside those presented here.

Additionally, there remains a gap in experimental data, specifically in the EBM production of full-scale, multi-layer articles from the Mo-TiC alloy. The methodology was effective in correlation and prediction of the formation of different phase compositions in the multi-layer WC-Co samples; however, there is a lack of data on the efficacy of the evaluated Mo-TiC parameter sets on multi-layer AM of the Mo-TiC MMC.

Overall, given the promise shown by this and previous work utilizing the thermal and thermodynamic phase modeling, there is sufficient motivation to further pursue the application of this methodology in the EBM field.

BIBLIOGRAPHY

[1] Sames, W. J. et al. "The metallurgy and processing science of metal additive manufacturing". *International Materials Reviews* **61**.5 (2016), pp. 315–360.

[2] Debroy, T et al. "Additive manufacturing of metallic components-Process, structure and properties" (2017).

[3] Gorsse, S. et al. *Additive manufacturing of metals: a brief review of the characteristic microstructures and properties of steels, Ti-6Al-4V and high-entropy alloys*. 2017.

[4] Körner, C. *Additive manufacturing of metallic components by selective electron beam melting - A review*. 2016.

[5] Najmon, J. C. et al. *Review of additive manufacturing technologies and applications in the aerospace industry*. 2019.

[6] Liu, R. et al. *Aerospace applications of laser additive manufacturing*. 2017.

[7] Calignano, F. et al. "Overview on additive manufacturing technologies". *Proceedings of the IEEE* **105** (4 2017), pp. 593–612.

[8] Harun, W. S. et al. *A review of powdered additive manufacturing techniques for Ti-6al-4v biomedical applications*. 2018.

[9] Martin, J. H. et al. "3D printing of high-strength aluminium alloys" (2017).

[10] Doñate-Buendia, C. et al. "Microstructure formation and mechanical properties of ODS steels built by laser additive manufacturing of nanoparticle coated iron-chromium powders". *Acta Materialia* **206** (2021).

[11] Kirka, M. M. et al. "Solidification and solid-state transformation sciences in metals additive manufacturing". *Scripta Materialia* **135** (2017), pp. 130–134.

[12] Seidel, A. et al. "Additive Manufacturing of Powdery Ni-Based Superalloys Mar-M-247 and CM 247 LC in Hybrid Laser Metal Deposition". *Metallurgical and Materials Transactions A* **49** ().

[13] Singh, S. et al. *Material issues in additive manufacturing: A review*. 2017.

[14] German, R. M. *Sintering : from emperical observations to scientific principles*. 2014, p. 536.

[15] Reed, R. C. *The Superalloys fundamentals and applications*. Vol. 9780521859042. Cambridge University Press, 2006, pp. 1–372.

[16] Guo, Z. & Sha, W. *Quantification of Precipitation Hardening and Evolution of Precipitates*. 2002, pp. 1273–1282.

[17] Chandran, K. S. & Fang, Z. Z. *Microstructure Design of Advanced Materials Through Microelement Models: WC-Co Cermets and Their Novel Architectures*. 2003.

[18] Ohser-Wiedemann, R. et al. "Spark plasma sintering of TiC particle-reinforced molybdenum composites". *International Journal of Refractory Metals and Hard Materials* **32** (2012), pp. 1–6.

[19] Browning, P. N. et al. "Sintering behavior and mechanical properties of Mo-TZM alloyed with nanotitanium carbide". *International Journal of Refractory Metals and Hard Materials* **62** (2017), pp. 78–84.

[20] Frazier, W. E. *Metal additive manufacturing: A review*. 2014.

[21] Kayacan, M. Y. & Yılmaz, N. "An investigation on the measurement of instantaneous temperatures in laser assisted additive manufacturing by thermal imagers". *Measurement: Journal of the International Measurement Confederation* **160** (2020).

[22] Coleman, J. et al. "Sensitivity of thermal predictions to uncertain surface tension data in laser additive manufacturing". *Journal of Heat Transfer* **142** (12 2020).

[23] Godec, M. et al. "Quantitative multiscale correlative microstructure analysis of additive manufacturing of stainless steel 316L processed by selective laser melting". *Materials Characterization* **160** (2020).

[24] Dudley, R. A. & Fiddy, M. A. *Engineered Materials and Metamaterials: Design and Fabrication*. SPIE, 2017.

[25] Flemings, M. C. *Behavior of Metal Alloys in the Semisolid State*. ASM INTERNATIONAL, 1991.

[26] Reed-Hill, R. & Abbaschian, R. *Physical Metallurgy Principles*. PWS-Kent series in engineering. PWS-Kent Pub., 1992.

[27] Beeley, P. *Foundry Technology*. Elsevier Science, 2001.

[28] Zyuban, N. et al. "A Study of the Development of Chemical Heterogeneity in Large Forging Ingots: Depending Upon the Configuration and Thermophysical Conditions of Casting". *Metallurgical and Materials Transactions A: Physical Metallurgy and Materials Science* **45** (13 2014), pp. 6200–6206.

[29] Piątkowski, J. et al. *Thermophysical properties of nickel-based cast superalloys*. 2015, pp. 543–546.

[30] Glazoff, M. et al. *Casting Aluminum Alloys*. Elsevier Science, 2010.

[31] Cormier, J et al. “In-Situ Determination of Precipitation Kinetics During Heat Treatment of Superalloy 718” ().

[32] Trosch, T. et al. *Microstructure and mechanical properties of selective laser melted Inconel 718 compared to forging and casting*. 2016.

[33] Zhang, D. et al. “Comparison of microstructures and mechanical properties of Inconel 718 alloy processed by selective laser melting and casting”. *Materials Science and Engineering A* **724** (2018), pp. 357–367.

[34] Bauri, R. & Yadav, D. *Metal Matrix Composites by Friction Stir Processing*. Friction Stir Welding and Processing. Elsevier Science, 2017.

[35] Gokuldoss, P. K. et al. *Additive manufacturing processes: Selective laser melting, electron beam melting and binder jetting-selection guidelines*. 2017.

[36] Liu, S. & Shin, Y. C. “Additive manufacturing of Ti6Al4V alloy: A review”. *Materials and Design* **164** (2019).

[37] Wang, X. et al. *Review on powder-bed laser additive manufacturing of Inconel 718 parts*. 2017.

[38] Fang, Z. *Sintering of Advanced Materials*. Woodhead Publishing Series in Metals and Surface Engineering. Elsevier Science, 2010.

[39] Goetzel, C. G. *Treatise on Powder Metallurgy*. Vol. 4. John Wiley and Sons, Inc., 1963, pp. 1–837.

[40] Attar, H. et al. “Comparative study of microstructures and mechanical properties of in situ Ti-TiB composites produced by selective laser melting, powder metallurgy, and casting technologies”. *Journal of Materials Research* **29** (17 2014), pp. 1941–1950.

[41] Susila, P. et al. “Microstructural studies on nanocrystalline oxide dispersion strengthened austenitic (Fe-18Cr-8Ni-2W-0.25Y2O3) alloy synthesized by high energy ball milling and vacuum hot pressing”. Vol. 45. 2010, pp. 4858–4865.

[42] Phaniraj, M. P. et al. “Microstructure development in mechanically alloyed yttria dispersed austenitic steels”. *Acta Materialia* **57** (6 2009), pp. 1856–1864.

[43] Kim, T. K. et al. “Microstructural observation and tensile isotropy of an austenitic ods steel”. *Nuclear Engineering and Technology* **40** (4 2008), pp. 305–310.

[44] Atkinson, H. V. & Davies, S. “Fundamental aspects of hot isostatic pressing: An overview”. *Metallurgical and Materials Transactions A: Physical Metallurgy and Materials Science* **31** (12 2000), pp. 2981–3000.

[45] Loh, N. L. & Sia, K. Y. *An overview of hot isostatic pressing*. 1992, pp. 45–65.

[46] Donachie, M. *Titanium: A Technical Guide, 2nd Edition*. Ingenieria e ingenieria civil. ASM International, 2000.

[47] Yang, Y. et al. "Additive manufacturing of WC-Co hardmetals: a review". *International Journal of Advanced Manufacturing Technology* **108** (5-6 2020), pp. 1653–1673.

[48] Yang, Q. et al. "The effects of fine WC contents and temperature on the microstructure and mechanical properties of inhomogeneous WC-(fine WC-Co) cemented carbides". *Ceramics International* **42** (16 2016), pp. 18100–18107.

[49] German, R. M. *Liquid Phase Sintering*. Springer US, 1985.

[50] Petzow, G & Kaysser, A. *Sintered Metal-Ceramic Composites*. 1984, pp. 51–70.

[51] Lesnik, N. D. *Springer Science+Business Media New York THEORY AND TECHNOLOGY OF SINTERING, THERMAL AND THERMOCHEMICAL TREATMENT MICROSTRUCTURE FORMATION AND EVOLUTION IN COMPOSITES DURING LIQUID-PHASE SINTERING*. 2013, pp. 11–12.

[52] Yang, D. Y. et al. "Suppression of abnormal grain growth in WC-Co via two-step liquid phase sintering". *Journal of the American Ceramic Society* **94** (4 2011), pp. 1019–1024.

[53] Bunnell, D. E. et al. *Fundamentals of Liquid Phase Sintering During Selective Laser Sintering*. 1994.

[54] German, R. M. & Rabin, B. H. "Enhanced sintering through second phase additions". *Powder Metallurgy* **28** (1 1985), pp. 7–12.

[55] Decker, R. F. "ALLOY DESIGN, USING SECOND PHASES." *Metall Trans* **4** (11 1973), pp. 2495–2518.

[56] Froschauer, L. & Fulrath, R. M. "Direct observation of liquid-phase sintering in the system iron-copper". *Journal of Materials Science* **10** (12 1975), pp. 2146–2155.

[57] Ibrahim, I. A. et al. *Particulate reinforced metal matrix composites-a review*. 1991, p. 1156.

[58] Nishida, Y. *Introduction to Metal Matrix Composites: Fabrication and Recycling*. SpringerLink : Bücher. Springer Japan, 2013.

[59] Luo, Y. H. et al. *From molecular metal complex to metal-organic framework: The CO 2 reduction photocatalysts with clear and tunable structure*. 2019.

[60] Dhingra, A. K. "Metals Replacement by Composites". *JOM* **38** (3 1986), p. 17.

[61] Persson, P. et al. "Self-propagating high-temperature synthesis and liquid-phase sintering of TiC/Fe composites". Vol. 127. Elsevier, 2002, pp. 131–139.

[62] Parashivamurthy, K. I. et al. *PROCESSING AND MECHANICAL PROPORTIES OF Fe-TiC COMPOSITES Elastic Stress Distribution around Holes in Infinite Plates Subjected to Uniaxial Loading View project PROCESSING AND MECHANICAL PROPORTIES OF Fe-TiC COMPOSITES*. 2005.

[63] Sharma, D. K. et al. "Manufacturing of metal matrix composites: A state of review". Vol. 26. Elsevier Ltd, 2019, pp. 506–519.

[64] Majumdar, S. et al. "Densification and grain growth during isothermal sintering of Mo and mechanically alloyed Mo-TZM". *Acta Materialia* **57** (14 2009), pp. 4158–4168.

[65] Ning, J. et al. "Analysis of microstructure and mechanical strength of lap joints of TZM alloy welded by a fiber laser". *Journal of Manufacturing Processes* **39** (2019), pp. 146–159.

[66] Kaserer, L. et al. "Fully dense and crack free molybdenum manufactured by Selective Laser Melting through alloying with carbon". *International Journal of Refractory Metals and Hard Materials* **84** (2019).

[67] Gu, D. *Laser additive manufacturing of high-performance materials*. Springer Berlin Heidelberg, 2015, pp. 1–311.

[68] Bhardwaj, T. et al. "Direct Energy Deposition - Laser Additive Manufacturing of Titanium-Molybdenum alloy: Parametric studies, microstructure and mechanical properties". *Journal of Alloys and Compounds* **787** (2019), pp. 1238–1248.

[69] Braun, J. et al. "Molybdenum and tungsten manufactured by selective laser melting: Analysis of defect structure and solidification mechanisms". *International Journal of Refractory Metals and Hard Materials* **84** (2019).

[70] Upadhyaya, G. S. *Materials science of cemented carbides an overview*. 2001, p. 483489.

[71] Zhou, W. et al. "Novel laser additive-manufactured Mo-based composite with enhanced mechanical and oxidation properties". *Journal of Alloys and Compounds* **819** (2020).

[72] Guillermet, A. F. "Thermal properties of powder beds in energy absorption and heat transfer during additive manufacturing with electron beam". *Metall. Trans. A* **20, no. 5** (1989), pp. 935–956.

[73] Goldschmidt, H. & Brand, J. "The tungsten-rich region of the system tungsten-carbon". *Journal of the Less Common Metals* **5**.2 (1963), pp. 181–194.

[74] Wang, X. et al. "Unstable twin in body-centered cubic tungsten nanocrystals". *Nature Communications* **11** (1 2020), pp. 1–7.

[75] Allibert, C. H. "Sintering features of cemented carbides WC-Co processed from fine powders". Vol. 19. Elsevier, 2001, pp. 53–61.

[76] Raihanuzzaman, R. M. et al. *Powder refinement, consolidation and mechanical properties of cemented carbides - An overview*. 2014.

[77] Lavergne, O. & Allibert, C. “Dissolution mechanism of tungsten carbide in cobalt-based liquids”. *High Temperatures-high Pressures* **31** (1999), pp. 347–355.

[78] Sánchez, J. M. et al. “HIP after sintering of ultrafine WC-Co hardmetals”. *International Journal of Refractory Metals and Hard Materials* **23** (3 2005), pp. 193–198.

[79] Hwang, K. S. et al. *Capillary Forces between Spheres during Agglomeration and Liquid Phase Sintering*.

[80] Ordóñez, A. et al. “Sintering + HIP of Ultrafine WC-Co Hardmetals”. *Materials Science Forum* **560** (2007), pp. 121–126.

[81] Kishino, J. et al. “Computational study on grain growth in cemented carbides”. *International Journal of Refractory Metals and Hard Materials* **20** (1 2002), pp. 31–40.

[82] Politi, J. R. D. S. et al. “Atomic and electronic structure of molybdenum carbide phases: Bulk and low Miller-index surfaces”. *Physical Chemistry Chemical Physics* **15** (30 2013), pp. 12617–12625.

[83] Shim, J. H. et al. “A thermodynamic evaluation of the Ti-Mo-C system”. *Metallurgical and Materials Transactions B: Process Metallurgy and Materials Processing Science* **27** (6 1996), pp. 955–966.

[84] Kurishita, H. et al. “Development of Molybdenum Alloy with High Toughness at Low Temperatures”. *Materials Transactions, JIM* **37**.1 (1996), pp. 89–97.

[85] Ida, S. et al. “Solidification pathways and phase equilibria in the Mo-Ti-C ternary system”. *High Temperature Materials and Processes* **39** (1 2020), pp. 164–170.

[86] Kaserer, L. et al. “Microstructure and mechanical properties of molybdenum-titanium-zirconium-carbon alloy TZM processed via laser powder-bed fusion”. *International Journal of Refractory Metals and Hard Materials* **93** (2020).

[87] Tuzemen, C. et al. “Production and characterization of TZM based TiC or ZrC reinforced composites prepared by spark plasma sintering (SPS)”. *Journal of Alloys and Compounds* **781** (2019), pp. 433–439.

[88] Leonard, K. J. *Radiation effects in refractory metals and alloys*. 2012.

[89] Kryukov, A. et al. “Irradiation embrittlement of reactor pressure vessel steel at very high neutron fluence”. *Journal of Nuclear Materials* **422** (1-3 2012), pp. 173–177.

[90] Eremenko, V. N. & Velikanova, T. Y. “The interaction of molybdenum with titanium carbide”. *Soviet Powder Metallurgy and Metal Ceramics* **2** (5 1963), pp. 347–352.

[91] Luo, Z. & Zhao, Y. *A survey of finite element analysis of temperature and thermal stress fields in powder bed fusion Additive Manufacturing*. 2018.

[92] AlMangour, B. et al. "Selective laser melting of TiC reinforced 316L stainless steel matrix nanocomposites: Influence of starting TiC particle size and volume content". *Materials and Design* **104** (2016), pp. 141–151.

[93] Volkov, A. V. et al. "Thermal oxidative degradation of molybdenum films under laser ablation". *Technical Physics* **60** (2 2015), pp. 265–269.

[94] Ibe, H. et al. "Formation process of microstructure in laser powder bed fusion with WC cemented carbide powder". *Funtai Oyobi Fummatsu Yakin/Journal of the Japan Society of Powder and Powder Metallurgy* **67** (6 2020), pp. 313–319.

[95] Konyashin, I. et al. "Additive manufacturing of WC-13%Co by selective electron beam melting: Achievements and challenges". *International Journal of Refractory Metals and Hard Materials* **84** (2019).

[96] Uhlmann, E. et al. "Investigation on Additive Manufacturing of Tungsten Carbide-cobalt by Selective Laser Melting". Vol. 35. Elsevier B.V., 2015, pp. 8–15.

[97] Shi, J. & Wang, Y. *Development of metal matrix composites by laser-assisted additive manufacturing technologies: a review*. 2020.

[98] Gu, D. D. et al. "Laser additive manufacturing of metallic components: Materials, processes and mechanisms". *International Materials Reviews* **57** (3 2012), pp. 133–164.

[99] Kumar, S. & Czekanski, A. "Optimization of parameters for SLS of WC-Co". *Rapid Prototyping Journal* **23** (6 2017), pp. 1202–1211.

[100] Khmyrov, R. S. et al. "Synthesis of Nanostructured WC-Co Hardmetal by Selective Laser Melting". Vol. 23. Elsevier B.V., 2017, pp. 114–119.

[101] Khmyrov, R. S. et al. "Phase composition and microstructure of WC-Co alloys obtained by selective laser melting". *Mechanics and Industry* **18** (7 2017).

[102] Khmyrov, R. S. et al. "Obtaining crack-free WC-Co alloys by selective laser melting". Vol. 83. Elsevier B.V., 2016, pp. 874–881.

[103] Schwanekamp, T. et al. "Impact of laser irradiation on microstructure and phase development of tungsten carbide - cobalt". Vol. 94. Elsevier B.V., 2020, pp. 239–242.

[104] Hao, S. Z. et al. "WC/Co composite surface structure and nano graphite precipitate induced by high current pulsed electron beam irradiation". *Applied Surface Science* **285** (PARTB 2013), pp. 552–556.

[105] Kruth, J. P. et al. "Lasers and materials in selective laser sintering". *Assembly Automation* **23** (4 2003), pp. 357–371.

[106] Chávez, J. et al. “Sintering behaviour and mechanical characterisation of Ti64/xTiN composites and bilayer components”. *Powder Metallurgy* **60** (4 2017), pp. 257–266.

[107] Danisman, C. B. et al. *Processing and characterization of spark plasma sintered TZM alloy*. 2016.

[108] Faidel, D. et al. “Investigation of the selective laser melting process with molybdenum powder”. *Additive Manufacturing* **8** (2015), pp. 88–94.

[109] Zhang, Y. et al. “Microstructure evolution and embrittlement of electron beam welded TZM alloy joint”. *Materials Science and Engineering A* **700** (2017), pp. 512–518.

[110] Shen, M. Y. et al. “Microstructure and fracture behavior of TiC particles reinforced Inconel 625 composites prepared by laser additive manufacturing”. *Journal of Alloys and Compounds* **734** (2018), pp. 188–195.

[111] Pribytkov, G. et al. “Additive manufacturing of parts from "titanium carbide-titanium" mechanically activated powder”. *Proceedings of the Advanced Materials with Hierarchical Structure for New Technologies and Reliable Structures*. Ed. by Fomin, V. et al. Vol. 2051. International Symposium on Hierarchical Materials: Development and Applications for New Technologies and Reliable Structures 2018 ; Conference date: 01-10-2018 Through 05-10-2018. American Institute of Physics Inc., 2018.

[112] Rock, C. et al. “Additive Manufacturing of Pure Mo and Mo + TiC MMC Alloy by Electron Beam Powder Bed Fusion”. *JOM* **72** (12 2020), pp. 4202–4213.

[113] Gaaly, A. “Optimization Models for Melting Patterns in Powder Bed Fusion Additive Manufacturing”. 2019.

[114] Lee, Y. S. & Zhang, W. “Modeling of heat transfer, fluid flow and solidification microstructure of nickel-base superalloy fabricated by laser powder bed fusion”. *Additive Manufacturing* **12** (2016), pp. 178–188.

[115] Liang, Z. et al. “Development of computational framework for titanium alloy phase transformation prediction in laser powder-bed fusion additive manufacturing”. *Materialia* **14** (2020).

[116] Cheng, B. & Chou, K. “Melt pool geometry simulations for powder-based electron beam additive manufacturing”. 2013.

[117] Bond, D. M. & Zikry, M. A. “Effects of electron beam manufacturing induced defects on fracture in Inconel 718”. *Additive Manufacturing* **32** (2020), p. 101059.

[118] Raplee, J. et al. “Thermographic Microstructure Monitoring in Electron Beam Additive Manufacturing”. *Scientific Reports* **7** (1 2017), pp. 1–16.

[119] Motaman, S. A. H. et al. “Optimal Design for Metal Additive Manufacturing: An Integrated Computational Materials Engineering (ICME) Approach”. *JOM* **72** (3 2020), pp. 1092–1104.

[120] Horstemeyer, M. F. M. F. *Integrated computational materials engineering (ICME) for metals : concept and case studies*.

[121] Huang, Y. et al. “Finite element analysis of thermal behavior of metal powder during selective laser melting”. *International Journal of Thermal Sciences* **104** (2016), pp. 146–157.

[122] Zhang, D. Q. et al. “Select laser melting of W-Ni-Fe powders: Simulation and experimental study”. *International Journal of Advanced Manufacturing Technology* **51** (5-8 2010), pp. 649–658.

[123] Ly, S. et al. “Metal vapor micro-jet controls material redistribution in laser powder bed fusion additive manufacturing OPEN” ().

[124] Matsumoto, M. et al. “Finite element analysis of single layer forming on metallic powder bed in rapid prototyping by selective laser processing”. *International Journal of Machine Tools and Manufacture* **42** (1 2002), pp. 61–67.

[125] Ledford, C. et al. “Evaluation of electron beam powder bed fusion additive manufacturing of high purity copper for overhang structures using in-situ real time backscatter electron monitoring”. Vol. 48. Elsevier B.V., 2020, pp. 828–838.

[126] King, W. E. et al. “Laser powder bed fusion additive manufacturing of metals; physics, computational, and materials challenges”. *Applied Physics Reviews* **2** (4 2015), p. 041304.

[127] Lee, Y. S. et al. “Asymmetric Cracking in Mar-M247 Alloy Builds During Electron Beam Powder Bed Fusion Additive Manufacturing”. *Metallurgical and Materials Transactions A: Physical Metallurgy and Materials Science* **49** (10 2018), pp. 5065–5079.

[128] Matthews, M. J. et al. “Denudation of metal powder layers in laser powder bed fusion processes”. *Acta Materialia* **114** (2016), pp. 33–42.

[129] Roy, S. et al. *HEAT TRANSFER MODEL AND FINITE ELEMENT FORMULATION FOR SIMULATION OF SELECTIVE LASER MELTING ADDITIVE MANUFACTURING*. 2017.

[130] Lopez, F. et al. “Identifying Uncertainty in Laser Powder Bed Fusion Additive Manufacturing Models”. *Journal of Mechanical Design* **138**.11 (2016). 114502.

[131] Shimono, Y. et al. *Numerical Simulation of Solidification in Additive Manufacturing of Ti Alloy by Multi-Phase Field Method*. 2017.

[132] Pal, D. et al. “An Efficient Multi-Scale Simulation Architecture for the Prediction of Performance Metrics of Parts Fabricated Using Additive Manufacturing”. *Metallurgical*

and Materials Transactions A: Physical Metallurgy and Materials Science **46** (9 2015), pp. 3852–3863.

[133] Touloukian, Y. S. et al. *Thermophysical properties of matter - the TPRC data series. Volume 12. Thermal expansion metallic elements and alloys. (Reannouncement). Data book*. 1975.

[134] Lide, D. R. et al. *CRC Handbook of Chemistry and Physics, 84th Edition, 2003-2004*. 2003.

[135] Assis Léo Machado, F. de et al. "Thermal properties of WC-10 wt. (%) Co alloys". *Materials Research* **11** (1 2008), pp. 37–41.

[136] Wang, H. et al. "Study of thermal expansion and thermal conductivity of cemented WC-Co composite". *International Journal of Refractory Metals and Hard Materials* **49** (1 2015), pp. 170–177.

[137] Ferreira, J. A. M. et al. "A study on the mechanical behaviour of WC/Co hardmetals" ().

[138] Franck, E. U. "J. D. Cox, D. D. Wagman, V. A. Medvedev: CODATA — Key Values for Thermodynamics, aus der Reihe: CODATA, Series on Thermodynamic Properties. Hemisphere Publishing Corporation, New York, Washington, Philadelphia, London 1989. 271 Seiten, Preis: £ 28.00". *Berichte der Bunsengesellschaft für physikalische Chemie* **94**.1 (1990), pp. 93–93. eprint: `https://onlinelibrary.wiley.com/doi/pdf/10.1002/bbpc.19900940121`.

[139] Zhao, Y. et al. "Thermal properties of powder beds in energy absorption and heat transfer during additive manufacturing with electron beam". *Powder Technology* **381** (2021), pp. 44–54.

[140] Gusarov, A. & Smurov, I. "Modeling the interaction of laser radiation with powder bed at selective laser melting". *Physics Procedia* **5** (2010), pp. 381–394.

[141] Cheng, B. et al. "A Combined Experimental-Numerical Method to Evaluate Powder Thermal Properties in Laser Powder Bed Fusion". *Journal of Manufacturing Science and Engineering* **140**.11 (2018). 111008. eprint: `https://asmedigitalcollection.asme.org/manufacturingscience/article-pdf/140/11/111008/6406465/manu\_140\_11\_111008.pdf`.

[142] *Computational Materials Engineering | Thermo-Calc Software*. 2021.

[143] Mason, P. & Hope, A. "Private communication". *ThermoCalc* ().

[144] Beuth, J. et al. "Process mapping for qualification across multiple direct metal additive manufacturing processes". 2013, pp. 655–665.

[145] Eso, O. et al. “Kinetics of cobalt gradient formation during the liquid phase sintering of functionally graded WC-Co”. *International Journal of Refractory Metals and Hard Materials* **25** (4 2007), pp. 286–292.

[146] Formisano, A. et al. “Influence of Eta-Phase on Wear Behavior of WC-Co Carbides”. *Advances in Tribology* **2016** (2016).

[147] Grigoriev, S. et al. “Possibilities of manufacturing products from cermet compositions using nanoscale powders by additive manufacturing methods”. *Materials* **12** (20 2019).

[148] Ku, N. et al. “Additive Manufacturing of Cemented Tungsten Carbide with a Cobalt-Free Alloy Binder by Selective Laser Melting for High-Hardness Applications”. *JOM* **71** (4 2019), pp. 1535–1542.

[149] Trojko, R et al. “The effect of silicon, aluminium and germanium on the stabilization of the C14 polymorph of HfMo2”. *Journal of the Less Common Metals* **92**.1 (1983), pp. 67–74.

[150] Dubrovinskaia, N. et al. “High-pressure study of titanium carbide”. *Journal of Alloys and Compounds* **289**.1 (1999), pp. 24–27.